Femtosecond-laser ablation dynamics of dielectrics: basics and applications for thin films

P Balling[1] **and J Schou**[2]

[1] Department of Physics and Astronomy, Aarhus University, Ny Munkegade 120, DK-8000 Aarhus C, Denmark
[2] DTU Fotonik, Risø Campus, Technical University of Denmark, DK-4000 Roskilde, Denmark

E-mail: balling@phys.au.dk and josc@fotonik.dtu.dk

Abstract

Laser ablation of dielectrics by ultrashort laser pulses is reviewed. The basic interaction between ultrashort light pulses and the dielectric material is described, and different approaches to the modeling of the femtosecond ablation dynamics are reviewed. Material excitation by ultrashort laser pulses is induced by a combination of strong-field excitation (multi-photon and tunnel excitation), collisional excitation (potentially leading to an avalanche process), and absorption in the plasma consisting of the electrons excited to the conduction band. It is discussed how these excitation processes can be described by various rate-equation models in combination with different descriptions of the excited electrons. The optical properties of the highly excited dielectric undergo a rapid change during the laser pulse, which must be included in a detailed modeling of the excitations. The material ejected from the dielectric following the femtosecond-laser excitation can potentially be used for thin-film deposition. The deposition rate is typically much smaller than that for nanosecond lasers, but film production by femtosecond lasers does possess several attractive features. First, the strong-field excitation makes it possible to produce films of materials that are transparent to the laser light. Second, the highly localized excitation reduces the emission of larger material particulates. Third, lasers with ultrashort pulses are shown to be particularly useful tools for the production of nanocluster films. The important question of the film stoichiometry relative to that of the target will be thoroughly discussed in relation to the films reported in the literature.

(Some figures may appear in colour only in the online journal)

This article was invited by Horst-Guenter Rubahn.

Contents

1. Introduction

At first sight there seems to be a contradiction in terms when discussing femtosecond-laser ablation of dielectric materials: most ultrashort-pulse laser systems operate in the infrared or visible regime, but these wavelengths are not absorbed by dielectric materials; the photon energy simply does not exceed the band gap. Traditionally, laser excitation of dielectrics has thus been based on ultraviolet (UV) lasers such as excimer lasers (see, e.g., [1]). However, as will be discussed in greater detail in section 2, the short pulse duration opens up for new material-excitation channels: the strong electric field associated with the high intensity available from a short pulse of light enables strong-field ionization (SFI) (or excitation) such as multi-photon and tunnel ionization [2]. In addition, once excited to the conduction band, the electrons may interact again with the laser field and possibly induce additional excitation by collisions with bound electrons [3]. This increases the density of 'free' (conduction-band) electrons rapidly in an avalanche process, and eventually the material may break up due to the high electron density.

In this review, we will only discuss laser ablation dynamics, where the initial absorption is dominated by this non-linear absorption (or possibly defect-induced absorption). This limits us to materials with a band gap which exceeds the photon energy, i.e. several electron volts. In addition, the review will focus on femtosecond-laser-induced processes, thus excluding some of the phenomena which become very important for longer pulses. For instance the use of femtosecond pulses allows us to assume that the material motion is essentially frozen for the duration of the laser pulse, and in many situations even charge- and heat transport is also minimal during the pulse. Finally, this review will focus on surface excitation, since this is the relevant process for laser ablation and thin-film growth.

As discussed in section 3, the plume emitted from a target irradiated by an ultrashort laser pulse has different characteristics than those obtained with conventional lasers. In section 4 it is thus shown that the specific interaction mechanisms of short-pulse excitation can be applied to produce thin films with characteristic properties. The strong-field excitation means that any material can be excited, including a material transparent to the laser. The highly localized excitation minimizes the formation of larger particulates from the target. Instead the emitted material consists of a combination of atoms (or ions) and nano-sized clusters. It will be discussed that ultrashort laser pulses appear to be efficient for the formation of films of nanoclusters. Finally, the stoichiometry of the films and its resemblance to the target material is a topic of ongoing discussions, and we will include this property in our review of the properties of currently reported films.

Reviews on different aspects of ultrashort-pulse laser ablation of dielectric materials have previously been published. Reference [4] gives a comprehensive description of the early investigations of laser-induced break down, including the results from early short-pulse excitation studies. A review with emphasis on multi-shot and bulk effects is presented in [5].

Many aspects of short-pulse ablation with an emphasis on polymer ablation have been reviewed in [6], while [7] provides a broad overview of short-pulse laser excitation of materials. A couple of recent reviews provide good overviews of bulk modifications of dielectric materials and the many possible photonic applications [8, 9].

1.1. The development of the femtosecond laser

The development, which has led to modern femtosecond-laser systems, was started shortly after the invention of the laser just over 50 years ago. The history of ultrashort-pulse lasers has been extensively reviewed elsewhere [10–14]. In this paper we will briefly summarize the steps that led to the situation of today, where ultrashort laser systems are no longer *topics* of research in highly advanced laser labs, but rather widespread *tools* for a broad range of research and, more recently, also industrial and medical applications.

The basis for generation of ultrashort laser pulses was formed with the advent of passive mode-locking techniques. The first lasers to break the picosecond limit were based on organic dyes in combination with a saturable absorber in a so-called colliding-pulse mode-locking (CPM) scheme (for a review of the early years of femtosecond lasers; see, e.g., Shank [15]). In spite of their tricky operation, the CPM lasers were the workhorses of the first ten years of femtosecond science. Simultaneously, much effort was devoted to the development of solid-state gain materials, and a major breakthrough was obtained, when self-modelocking in a Ti : sapphire laser was discovered by de Spence *et al* [16]. This provided an oscillator which with small modifications are still a key ingredient in many commercial laser systems today.

An equally important technology was the introduction of chirped-pulse amplification by Strickland and Mourou [17], which allowed the amplification of short pulses to high energies in table-top (and later even one-box) setups. The ingenious idea is to reduce the peak intensities (and thereby avoid non-linearities) by stretching the pulses in time before amplification. This prevents the need for expensive large-aperture optics and amplifiers. Stretching and compression of pulses are based on different dispersion techniques, and proper managing of dispersion is important for both the generation and the amplification of ultrashort pulses.

In parallel with the Ti : sapphire-based technology, a fiber-based femtosecond technology has emerged. Fiber oscillators using a variety of mode-locking techniques have been available for many years (for reviews, see [18, 19]). Initially the fiber lasers were limited to fairly low pulse energies in order to avoid fiber non-linearities, but recent developments have led to commercial systems with pulse energies in the range of interest for laser ablation (several microjoules per pulse). Since these systems can potentially deliver very high average powers [20], their application in future thin-film manufacturing setups is very promising.

1.2. Early investigations of femtosecond light–matter interaction

The first investigations of femtosecond-laser induced material modifications were reported shortly after the advent of the

CPM laser, in an investigation of ultrafast melting of silicon by Shank *et al* [21]. Femtosecond-laser ablation experiments seem first to have been demonstrated by Kuper and Stuke using 500 fs UV pulses on polymers [22], and the first investigations of a dielectric, SiO$_2$, by Ihlemann *et al* used similar pulses [23]. The benefits of highly localized interactions were described in terms of a much reduced heat-affected zone (HAZ) by Kautek and Kruger [24], while the effect of the pulse duration on the observed threshold was first investigated in Du *et al* [25] (see also section 2.3.2). The possibilities of producing sub-wavelength features in metal foils were thoroughly discussed in Pronko *et al* [26], and at about the same time, other groups started to report on investigations of ultra-short pulse laser ablation of metals [27, 28].

The interaction between femtosecond-laser pulses and dielectric materials has several important characteristics. First, since the interaction is highly non-linear, the excitation can be extremely localized to a small focal volume. This is further enhanced by the minimized heat transport for an ultrashort pulse. Second, the excitation can be driven in *all* materials even if the photon energy is less than the band gap of the material. Finally, the excitation is much more deterministic than for (long-wavelength) pulses of a longer pulse duration, where the response depends statistically on the number of defect sites or thermally excited electron–hole pairs.

All these properties are important for femtosecond-laser based nano- and micro-processing as well as for thin-film generation, as will be discussed in greater detail in the following sections.

1.3. Thin-film production: in general

The production of thin films has played an important role for the technological level of the society. In principle, thin film or coating technology serves to change the surface properties of a bulk material, for example to make a glass reflecting by coating it with aluminum, to make a transparent panel conductive by adding a thin layer of a semiconducting, transparent material, to reduce the reflection of optical surfaces by an anti-reflective coating or to make wear-resistant tools by coating them with tribological layers. This coating is typically a few hundred nanometers thick. The progress of coating technology has been closely connected to the development of vacuum and surface characterization methods, which gradually entered from scientific laboratories into production facilities.

Until the mid-1970s, evaporation deposition was the preferred technique. Evaporation deposition is a straightforward technique, which can be performed with few components: a heater, a simple vacuum system, and a substrate. However, the technique requires samples of low melting point, which means that highly heat-resistant materials, in particular molybdenum and tantalum, were difficult to use in an evaporation process. Another problem was the large material consumption, because the evaporated material leaves the target with directions characterized by a cosine distribution [29]. Even with the substrate placed opposite to the target and facing it, a large amount of the evaporated material was deposited on the wall and windows of the evaporation chamber. An

additional problem occurred for multi-component targets of components with different binding energies, e.g. metal alloys. The most volatile component will evaporate first, such that the chemical composition of the film becomes non-uniform in depth—or in the worst case it leads to a film completely without the non-volatile components of the target.

A breakthrough in film deposition appeared in 1974 when the magnetron sputtering deposition was invented [30]. Until then, sputtering deposition had been a very slow process. The discharge in a magnetron is kept in the vicinity of the target and can lead to deposition rates exceeding $1 \, \mu m \, min^{-1}$. The sputtering-ejection process is directional in the sense that the sputtered flow from the target is strongly peaked in the forward direction (just as the laser-ablated flow, see section 3.5), which strongly reduces the material loss outside the substrate area. Sputtering deposition has turned out to be a reliable technique for one-component material as well as for many multi-component target combinations and can also be used for hard materials. Since the sputtered particles arrive at the films with super-thermal energy (similar to laser-ablated particles, section 3.3), the particles are mobile on the substrate and later on the film surface. This gives a much better adhesion to the substrate and a higher crystal quality compared with evaporation deposition. However, also for the fundamental sputtering process, the ejection rate depends on the binding, and the preferential sputtering by negative ions on the growing film will occur, eventually leaving a film of a stoichiometry (i.e. relative atomic composition) different from that of the target. This problem can be solved by different designs of the sputtering geometry, e.g. sputtering targets for high-temperature superconductors YBCO, may, for example, be shaped as a ring. For the moment film production by lasers, pulsed-laser deposition (PLD), cannot compete commercially with the established sputtering-deposition technique except for a few, special materials. A major feature for the industrial production of sputtering deposition is the possibility of upscaling the systems such that areas 100–1000 cm^2 of arbitrary shape can be coated within several hours. This ability is superior to any present-day laser-based deposition system.

1.4. Early film production by lasers

The development of film production by lasers has largely followed the development of lasers [31]. After the high-power ruby lasers became available, the attempts to use lasers for film deposition gradually began. The first PLD experiment carried out by Smith and Turner was intuitively simple, but did include some essential features which are still basic characteristics today. The authors used the laser energy to drive a flash evaporation with a short thermal cycle in order to achieve stoichiometric control, but did not succeed in achieving the same composition in the film due to insufficient laser peak power and very long pulses [32]. The rapid progress in other types of lasers made the CO$_2$ laser available, and the first films were made with this laser in 1969 [33]. However, since many materials have a large absorption depth at the $10.6 \, \mu m$ wavelength, a liquid layer was formed, which frequently caused undesirable effects such as splashing of micrometer-sized particulates (an effect which also frequently occurs in

present-day nanosecond PLD). The general trend in the first decade after the invention of the laser was that experiments were usually single efforts without any systematic work to optimize experimental parameters or explore the underlying physics.

In the 1970s, two significant developments accelerated the film production by PLD. Reliable electronic Q-switches became available and made it possible to use short, powerful pulses on the targets. Also, improved, reliable second-harmonic generators made it possible to deliver shorter wavelength in the pulses, usually with shallower absorption depths. These two improvements meant that the film quality was improved and that stoichiometric material transfer from target to substrate was achieved occasionally. In the mid-1970s even films of the very complex composition, ReB_{22}, were produced [34].

Even though the number of groups that employed PLD grew steadily because of the improved quality of commercial lasers, the PLD community was relatively small. However, in 1987 Venkatesan's group showed that thin films of the new high T_c super conductors with perovskite structure, YBCO, could be fabricated easily with PLD, and could even keep the superconducting functionality [35], while laboratories with other deposition methods were struggling to obtain the correct stoichiometry. This was the work that triggered the worldwide use of PLD. The materials-research community suddenly realized that the PLD concept was a simple and fast tool for exploring and producing new film materials at the frontiers of materials science.

The success of PLD is primarily determined by the simple concept and the decoupling of the experimental parameters:

(i) The energy that drives the material transfer from target to substrate originates from an external source, the laser. It can be directed very precisely on a desired spot on target and does not involve any discharge in a background gas in the vacuum chamber.

(ii) The background gas and pressure can be chosen conveniently without any restraints for discharge formation as in sputtering deposition. It means that the ablation can be carried out in an oxygen background gas such that any loss of oxygen during the material transfer to substrate can be compensated by intake from the background gas. This has been a major feature for the preservation of stoichiometry in the oxide films.

(iii) The substrate can be placed at any convenient distance from the laser spot and can be kept at any temperature from room temperature up to more than $1000\,^{\circ}C$ by an external heater as opposed to sputtering deposition, where the adjacent discharge heats the substrate.

(iv) The number of pulses and the pulse energy of the laser can be controlled easily. It means that complete (interface)-layers can be formed after a precise number of pulses, in particular if the growth is monitored with reflection high-energy electron diffraction (RHEED). This precise deposition has made surface engineering of oxides at the monolayer level possible [36].

At the commercial level, sputtering deposition is still the dominant technique. High power, commercial lasers are still expensive, and the precise cleaning of laser optics and alignment of laser beams can still be an obstacle in an industrial environment. Another problem is the occurrence of particulates, micrometer-sized particles ejected from the target, which can be seen on a major part of the films [31]. The number of particulates can be reduced by employing shorter wavelengths, e.g. in the UV-regime, and as discussed in section 4, also by short pulses in the femtosecond range.

The new reliable femtosecond lasers, which became available up to the year 2000, were primarily used for ablation studies rather than film production by PLD. The pulse energy was rarely sufficient for the necessary high ablation rate, but nevertheless, the first films produced by femtosecond-laser PLD appeared just before 2000. The first reports dealt with diamond-like carbon films produced from graphite [37] or frozen acetone [38]. The first film of a dielectric, ZnO, was produced by Okoshi *et al* [39] and by Millon *et al* [40]. Today more than 20 dielectric materials have been deposited as thin films by femtosecond-laser PLD, as reported in section 4.

2. Basics of femtosecond ablation dynamics

2.1. Phenomenological description

Light–matter interaction is a fundamental process in nature. Due to the much smaller mass of electrons relative to the nucleus, it is a good approximation to state that light is absorbed by electrons. For an initially free electron, this process is often denoted as inverse bremsstrahlung. In spite of the importance of the nearby nucleus, in many cases the simplified picture of electron (only) excitation is useful. Since electrons are fermions, in order for excitation to be possible, the electron must be transferred from its initial (populated) state to an available (unoccupied) final state. In free atoms, this gives rise to discrete absorption lines corresponding to bound–bound transitions plus an absorption continuum for photon energies exceeding the ionization potential.

It is well known from solid-state physics that when atoms are aggregated into solid materials, the quantized energy levels of the compound system become bands. Depending on the constituent atoms and the precise stoichiometry of the material, the band structure exhibits different characteristic properties, which qualifies the material as being a metal, a semiconductor or an insulator. For metals, the highest-energy electrons occupy partially filled bands, which means that there is no threshold for the excitation of electrons from occupied to unoccupied states. This has many implications for the properties of metals, but let us for now focus on the ability of metals to absorb light of 'any wavelength'. This being said, absorption is maybe not the most striking optical property of metals: due to the high electron conductivity, an incoming electric field is in fact very efficiently screened, and a reflected field is generated, which typically contains a large fraction of the energy. Nevertheless, absorption of a few percent of the light energy will still happen.

In contrast to the situation for metals, for semiconductors, the highest-energy electrons (at low temperature) occupy a

completely filled band, the valence band. In order to excite an electron, it is thus necessary to supply enough energy to bridge the gap to the first unoccupied band (the conduction band). For semiconductors this band gap is small enough for an appreciable fraction of electrons to be excited to the conduction band simply by thermal excitation; hence the term semiconducting. In addition, semiconductors are strongly influenced by the presence of impurity atoms, which can supply additional energy levels, for instance inside the band gap. The optical properties of clean (or *intrinsic*) semiconductors are characterized by a threshold photon energy, which must be reached in order to allow excitation of electrons from the valence to the conduction band.

The term insulator is used for materials where the band gap is large enough for very few charges to be thermally excited to the conduction band; it is electrically insulating. At the same time, the band gap of an insulator is typically so large that optical excitation is not possible with infrared and visible radiation. The term dielectric is often used interchangeably with insulator, particularly when the response of the material to external electric fields is discussed: the electric field, which cannot transport the electrons over macroscopic distances, may still polarize the charges locally inside the insulator, and the polarizability is quantified by a dielectric function. Dielectrics may or may not be transparent: although their energy levels do not allow absorption (of visible light), the material may still exhibit enough scattering for even thin samples not to be capable of transmitting unperturbed light fields. They are then instead denoted as translucent.

This brief description of light–matter interaction gives us the framework for discussing laser excitation of insulators/dielectrics. As mentioned previously, the excitation of dielectrics typically requires UV wavelengths in order to bridge the band gap. Consequently, excimer lasers are useful light sources for dielectrics. There is, however, also the possibility of using intense infrared laser fields as, e.g., CO_2-lasers. This is due to the absorption of IR light corresponding to vibrational excitation of the solid possibly in combination with absorption by thermally excited electrons or impurity-donated electrons. These mechanisms are efficient for large-scale drilling and cutting, but less appropriate for micro- and nano-processing due to the statistical nature of the process, which results in less predictive behavior and typically quite rough machined areas that are strongly influenced by thermal damage [41, 42]. When discussing laser-ablation for thin-film generation, the problem is similar: The statistical nature as well as a strong thermal component of the ablation process leads to release of material with a stoichiometric composition, which may differ significantly from that of the native material; see section 4.3. However, as briefly mentioned in the introduction, this can potentially be different when using the strong-field excitation associated with ultrashort laser pulses; see section 4.3.

To get an idea of what a strong laser field is, a comparison of the electric field of the light with that acting on an electron in a ground-state hydrogen atom is appropriate. The electron in a hydrogen atom experiences an electric field from the nucleus of approximately 5×10^9 V m^{-1}. To generate such an electric field
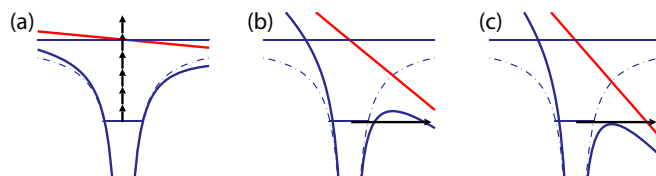

Figure 1. A schematic of the three regimes of SFI. The dashed–dotted lines represent the Coulomb potential without an electric field, while the blue solid lines show the potentials in the presence of the laser fields which are sketched with the red solid lines. (*a*) shows the multi-photon regime, where multiple photons are absorbed for an electron to become free; (*b*) shows how in the tunneling regime, an electron can be liberated by tunneling through the barrier; (*c*) shows the over-the-barrier regime, where the barrier is suppressed enough that the electron can escape freely from the atom.

by light, an intensity of 3.5×10^{16} W cm^{-2} must be applied; this is denoted as one atomic unit of intensity. In the early years of laser ablation and thin film production, due to the available laser sources, the applied light fields were very weak compared with this intensity, which means that the initial light–matter interaction was essentially in the perturbative limit. However, with the advent of ultrashort-pulse lasers this is no longer the case.

The requirement for ionization of an atom that the incoming photon energy must exceed the binding energy of the electron is only valid for weak light fields. As the electric field becomes stronger, non-linear effects will occur and multi-photon excitation becomes possible. When the intensity approaches the atomic unit of intensity, the electric field becomes sufficiently strong to strongly perturb the Coulomb potential. In this case the electron may tunnel through the suppressed barrier and ionization can occur. When the fields become even stronger, the potential barrier can be suppressed sufficiently to free the electron directly into the continuum without tunneling, denoted by over-the-barrier ionization. These three strong-field regimes are sketched in figure 1.

In addition to the large differences in the optical properties between insulators, semiconductors and metals, the energy levels of the materials also have a strong influence on the response of the material to an excitation. Most importantly, the thermal and electrical conductivity is much smaller for dielectrics than it is for metals. The low thermal conductivity holds the promise for quite localized interactions when pulsed light sources are used. This is a separate reason for employing ultrashort laser pulses. The reduced electric conductivity has a more indirect influence on the material response. When a strong light field excites a large number of carriers from the valence band, the material potentially becomes unstable: the valence band corresponds to the 'bonding orbitals' of the solid, so that the restoring forces of the solid vanish at high excitation. For metals, the bonding is typically restored on a fast time scale, since the excited electrons are replaced by 'cold' electrons transported into the laser-excited volume. For semiconductors this is different, and signatures of so-called 'ultrafast melting' has been observed (for a review, see [43]). For dielectrics, the destabilization is even more pronounced and a high excitation level will therefore with high probability

lead to material fragmentation. The detailed description of mechanisms for material fragmentation will be discussed in sections 2.3.4 and 3.

2.2. Experimental observables related to ablation dynamics

There are three main categories of information, which can be extracted from laser-ablation experiments: the geometrical (or morphological) properties of laser-generated features, optical measurements on the laser-excited dielectric materials, and structural measurements of the material around ablated features. These three groups of experimental observables provide complimentary information.

In order to characterize the strength of the laser field, the two quantities fluence, F, and intensity, I, are both used. They are related by $F = \int I \, dt$, where the integral is over one laser pulse. Since the intensity is the energy per unit area per unit time, the fluence is the energy per area supplied over the entire pulse. This is a relevant quantity, if the material response happens on a time scale which is long compared with the pulse duration. This is *not* the case for short-pulse excitation of dielectrics. On the other hand, it is also not enough to provide the intensity in order to predict the material response, because the pulse duration will strongly influence the evolution of the process. In the literature, most authors specify the experimental conditions by providing the laser fluence in addition to the laser pulse duration.

When inspecting the reported experimental work, another important characteristic to note is whether the observations are for single- or multi-pulse irradiation. As will be discussed further in section 2.7, the observed characteristics change significantly for a dielectric that has been irradiated before. In order to study the properties of the intrinsic material, it is thus necessary to rely on single-pulse experiments.

Another related problem is that of sample quality. For high-band-gap materials, the presence of even small concentration levels of impurities or defects can have a significant impact on the observed response to short-pulse excitation. Electrons from states that are located in the band gap are ionized much more easily by the laser, and once excited into the conduction band, these seed the subsequent excitation, e.g. by collisional excitation. Similarly, the sample surface morphology can have a significant impact on the observed behavior, both due to the effect on the optical properties (reflectivity, scattering, local field enhancement etc) and due to the possibly lower damage threshold (e.g. lower cohesive energy for low-coordinated atoms).

2.2.1. Morphological investigations.
Much information has been obtained by inspecting the geometry of laser-generated holes. Typical experiments undertake measurements of the hole geometries *ex situ* using an optical microscope or a scanning-electron microscope (SEM). In order to obtain depth profiles of the holes, one may employ optical techniques based on interferometric methods (e.g. interference microscopy) or atomic-force microscopy (AFM), which allows measurements to be carried out also on small and shallow structures and does not rely on an unambiguous surface reflectivity. AFM

measurements are, on the other hand, fairly limited in their transverse-scanning and depth range. In a few cases, transmission-electron microscopy (TEM) in combination with focused-ion-beam (FIB) milling has been used to obtain very detailed information about the cross section of laser-formed holes [44]; see also section 2.2.3.

While the most precise methods for obtaining geometrical information are thus typically undertaken after ablation is completed, a few techniques for *in situ* real-time measurements have also been proposed. One implementation uses a variation of time-gated imaging employing the time-structure of the back-scattered light from the ablating beam itself [45], while another is based on a built in interferometric technique, which is essentially a variation of an optical-coherence-tomography setup [46].

Parametric investigations of hole sizes, e.g. hole diameters or hole depths, as a function of laser parameters (intensity or fluence) provide an attractive way for extracting the threshold for laser damage and/or ablation. Such threshold determinations typically employ some kind of scaling law. The scaling law for diameter measurements is particularly simple. As pointed out originally for picosecond-pulse lasers by Liu [47], if a spatially Gaussian laser beam interacts with a material, which has a specific threshold for modification, the diameter of the modified (molten, damaged, ablated, etc) region on the surface must follow the scaling

$$D^2 = 2w^2 \ln\left(\frac{F}{F_{th}}\right), \tag{1}$$

where w is the laser spot size at the surface, i.e. the radius where the fluence of the Gaussian beam has dropped to the $1/e^2$ level, and F_{th} denotes the threshold for the material change, here expressed in terms of the threshold fluence. The expression above is valid as long as the radial propagation of energy can be neglected. Note that since energy and fluence are proportional, the right-hand side may equally well be expressed in terms of pulse energies. In this case the expression can, in fact, be used to determine the laser spot size *in situ*, although some authors point out that care must be taken with this approach when working with very high band-gap materials [44, 48].

While the scaling of the diameters is thus quite well established, the scaling of hole depths is more unclear. It is well known that for a linearly absorbing material, the exponential deposition of energy *versus* depth often leads to ablation rates that depend logarithmically on the applied fluence [24, 27, 28, 41, 49, 50]. However, as discussed above, the absorption of short light pulses in a dielectric is highly non-linear, so such simple scaling cannot be expected. Nonetheless, for experimental determinations of thresholds, a logarithmic extrapolation is still often applied. Various modifications of the simple logarithmic dependence have been suggested in situations, where the absorption is dominated by multi-photon absorption of a given order; see, e.g., [51–53]. In recent investigations, much insight has been obtained by comparing measurements of ablation depth *versus* fluence to numerical simulations of the ablation dynamics in various approximations; see section 2.4.

2.2.2. Optical investigations. Complimentary information about the highly excited dielectric material can be obtained from optical measurements. In contrast to the morphological studies, such measurements can readily be undertaken *in situ* and by employing the standard pump–probe techniques of ultrafast science, time-resolved measurements can be used to determine valuable dynamical information.

As already mentioned, the first experimental investigations of femtosecond-laser-induced material modifications were melting of silicon. These investigations were in fact based on time-resolved measurements of the material reflectivity, using this property to indicate when a phase transition had occurred [21]. The first time-resolved investigations on dielectrics were carried out by Audebert *et al* using the powerful technique of spectral interferometry to investigate SiO_2 at moderate fluences [54]. By measuring the phase shift and the fringe contrast as a function of time, the authors could determine both the real and the imaginary parts of the refractive index of the laser-excited volume (for a review of this technique, see Mao *et al* [55]). Other early examples of optical measurements on a dielectric are given in [56, 57], where time-resolved microscopy provided the sample reflectivity as a function of time after excitation at intensities well above the damage threshold.

Various versions of such optical measurements— both interferometric and measurements of reflectivity and transmission—have provided important information about highly excited dielectrics; see sections 2.4 and 2.5.

2.2.3. Atomic-scale structural characterization. A few measurements have been directed toward measuring the local material structure of the region around laser-ablated holes. The combination of FIB and TEM has allowed Hsu *et al* to investigate structural defects in single-crystalline diamond samples following excitations [44]. Furthermore, in a recent paper, the technique of near-edge x-ray absorption spectroscopy was used by Seuthe *et al* for a detailed investigation of structural changes in potassium–magnesium silicate glasses following femtosecond-laser pulse irradiation [58]. A related, albeit more indirect, method for retrieving the local structure is Raman spectroscopy. This method has proven particularly useful for investigating bulk material modifications as originally demonstrated in Chan *et al* [59] and recently used by several groups; see, e.g. [60] and references therein.

While these experiments all represent measurements undertaken *post mortem*, it is expected that very detailed information about highly excited dielectrics and the ablation process in the future may be obtained by extending the methods used for investigating the structural dynamics of semiconductors (reviewed in [43]) to dielectric materials. This will become possible due to the development of new high-intensity x-ray sources based on free-electron lasers (see, e.g., [61]).

2.3. Describing highly excited dielectric materials

The overall mechanisms involved in dielectrics excited by ultrashort pulses are sketched in figure 2. Initially, an
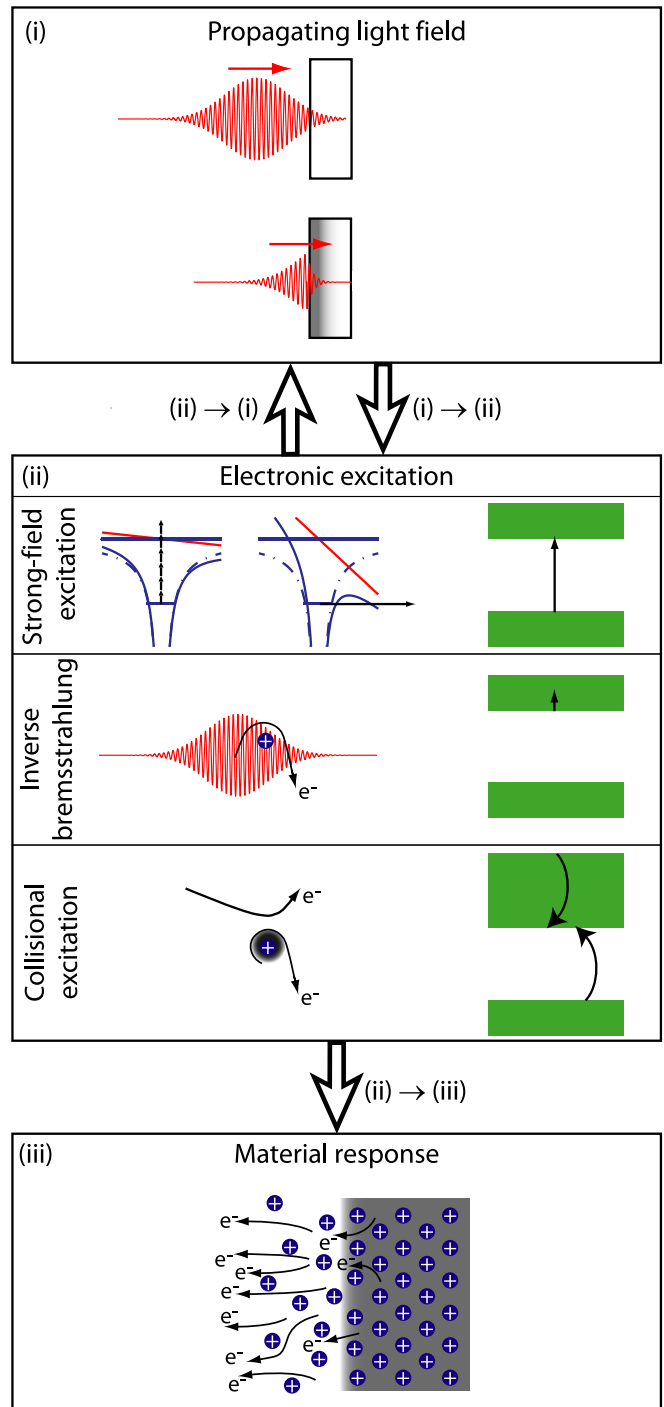
Figure 2. A schematic of the interrelation between the exciting light field and the dielectric material. The electronic excitation (box (ii)) is strongly coupled with the light absorption (box (i)), and the electronic excitation gives rise to the material response (box (iii)), as described in detail in the text. In box (ii), the drawings on the left indicate a schematic of the three different excitation mechanisms, while the sketches on the right show the associated effect on the electronic population in the valence and conduction bands indicated by lower and upper green boxes, respectively.

intense light field propagates into an unperturbed material (box (i) in the figure). With no 'free' electrons present, this light field is only attenuated by strong-field (multi-photon) absorption. These absorption processes generate electrons

in the conduction band; see box (ii). Specific models for the strong-field excitation will be discussed in more detail in section 2.3.1.

As soon as a non-vanishing density of 'free' electrons has been generated, these will change the optical properties of the material and hence influence the propagation of the light field, as symbolized by the arrow (ii) → (i). While the occurrence of this free-electron absorption is clear, the specific relation between the density of electrons and the optical properties is unfortunately less clear, as will be discussed in detail in section 2.3.3.

An important coupling mechanism, which should also be accounted for, is that the free-carrier absorption (also denoted as inverse bremsstrahlung) gives rise to additional electronic excitations. Depending on the specific model applied for the electrons (box (ii) in figure 2), this can be described as an increased electron temperature or as additional electronic excitations; see also section 2.3.2.

The mechanisms of electronic excitations are in fact even more complicated than the aforementioned contributions from strong-field and free-carrier excitation: when the electrons in the conduction band are heated sufficiently, they have the possibility of inducing collisional excitation of other electrons from the valence band. This so-called impact ionization (or excitation) is the basis for charge multiplication or 'avalanche' processes, which must be included in the description of electronic excitation (box (ii) in figure 2).

Finally, depending on the laser-induced process that is under investigation, one must have a model of how to convert the electronic excitation to a given material response. If, for instance, laser ablation is considered, the electronic excitation must be converted to an ablation signature. For instance, one can assume that material, where the density of excited electrons exceeds a certain 'critical density', will be ablated. The mechanisms for material removal as well as other possible descriptions of electron-material coupling (the arrow (ii) → (iii) in figure 2) will be discussed in section 2.3.4.

2.3.1. Strong-field excitation. As already mentioned, the initial excitation of carriers by a field with photon energy below the band gap involves a strong-field excitation process. In accordance with the literature, we will often use SFI to denote excitation to the conduction band, although electrons here are strictly speaking not free.

At fairly low fields, the dominating excitation mechanism is multi-photon excitation; see figure 1. In the perturbative limit, the transition rate for an N-order photon absorption is proportional to I^N, as it has been used extensively [41]. However, already at modest intensities, it is necessary to consider the AC Stark shift of the bands, which increases the band gap. The ponderomotive energy, U_p, for a free electron is the cycle-averaged kinetic energy of its oscillating motion in the electromagnetic field, which is simply

$$U_p = \frac{e^2 E^2}{4m_0 \omega^2}, \qquad (2)$$

where ω and E are the angular frequency and the electric field amplitude of the light, respectively, while e and m_0 denote the

electron charge and mass. A convenient form for numerical evaluation of this expression, $U_p = 0.93\,\text{eV} \cdot (\lambda/(1\,\mu\text{m}))^2 \cdot I/(10^{13}\,\text{W cm}^{-2})$, clearly shows that at the intensities of relevance for short-pulse ablation, the ponderomotive shift can easily exceed the photon energy. Since the shift of the conduction band relative to the valence band will be of this order of magnitude, the order, N, of the lowest accessible process will increase, and therefore the simple perturbative scaling, I^N, soon becomes invalid.

A quantitative model of the SFI yield was proposed by Keldysh in 1965 [2]. Here, the quantitative results of the SFI will only be stated for a solid with a dispersion relation given as

$$\epsilon_s(p) = \Delta \left(1 + \frac{p^2}{m\Delta}\right)^{1/2}, \qquad (3)$$

where Δ is the band gap, m is the reduced mass of the effective electron and hole masses and p is the electron momentum. An important parameter for describing the SFI is the so-called Keldysh parameter, γ, given as $\gamma = \omega\sqrt{m\Delta}/(eE)$.

The strong-field excitation rate given in [2] is expressed in terms of the complete elliptic integrals of the first and second kind, $\mathcal{K}$ and $\mathcal{E}$, as well as the Dawson integral, Φ. Note that here we will use the convention of Abramowitz and Stegun [62] (as well as many numerical programs) and express $\mathcal{K}$ and $\mathcal{E}$ as functions of the parameter $m_{\text{ellip}} = k_{\text{ellip}}^2$, where k_{ellip} is the so-called modulus, used by Keldysh in [2]. To simplify the following expressions, let us follow [63] and introduce the two auxiliary gammas, $\gamma_1 = \gamma^2/(1+\gamma^2)$ and $\gamma_2 = 1/(1+\gamma^2)$. Furthermore, let x denote the effective ionization potential in units of the photon energy,

$$x = \frac{2}{\pi} \frac{\Delta}{\hbar\omega} \frac{\mathcal{E}(\gamma_2)}{\sqrt{\gamma_1}}. \qquad (4)$$

The SFI rate can then be written as

$$W = 2\frac{2\omega}{9\pi}\left(\frac{m\omega}{\hbar\sqrt{\gamma_1}}\right)^{3/2} Q(\gamma, x)$$
$$\times \exp\left(-\pi\lfloor x+1\rfloor \frac{\mathcal{K}(\gamma_1) - \mathcal{E}(\gamma_1)}{\mathcal{E}(\gamma_2)}\right), \qquad (5)$$

where we have used

$$Q(\gamma, x) = \sqrt{\frac{\pi}{2\mathcal{K}(\gamma_2)}}$$
$$\times \sum_{n=0}^{\infty} \exp\left(-n\pi \frac{\mathcal{K}(\gamma_1) - \mathcal{E}(\gamma_1)}{\mathcal{E}(\gamma_2)}\right)$$
$$\times \Phi\left(\sqrt{\frac{\pi^2(\lfloor x+1\rfloor - x + n)}{2\mathcal{K}(\gamma_2)\mathcal{E}(\gamma_2)}}\right). \qquad (6)$$

Note that these expressions have been modified according to [64], where small misprints have been corrected, and an extra factor of 2 due to electron spin degeneracy has been included in all rates. The SFI rate for a specific band gap and specific laser wavelength is plotted in figure 3 (solid red line).

In the limit of $\gamma \gg 1$, i.e. the optical frequency much larger than the tunnel-ionization rate, tunneling within an
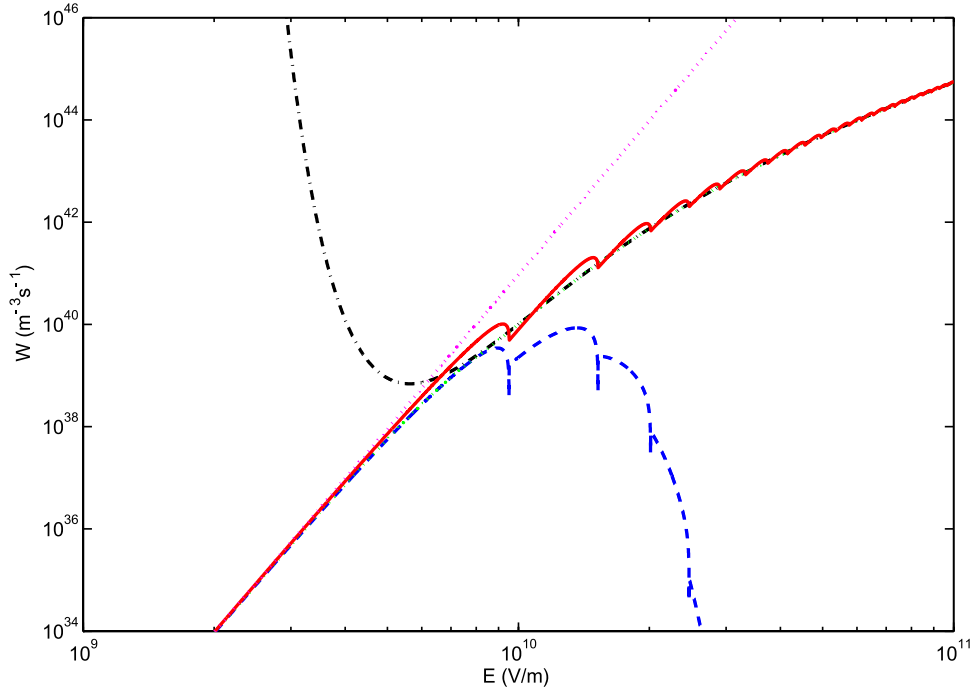
Figure 3. The SFI rate according to Keldysh theory [2] for a specific wavelength (800 nm) and band gap (6.5 eV). The blue dashed line shows the expression for the multi-photon regime, equation (8) (valid only at low fields), while the black dashed–dotted line shows the probability in the tunneling regime, equation (9) (valid only at high fields). The cyan dotted line shows the perturbative limit $W \propto I^5$ or $W \propto E^{10}$ since at a low intensity $N = 5$ with the wavelength and band gap used here. The red solid line shows the full Keldysh SFI rate according to equation (5), while the dotted green line shows one choice for an interpolated curve following [65]. Note for comparison that the graph covers an intensity interval of 1.33×10^{11} W cm^{-2} ($E = 10^9$ V m^{-1}; $\gamma = 10.1$) to 1.33×10^{15} W cm^{-2} ($E = 10^{11}$ V m^{-1}; $\gamma = 0.101$).

optical cycle is not possible, and the system is in the multi-photon ionization regime. In this limit, the effective ionization potential can be expressed as a corrected band gap, $\tilde{\Delta}$, and calculated from $\hbar\omega x$ in the high-gamma limit of equation (4), giving

$$\tilde{\Delta} = \Delta + U_{\mathrm{p}} \tag{7}$$

where U_{p} is given by equation (2) with m_0 replaced by m. The order of the multi-photon process is then $N = \lfloor x + 1 \rfloor \simeq \lfloor \tilde{\Delta}/\hbar\omega + 1 \rfloor$, and the multi-photon ionization probability is given by [2, 64]

$$W_{\mathrm{MP}} = 2\frac{2\omega}{9\pi}\left(\frac{m\omega}{\hbar}\right)^{3/2}\Phi\left(\sqrt{2N - 2x}\right)$$
$$\times \exp\left(2N\left(1 - \frac{1}{4\gamma^2}\right)\right)\left(\frac{1}{16\gamma^2}\right)^{N}, \tag{8}$$

At low intensities, the probability given by equation (8) is dominated by the power-law dependence on intensity corresponding to the last factor, I^N (note that $\gamma^{-2} \propto E^2 \propto I$), in accordance with the perturbative limit discussed above. Curves for the power-law dependence as well as the for full multi-photon expression are also shown in figure 3.

When $\gamma \ll 1$ an electron will have sufficient time to tunnel through the barrier within one optical cycle, and we are in the tunneling regime. The SFI probability is then given as [2, 64]

$$W_{\mathrm{TUN}} = 2\frac{2}{9\pi^2}\frac{\Delta}{\hbar}\left(\frac{m\Delta}{\hbar^2}\right)^{3/2}\left(\frac{\hbar\omega}{\Delta\gamma}\right)^{5/2}$$
$$\times \exp\left(-\frac{\pi}{2}\frac{\Delta\gamma}{\hbar\omega}\left(1 - \frac{\gamma^2}{8}\right)\right). \tag{9}$$

This expression is also shown in figure 3.

The SFI rate is primarily determined from the action of the field on the final state, so the initial state is of less importance to the ionization yield [2]. In the above expressions, it is assumed that no resonances are present. Other proposals for the SFI have been made, where ionization of definite quantum states has been considered; see, e.g. [66]. The mechanisms of the SFE process have also been studied by investigating the dependence on the light polarization. An early study by Du *et al* found the same breakdown threshold for linearly and circularly polarized light and attributed this to a suppression of multi-photon ionization due to collisions [67]. This is in contrast to more recent investigations by Temnov *et al*, which show a clear polarization dependence, with the SFI cross section for linear polarization being 4 to 6 times higher than for circular polarization, depending on the material [68]. Quite recently, the rotation of elliptically polarized light has been investigated by Gertsvolf *et al*, and the observed polarization changes are explained by sub-cycle (i.e. attosecond) phenomena [69]. Other authors have discussed the effects of the holes, which may enhance the SFI by the same mechanisms as enhanced ionization of molecules [70]. The localized effect of holes has been suggested to induce an 'ionization wave', which can sweep quickly through the material, a phenomenon dubbed 'forest fire'. In addition, an extension of the work by Keldysh to more complicated band structures as, e.g. a cosine band structure has been suggested [64, 71, 72].

The combination of the multi-photon and tunnel descriptions is necessary when modeling short-pulse ablation, since a wide range of electric field strengths is typically used

in the calculations. Several authors have used the complete Keldysh expression [63, 73, 74]. A mathematically convenient expression for numerical evaluation of SFI was proposed by Kaiser *et al* [65], who suggested an interpolation between the tunnel-ionization rate, equation (9), and the multi-photon-ionization rate, equation (8), (albeit replacing x with $\tilde{\Delta}/(\hbar\omega)$, equation (7)) in order to give a smooth transition between the two limiting regimes. This spline procedure takes the region of validity of the two expressions into account, but it should be noted that strictly speaking the values are unphysical outside the regions of validity. Figure 3 shows an example of an interpolated curve using this approach. It follows the overall trends of the full calculation quite well, but misses details like the small variations when the multi-photon order changes.

2.3.2. Modeling the electronic excitation. Once electrons are excited into the conduction band, they have the possibility of being accelerated by the laser field and gain sufficient energy to enable excitation of other electrons from the valence band by collisional excitation. As mentioned before, this gives the potential for an avalanche process.

A straightforward model of such 'cascade multiplication' was proposed by Bloembergen already in 1974 [3] as a rate equation with a term proportional to the density of electrons in the conduction band,

$$\frac{\partial n_e}{\partial t} = \eta(E)n_e + \left(\frac{\partial n_e}{\partial t}\right)_{\text{tunnel}} - \left(\frac{\partial n_e}{\partial t}\right)_{\text{loss}}, \qquad (10)$$

where n_e is the total density of electrons in the conduction band, $\eta(E)$ is the probability per unit time for collisional excitation, $\left(\frac{\partial n_e}{\partial t_{\text{tunnel}}}\right)$ is the strong-field photo-ionization rate, and $\left(\frac{\partial n_e}{\partial t_{\text{loss}}}\right)$ allows for losses of excited electrons.

The early investigations of short-pulse excitation of dielectrics in the mid-1990s were modeled by the same expression with the small modification that losses were neglected for sub-picosecond pulses. Du and co-workers measured the threshold for breakdown (defined by the onset of plasma emission) of SiO_2 as a function of the laser pulse duration and found a minimum at a few picoseconds [25]. The phenomenon is explained by the significance of avalanche ionization, which needs time to develop.

In a more elaborate extension of the model by Stuart and co-workers, the electronic excitation was still described by a similar rate equation (albeit with a power-law scaling for the strong-field excitation) in combination with a Fokker–Planck description of the electronic distribution function [75, 76]. This model provided a good description of the ablation threshold *versus* the laser pulse duration up to ~10 ps as shown in figure 4. At longer pulse durations, the experimentally observed threshold fluence in both [25] and [75] is reported to follow a $\sqrt{\tau}$-dependence, which is the anticipated behavior if the threshold is determined by heat diffusion [41]. Please note that the experiments reported in [75, 76] are undertaken with multi-shot irradiation, which influences the observations; see section 2.7. The threshold was defined by any visible damage on the sample when inspected in a Nomarski microscope.

The Stuart papers also discuss the relative significance of the avalanche term, an interesting discussion, which continues
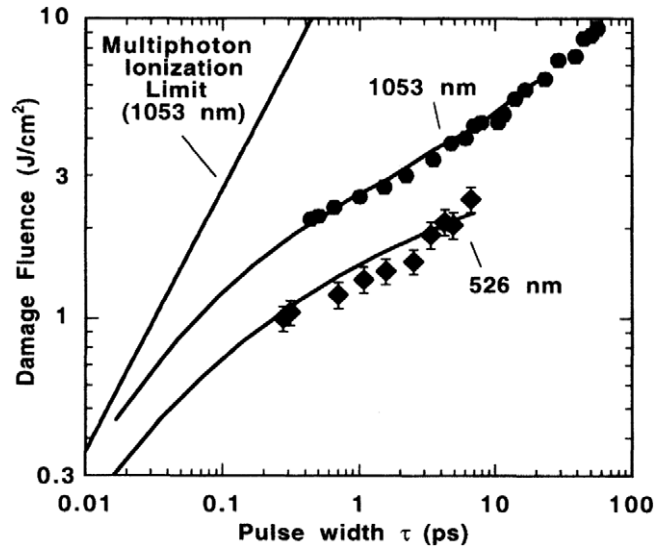

Figure 4. The measured damage thresholds for fused silica at 1053 (●) and 526 nm (♦) together with a theoretical prediction based on a rate-equation/Fokker–Planck description as described in the text. Reproduced with permission from Stuart *et al* [75]. Copyright (1995) by the American Physical Society.
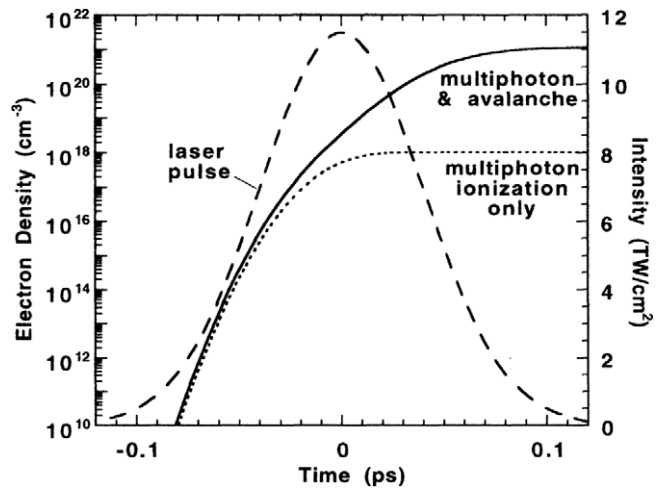
Figure 5. The calculated evolution of the free-electron density for a 100 fs, 1053 nm pulse of peak intensity 1.2×10^{13} W cm^{-2} in fused silica calculated from a rate-equation/Fokker–Planck description. The solid line shows the total electron density including impact ionization, while the dotted line shows the result if the avalanche term is omitted. From Stuart *et al* [75]. Copyright (1995) by the American Physical Society.

even today; see section 2.5. According to [75, 76], the multi-photon ionization starts the excitation, but during a 100 fs pulse, the avalanche term becomes the dominating excitation mechanism. A comparison between the calculation with and without avalanche is shown in figure 5; please note the logarithmic vertical (electron-density) axis.

Improvements of the rate-equation description were suggested by Tien *et al* [63], who use the complete Keldysh description of SFI [2] in combination with more complete expressions for impact ionization. The variation between the different experimental results of threshold *versus* pulse duration for SiO_2 published at that time [25, 75, 77, 78] is discussed in terms of multi-pulse irradiation effects.

Based on optical measurements using time-resolved spectral interferometry (see section 2.2.2), Guizard *et al* proposed an extension of the rate-equation model [79]. For MgO and Al$_2$O$_3$, the phase-shift data could be explained well by the existing rate-equation model using an excitation described as multi-photon absorption. The observed refractive-index change was given by a combination of a positive contribution from the instantaneous Kerr effect and a negative contribution from the free electrons in the conduction band. However, in order to explain the observations for quartz, SiO$_2$, which exhibits a rapid trapping of carriers into self-trapped excitons, the authors introduced a second equation describing the density of the self-trapped excitions, which is coupled to the density of electrons in the conduction band by a constant coupling rate. An extension of this work to describe the absorption soon followed [80], and in some cases more rate equations were needed to account for, e.g., free and trapped holes [81].

In a variation of this approach, Li *et al* [82] employ the single-rate-equation description of excitation but introduce a simple decay term in order to explain the threshold for optical breakdown induced by double pulses. It was soon suggested that the observed decay could be explained by a rapid trapping of carriers into the self-trapped excitons [83].

A modification to the avalanche term of the rate equation equation (10) was suggested by Noack and Vogel in order to account for the time needed for electrons in the conduction band to gain enough energy in order to be able to induce the collisional-excitation process [84]. Based on an estimate for this required time, t_{ion} originally proposed by Kennedy [85], the authors of [84] propose to use the electron density at an earlier time—offset by t_{ion}—when evaluating the collisional-excitation term. This model was recently used to successfully describe the results of a time-resolved spectral interferometry investigation of short-pulse excited thin water jets [86]. Although the delayed-time approach was originally proposed for the modeling of water, it should be of broader applicability, since water can in many ways be viewed as an amorphous dielectric [87].

A model, which emphasizes the importance of electrostatic effects during ablation, is presented by Gamaly *et al* [88]. According to these authors, ablation happens because the ions are pulled out of the solid by energetic electrons. The ablation mechanisms will be discussed in greater detail in section 2.3.4.

The theoretical description by Kaiser *et al* in [65] represents a fundamentally new approach beyond the rate-equation description of the carrier density used so far. Based on microscopic arguments of the physical processes, the authors establish Boltzmann equations for the electrons and phonons and describe their interaction by matrix elements. This results in an appreciable numerical challenge, which for instance for SiO$_2$ amounts to solving 325 non-linear coupled differential equations. The results of the calculation provide important insight into short-pulse excitation. First, the collisional excitation is *not* linear in the free-electron density as assumed in the rate-equation model. Second, the collisional excitation only becomes of significance (for SiO$_2$) at pulse durations
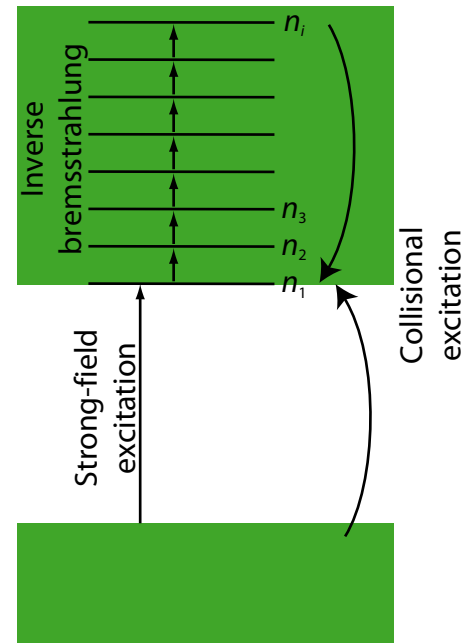

Figure 6. A schematic of the mechanisms included in the MRE model, as described in detail in the text.

above ∼100 fs. The authors do, however, point out that their model is only valid for free-electron densities where electron–ion collision can be neglected, since at high densities inverse bremsstrahlung will lead to higher absorption, and this absorption is not included in the model.

In a recent paper by Schneblanov *et al*, the kinetic approach of [65] was extended to include the complete Keldysh expression for the photo-ionization rate [74]. This investigation predicts a surprisingly low kinetic energy of the electrons promoted to the conduction band and notably smaller than the threshold for collisional excitation.

The reason for the inadequacy of a term, which is simply linear in the total free-electron density, to describe the collisional excitation is discussed in some detail by Rethfeld [89]. The problem is that this approach fails to account for the fact that only the most energetic electrons are able to induce the collisional excitation. In order to provide a model, which is numerically more tractable than the Boltzmann-equation model of [65], Rethfeld in [89] introduces a set of rate equations, which account for the excitation of the 'free' electrons in a simplified and fairly intuitive approach using discrete energy levels to represent the conduction band (figure 6). In this multiple-rate-equation (MRE) model, the electrons are described by a set of discrete energy states with electron densities given by n_j and corresponding kinetic energies of

$$E_{kin}(j) = (j - 1)\hbar\omega, \tag{11}$$

where ω is the laser frequency. The processes included in the model are sketched in figure 6. Strong-field excitation creates the electrons with low energy. These electrons are subsequently excited in the conduction band by the light field (inverse bremsstrahlung) until a critical energy for collisional excitation is reached. In collisional excitation, one electron from the highest conduction-band state collides with an

electron from the valence band and produces two electrons in the lowest-lying conduction-band state (curved arrows in figure 6).

The dynamics of these processes are described by a system of coupled differential equations given by [89]

$$\frac{\partial n_1}{\partial t} = \dot{n}_{\mathrm{pi}} - W_{1\mathrm{pt}}n_1 + 2\eta n_i$$

$$\frac{\partial n_2}{\partial t} = W_{1\mathrm{pt}}n_1 - W_{1\mathrm{pt}}n_2$$

$$\vdots \qquad (12)$$

$$\frac{\partial n_{i-1}}{\partial t} = W_{1\mathrm{pt}}n_{i-2} - W_{1\mathrm{pt}}n_{i-1}$$

$$\frac{\partial n_i}{\partial t} = W_{1\mathrm{pt}}n_{i-1} - \eta n_i.$$

In these equations, $\dot{n}_{\mathrm{pi}}$ is the photoionization rate due to SFI using the interpolated Keldysh equations as in [65] (see section 2.3.1). The photo-excited electrons appear in the lowest conduction band state, since the SFI rate decreases rapidly with increasing energy barrier. The last term in the first and the last equations are due to impact ionization with η being the impact ionization probability. As can be seen, two electrons appear in the first state with each impact ionization event: one from the ith conduction-band state and one from the valence band. The remaining terms describe the intra-band single-photon absorption, which occurs with a probability given by $W_{1\mathrm{pt}}$. In the original papers [89, 90], the one-photon absorption was calculated from a fixed cross section derived from Drude absorption, while in later implementations of the model, the one-photon excitation was chosen in accordance with a description of the time-dependent optical properties of the material [91–94]; see section 2.4. Christensen and Balling [91] also account for a population of final states after collisional excitation, which takes statistics into account, and the saturation of the excitation due to depletion of the valence band is included.

Reference [89] compares the results from the Boltzmann-equation model of [65] with the results from both the traditional single-rate-equation description and the MRE model; see figure 7. As is apparent, the MRE model and the kinetic model give very similar results, while the single-rate-equation models clearly overestimate the importance of impact ionization. We will return to a thorough discussion about the relative significance of the avalanche process in section 2.5.

2.3.3. Optical properties of highly excited dielectric materials.
As soon as the density of conduction-band electrons becomes non-vanishing due to the electronic excitation, the dielectric material changes its optical properties dramatically; see figure 2. The 'free' electrons behave much like the conduction electrons of the metal, and the material acquires metal-like properties in the light response, such as a higher reflectivity and a finite penetration depth.

The optical properties are described by the dielectric and magnetic permeabilities, ϵ and μ, where $\mu = 1$ is often assumed while ϵ is a strongly varying function of both time
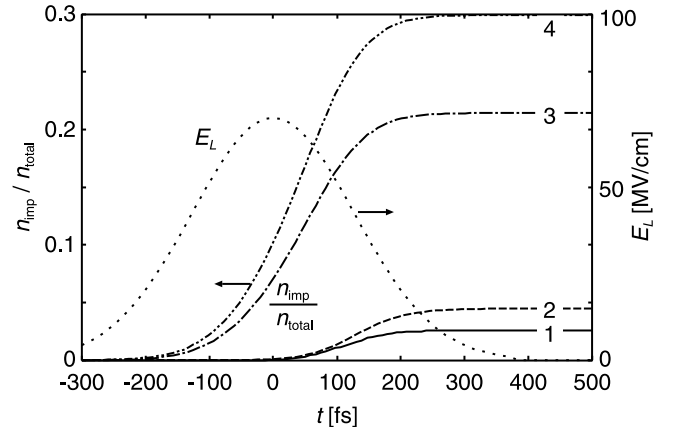

Figure 7. The relative importance of impact-ionized electrons as a function of time during a 300 fs Gaussian laser pulse as calculated from different models. (1) The MRE model, equation (12); (2) The full kinetic approach [65]; (3) and (4) From the single rate equation, equation (10) with different values for the avalanche coefficient. A photon energy of 2.48 eV and a band gap of 9 eV have been applied. Reproduced with permission from Rethfeld [89]. Copyright (2004) by the American Physical Society.

and space following the irradiation, as will be discussed in greater detail in section 2.4. Initially the dielectric function is real, and the (linear) absorption is negligible, but as the excitation proceeds, ϵ acquires an imaginary part, which means that dissipation sets in [95]. The complex refractive index can be defined by $n + i\kappa = \sqrt{\epsilon}$, where n and κ are both real. For a slowly varying dielectric constant, the simplest solutions to Maxwell's equations are plane waves with complex propagation constant (wave number) $k = (n+i\kappa)\omega/c$, so that n denotes the normal refractive index and κ the extinction coefficient. Note that since the electric field then decays as a function of depth (denoted by z) as $\exp(-\kappa\omega z/c)$, the intensity drops with a characteristic absorption coefficient $\alpha = 2\kappa\omega/c$, i.e. an absorption length $1/\alpha = c/(2\kappa\omega) = \lambda/(4\pi\kappa)$. As κ increases, the absorption length drops to a fraction of the laser wavelength, consistent with the metal-like description.

An obvious way to describe the optical properties is to apply the well-known Drude model, which can be derived by a classical description of a free-electron gas [96]. The electrons are accelerated by the time-varying field and their momentum is scattered with a rate Γ. This carries through to the conductivity and adds an imaginary term to the dielectric function, which becomes

$$\epsilon(\omega) = 1 - \frac{\omega_{\mathrm{p}}^2}{\omega^2 + i\omega\Gamma}, \qquad (13)$$

where the plasma frequency is given by

$$\omega_{\mathrm{p}}^2 = \frac{n_e e^2}{m_0 \epsilon_0}, \qquad (14)$$

which is determined by the density of electrons, n_e, in the conduction band.

Note that in order to account for the effects of the bound electrons inside the solid, one should really replace the 1 in

equation (13) by the square of the refractive index of the unperturbed material, n_0^2. In addition, Guizard *et al* [97] point out that, as the excitation progresses, this contribution should really decrease in accordance with

$$\epsilon(\omega) = \left(1 + \frac{3(n_v - n_e)\chi}{3 - (n_v - n_e)\chi}\right) - \frac{\omega_p^2}{\omega^2 + i\omega\Gamma}, \qquad (15)$$

where n_v is the valence-electron density (before excitation) and χ is derived from the Clausius–Mossotti equation [96] such that the real part equals the refractive index of the material prior to excitation.

An important complication is somewhat hidden in these expressions for the dielectric function, since the electron-momentum scattering rate is needed. In many treatments, Γ has simply been taken as a constant [97–100] or used as a constant fitting parameter in order to obtain agreement with experimental data [86, 101].

In general, the scattering of the electrons contains several components: (i) electron–phonon scattering (dominating at low excitation), (ii) electron–ion scattering (i.e. on ions formed after electronic excitation), (iii) electron–neutral-atom scattering (as the solid bonds vanish) and (iv) electron–electron scattering.

The electron–phonon scattering rate for degenerate matter can be calculated from quite general arguments, as done originally for astrophysical objects by [102]. For cold solid matter, Eidmann *et al* show that the expression simplifies to [103]

$$\Gamma_{e\text{-}p} \simeq 2k_s \frac{e^2 k_B T_i}{4\pi\epsilon_0\hbar^2 v_F}, \qquad (16)$$

where T_i is the temperature of the lattice, $v_F = \hbar(3\pi^2 n_e)^{1/3}/m_0$ is the Fermi velocity of the electrons and k_s is a numerical constant used to match the collision rate to measured values for the cold sample. This expression shows that under the assumption that the lattice remains cold for the duration of the laser pulse, the electron–phonon coupling is constant as a function of electron energy (but depends on the electron density through v_F). More advanced calculations provide the electron–phonon momentum scattering rate as a function of the electron kinetic energy. For instance for SiO_2, the scattering rate increases from $\sim 10^{14}$ to $\sim 10^{16}\,s^{-1}$ as the electron kinetic energy increases from 0 to 6 eV but then remains quite constant at this value over the calculated energy range, i.e. from 6 to 30 eV [104, 105].

Note that as the electronic excitation increases, the phonon spectrum will change, as the restoring forces of the lattice are gradually weakened. The phonon energy of the scattered phonons thus gradually decreases, and eventually the electron–phonon scattering vanishes completely. The description thus changes gradually from that of a solid to that of a warm dense matter, which is hard to describe theoretically. It is most frequently described as a weakly ionized plasma (at solid density), and the description of scattering can then be based on different results from plasma physics (for an overview, see [106]).

For the electron–ion collision rate, several groups have used the Spitzer expression (see section 2.4), which is derived under the assumption of a Maxwell–Boltzmann distribution of the electron velocity [107, 108],

$$\Gamma_{e\text{-}i} = \frac{1}{3(2\pi)^{3/2}} \frac{Z\omega_p^4}{n_e v_e^3} \ln\Lambda, \qquad (17)$$

where Z is the charge state of the ions and $v_e = \sqrt{3k_B T_e/m_0}$ is the thermal velocity of the electrons. The factor $\ln\Lambda$ is denoted as the Coulomb logarithm. It originates from the cross section for Coulomb scattering and can be evaluated by $\ln\Lambda = 1/2\ln(1 + (b_{max}/b_{min})^2)$, where the b's are maximum and minimum impact parameters; see, e.g., [107, 108]. The expression can be generalized to include the degeneracy effects, which become important at lower kinetic energies of the electrons; for a detailed discussion, see [107].

At intermediate excitations, before all atoms in the solid are ionized, one should also consider the effect of scattering of the electrons on remaining neutral atoms after the solid bonds have weakened. Since the cross section, density and mean-free-path are related by $\sigma n_0\ell = 1$, the rate for electron–neutral scattering estimated by v_e/ℓ becomes

$$\Gamma_{e\text{-}n} = \sigma n_0\sqrt{3k_B T_e/m_0}, \qquad (18)$$

where the neutral density, n_0, is related to the original atom density, n_a, the time-dependent electron density and the charge-state of the ions as $n_0 = n_a - n_e/Z$, since n_e/Z is the number of ions. The cross section is slowly varying over the relevant energy range and roughly given by the size of the atom; a typical value is $\sigma_0 \simeq 5 \times 10^{-15}\,cm^2$ [106].

The effect of electron–electron scattering has been discussed by a few groups [91, 109]. Christensen and Balling [91] treat the electrons semiclassically by employing a classical scattering rate from kinetic gas theory on electrons with a 'radius' given by the Debye screening length [96]. The resulting expression becomes

$$\Gamma_{e\text{-}e} = \frac{4\pi\epsilon_0}{e^2}\sqrt{\frac{6}{m_0}}(k_B T_e)^{3/2}, \qquad (19)$$

which is independent of the electron density, because the square of the Debye radius is inversely proportional to density. Chimier *et al* [109] use an expression valid for a degenerate electron gas, giving an expression $\sim T_e^2/E_F$.

For both the electron–phonon, the electron–ion and the electron–neutral-atom scattering rates, one can put an upper limit on the scattering rate based on the known lattice spacing of the material: the collision rate can never exceed v_e/a, where a is the lattice spacing (or more generally the effective radius of the atoms of density n_a; see, e.g., [103]). We thus have as an upper limit

$$\Gamma_{max} = \sqrt{\frac{3k_B T_e}{m_0}}\left(\frac{4\pi}{3}n_a\right)^{1/3}, \qquad (20)$$

The electron–electron scattering rates can be slightly larger than this, since these collisions are limited by the electron density and thus will not exceed $Z\Gamma_{max}$.

Table 1. An overview of modeling approaches to short-pulse excitation and ablation. The abbreviations used are the following. (i) The electronic excitation models: 'SRE' = single rate equation; 'T_e' = include description of electron temperature; 'TTM' = two-temperature model; 'MRE' = multiple rate equation. (ii) The strong-field excitation: 'MPE' = multi-photon excitation; 'Keldysh' = combined MPE and tunneling. (iii) The optical model: 'Drude' = dielectric function by equation (13) or (15). (iv) The electron scattering rate: 'e–p' = electron–phonon; 'e–i' = electron–ion; 'e–n' = electron–neutral; 'e–e' = electron–electron.

Reference	Excitation model	Optical model	Electron-scattering rate	Ablation criterion
Stuart 1996 [76]	SRE MPE	Drude	e–p: From [104]	Charge density − critical
Guizard 2002 [97]	SRE MPE	Drude	e–p	Energy density + redistribution
Feit 2004 [101]	SRE MPE	Drude	Constant	Charge density − critical
Jiang 2005 [119, 110]	SRE T_e MPE	WKB absorption Drude	e–p: Cold solid matter e–i: Spitzer	Charge density − critical
Peñano 2005 [113]	SRE T_e MPE	Maxwell Drude	e–n: $\sqrt{T}$ e–i: Spitzer	Energy density *versus* charge density
Petrov 2008 [114]	SRE T_e Keldysh + forest fire	Maxwell Drude	e–p: From [105] e–i: Spitzer	Energy density *versus* charge density
Jiang 2008 [115]	SRE TTM MPE	WKB absorption Drude	e–p: Cold solid matter e–i: Spitzer	Charge density *versus* lattice temperature
Christensen 2009 [91]	MRE Keldysh	Cumulated absorption Drude	e–p: Constant e–e: Semiclassical	Charge density–fixed
Bourgeade 2010 [121]	MRE MPE	Maxwell Drude	e–n: $\sqrt{T}$ e–i: Spitzer	—
Chimier 2011 [109]	SRE TTM Keldysh	Exponential Drude	e–p: Cold solid matter e–n: $\sqrt{T}$ e–i: Spitzer e–e: Fermi gas Maximum rate inferred	Lattice temperature

In general, it is hard to form expressions that remain valid over a large electron-energy and density range. Many authors have thus used interpolations between different approximations. This was first suggested by Eidmann *et al* for metals [103] and later used for dielectrics by, e.g., Chimier *et al* [109].

2.3.4. From electronic excitation to material response: ablation mechanisms. Once a proper description of the material excitation has been established, one must devise methods for associating an excitation level with a given material alteration. Two fundamentally different criteria have been applied: one is based on the electron density while the other uses the (closely related) energy density. The ablation criteria used in several papers are listed in table 1.

Many authors attempt to associate a certain density of excited electrons with a specific material response [76, 91, 101, 110]. The rationale is as follows: the electrons in the valence band form the bonding orbitals of the solid, so when a certain fraction has been excited, the material becomes unstable and fragmentation (leading to ablation) sets in. In many papers, the density used for this criterion is taken to be the critical plasma density, i.e. the electron density where the plasma frequency, equation (14), equals the frequency of the laser [76, 101, 110]. The argument is that when this density is reached, the absorption will increase so much that a small amount of additional pulse energy will be enough to trigger the material removal (see, e.g., [111]). While it is clear that at the critical plasma density, the optical properties of the material will change, other authors have argued that the density for ablation to set in should be a material parameter and thus not depend on the wavelength of the light (see, e.g., [91]).

To the extent that a thermal description can account for the material response, it appears more intuitive to use the energy density for predicting the material response. This may also be a more robust criterion, since according to [97, 112], the charge density at threshold may in fact depend on the pulse duration. The total energy density can be calculated as the sum of that belonging to electrons and lattice (as described, e.g., in [65, 113, 114]) or when properly accounting for the electron–lattice coupling, the lattice temperature can be used to predict the material response [109, 115, 116]. The electron–lattice coupling has been treated in a two-temperature description using different approximations to electron–ion coupling factors, which are not very well fixed by the experimental data [115], but provide an electron–lattice equilibration time of a few picoseconds [109].

Some authors have shown that the predictions of threshold from the two ablation criteria are in fact quite similar [116], while others note that although the behavior of, e.g., the threshold fluence versus pulse duration is qualitatively similar, a systematically higher threshold fluence is predicted when applying the thermal criterion than when applying the density criterion [113, 114].

The specific mechanisms leading to material ejection will be discussed in detail in section 3. Here let us just point to the fact that there appears to be two competing mechanisms: a thermal mechanism, which will be discussed in greater detail in section 3.1, and an electrostatic mechanism, often denoted as Coulomb explosion; see section 3.4. The driving mechanism of the latter is the separation of charges: the strong laser intensity induces (multi-photon) photoemission, and due to the low conductivity of the dielectric material, this can lead to the build-up of a local positive charge density. If the electrostatic
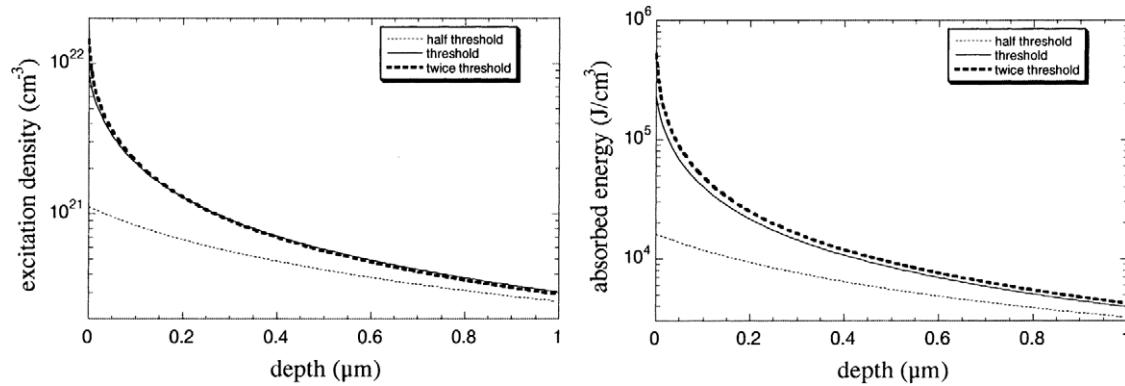
Figure 8. The carrier excitation density as a function of depth in Al_2O_3 for three different intensities; the threshold is at 73 TW cm^{-2} with a pulse duration of 58 fs. The right panel shows the corresponding energy densities. Reproduced with permission from Guizard *et al* [97]. Copyright (2002), reprinted with permission from Elsevier.

repulsion exceeds the binding forces, the ions are ejected by Coulomb explosion. In this case, the ablated particles exhibit a non-thermal kinetic-energy distribution, as can be observed by time-of-flight mass spectrometry [117, 118], which will be discussed in greater detail in section 3.4.

The existence of thermal effects at high fluences has been demonstrated by a TEM investigation of diamond [44]. The authors show that after single-pulse irradiation, a thin surface layer ($\sim$50 nm) exhibits diffuse diffraction rings, indicating the formation of a layer of nanocrystalline diamond and possibly amorphous carbon. For potassium–magnesium-silicate glass, a recent x-ray absorption near-edge spectroscopy (XANES) study of laser-ablated regions has shown that above the ablation threshold, the magnesium K-edge undergoes a shift to lower energies, which is attributed to a reduced Mg–O bond length associated with a change in the average coordination number of the Mg ion from mainly sixfold coordinated to partly fourfold due to the irradiation [58]. This decrease in bond length, associated with densification, is similar to that observed by Raman spectroscopy of bulk modifications of BK7 when irradiated with MHz-repetition-rate, low-pulse-energy ultrashort pulses [60]. On the other hand, the effect of higher-energy kHz-rep-rate irradiation appears to be the formation of non-bridging oxygen atoms associated with defect formation [60].

2.4. Modeling ablation dynamics: combining material excitation and propagation

While the previous section gave an overview of the ingredients of a description of highly excited dielectric materials, we will here describe different approaches to modeling the entire ablation process. Referring again to figure 2, such descriptions need to include both material excitation and light propagation. The benefit is that the models potentially allow a prediction of both ablation thresholds and ablation rates, and a comparison of the results of a calculation with measurements of the ablation depth as a function of the applied fluence puts quite strict boundaries on the model. An overview of different approaches to such modeling is provided in table 1.

At first sight, it may seem that the description of the threshold is less sensitive to propagation, since it will

effectively be determined by the threshold for breakdown at the surface. However, as will soon become clear, already in the outer layer, the mechanisms are strongly influenced by the time-dependent optical properties of the material.

2.4.1. Single-rate-equation and Drude models. The first example of a calculation, which combined material excitation (in a single-rate-equation description) and propagation using the Drude expression equation (13) for the dielectric function, was presented in Stuart *et al* [76]. In this paper, the absorption is set equal to the energy gain of the electrons due to avalanche excitation. The authors demonstrate how the electronic excitation leads to a high reflectivity of the rear end of pulses, and they also show that, at high fluences, the energy is primarily deposited over a thin 'skin depth'.

The Drude model was also used to describe the time-resolved optical measurements by Quere *et al* [98]. By combining a rate equation describing multi-photon and avalanche excitation with a propagation equation accounting for the energy absorbed by multi-photon absorption and in the free-electron plasma, the authors produced excitation-*versus*-depth curves through the excited material. The authors show that their experimental data can only be reproduced by assuming negligible influence of avalanche.

In a later paper by the same group [97], the authors extend this method to the higher excitation levels needed to describe ablation. In order to account for the potentially high excitation levels, they use the Clausius–Mossotti correction to the Drude model, equation (15) in section 2.3.3. They provide a comparison between the carrier excitation level and the energy density for Al_2O_3; see figure 8. As also noted by the authors, the variation of the two quantities as a function of depth are qualitatively very similar in the presented model.

With these results, Guizard *et al* [97] were for the first time able to predict ablation depths from the excitation levels. Based on the previously reported observation that the density at threshold depends on the pulse duration [112], these authors applied an ablation criterion based on the total absorbed energy density at the end of the pulse. The appropriate energy was obtained by comparison with the experimental data, and the authors point out that the threshold is only weakly dependent
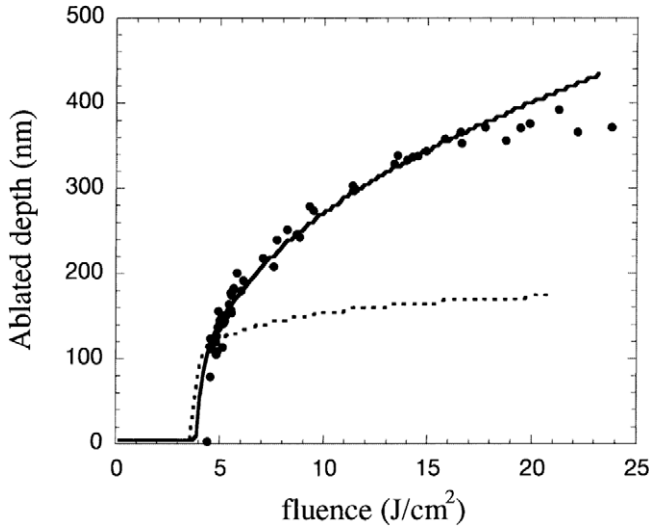
Figure 9. A comparison between the calculated (lines) and measured (points) crater depths in Al$_2$O$_3$. The solid line and dashed lines correspond to two different ablation criteria, as described in the text. Reproduced with permission from Guizard *et al* [97]. Copyright (2002) reprinted with permission from Elsevier.

Figure 10. A comparison between the crater shapes derived from an electron density and a lattice temperature criterion. Laser parameters are 50 fs pulses at 780 nm and a fluence of 5 J cm^{-2}. Reproduced with permission from Jiang *et al* [115], and American Institute of Physics, Copyright (2008).

on the choice for this energy density, while it has, however, strong impact on the calculated ablation depths.

Figure 9 shows the comparison between the results of the calculation and the experimental depths obtained by applying an interferometric technique. The dotted line is the result directly derived from the simulation, while the solid line represents a modification of the calculated energy densities *versus* depth so that the excess energy accumulated near the surface propagates into the sample, an approach which the authors denote as an entirely 'mathematical result', which may not be justified by physical arguments.

As previously assumed in Stuart *et al* [76], Feit *et al* [101] argue that the energy absorbed by the 'free' electrons will eventually lead to subsequent excitation of secondary electrons and thus propose to set the free-electron absorption (quantified by the complex refractive index) equal to the avalanche term of the rate equation. The electron absorption is described with a Drude-model dielectric function. Under these assumptions, the authors calculate the transient changes in optical properties of water including the reflection from the front surface as well as absorption and transmission through 25 μm. As mentioned in the paper, water is here regarded as an amorphous dielectric with a band-gap energy of 6.5 eV. The authors use a fixed collision frequency in the Drude expression, which is adjusted to 3×10^{14} s^{-1} in order to provide agreement with experimental data.

2.4.2. Single-rate-equation, electron temperature and Drude models. Jiang and co-workers combine the rate-equation description of electronic excitation with a free-electron-gas description of the electrons in the conduction band [110, 119, 120]. The absorption in a Drude model is coupled with electron heating described by a temperature of the electrons in the conduction band. The free-electron relaxation rate used in the Drude expression is taken as a sum of two terms: an electron–phonon scattering rate as given by equation (16)
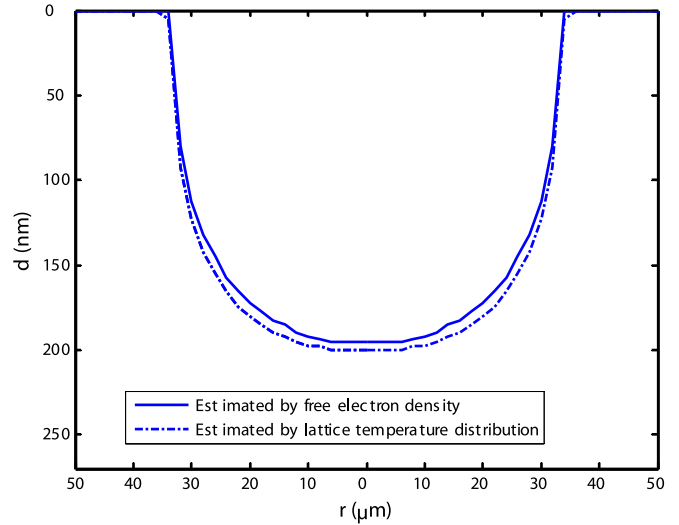
(taken from [103]) and an electron–ion scattering rate given by a Spitzer-type expression, see equation (17), corrected for degeneracy effects at low excitation levels as discussed in [107], see also section 2.3.3. The intensity distribution is obtained iteratively from the expression [110]

$$
\begin{aligned}
I(t, r, z) = {} & \frac{2F}{\sqrt{\pi/\ln 2\tau}} \left(1 - R(t, r)\right) \\
& \times \exp\Bigg(-\left(\frac{r}{r_0}\right)^2 - 4\ln 2 \left(\frac{t}{\tau}\right)^2 \\
& \quad - \int_0^z \alpha(t, r, z')\, \mathrm{d}z' \Bigg),
\end{aligned}
\tag{21}
$$

where the absorption coefficient of the material, α, is derived from the optical parameters of the Drude plasma using $\alpha = 2\kappa\omega/c$ (as discussed in section 2.3.3). Note that this equation is a Wentzel–Kramers–Brillouin (WKB)-type expression, which is derived under the assumption that the optical parameters of the material do not change significantly over one optical wavelength (see [108]).

With their model, the authors of [110, 119, 120] can calculate both the density and the temperature of the electrons as a function of time and space, and they use this to predict crater profiles under the assumption that material is ablated if the electron density at the end of irradiation is greater than the critical density.

In a later paper by the same group [115], the model is extended to a two-temperature description of the electrons and lattice, and the crater profiles obtained from the free-electron density are found to be very similar to those obtained using a threshold for ablation based on the lattice temperature. This comparison is shown in figure 10.

2.4.3. Models with emphasis on electromagnetic propagation. Some groups have put strong emphasis on a proper treatment of the electromagnetic theory, typically solving
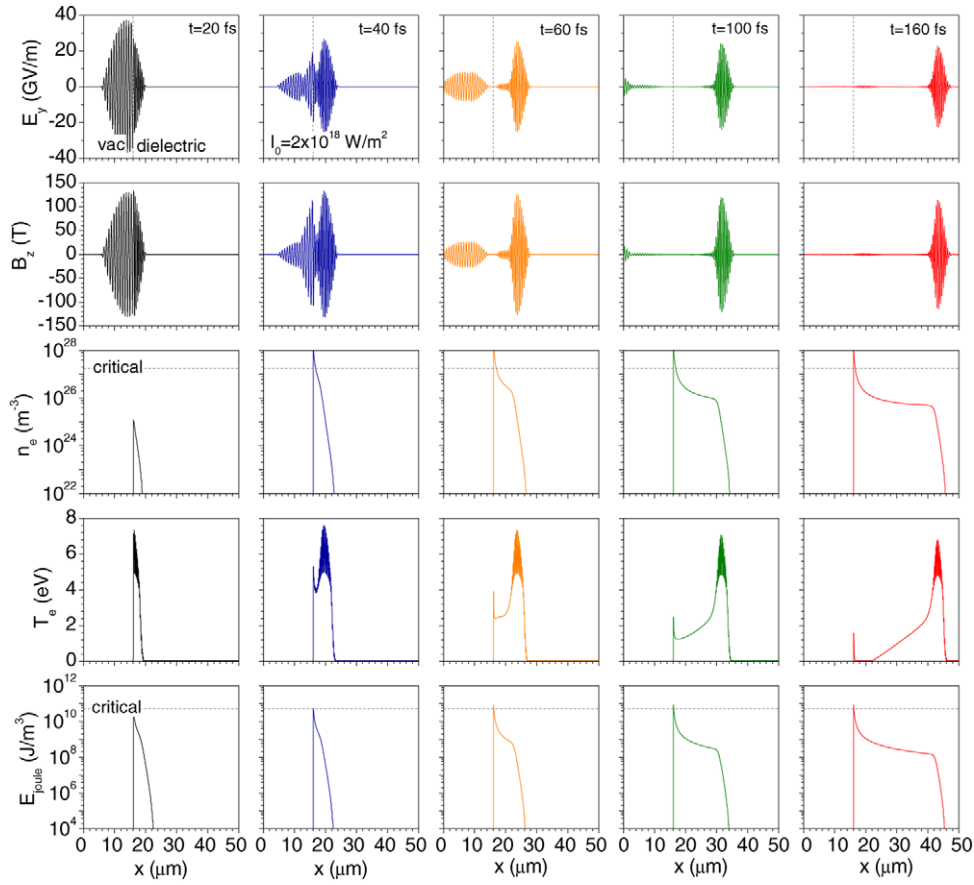
Figure 11. Snapshots of the laser electric and magnetic fields of an ultrashort pulse impinging on an SiO_2 sample, shown together with the electron density and temperature as well as the absorbed energy density. The laser has a wavelength of 800 nm, pulse duration (FWHM) of 26.7 fs and peak intensity 2×10^{14} W cm^{-2}. Reproduced with permission from Petrov and Davis [114].

Maxwell's equation numerically in the excited medium. For example Peñano *et al* [113] investigated the one-dimensional propagation of a 100 fs pulse in a material, where the dielectric function was described by a Drude model with a free-electron scattering rate being the sum of an electron–neutral (see equation (18)) and an electron–ion scattering rate (equation (17)). The electronic excitation was described by a rate equation for the density with the strong-field excitation rate described by a six-photon-excitation cross section in combination with an equation for the electron temperature. The important conclusion of the paper is that a significant transmission of the pulse is seen even at intensities, where the excitation is so large that the plasma density exceeds the critical value, the reason being that this only happens toward the trailing end of the pulse.

In the work by Petrov and Davis [114], the work of Peñano *et al* [113] is extended in two ways: first, the authors use more accurate strong-field excitation rates and, second, they introduce the effect of holes as seeds for enhanced ionization in the 'forest fire' model of Gaier *et al* [70]. Figure 11 shows an example of the result from the calculation. The incident pulse interacts with the plasma it generates, and the propagation, excitation and heating must be treated self-consistently. Based on their calculations, Petrov *et al* [114] conclude that the absorption in the electron plasma is the main mechanism for energy transfer from the light field to the solid with SFI playing a small role energetically, but an important role for seeding

the process. Accordingly, they claim that—for SiO_2—the collisional excitation is dominating over direct strong-field excitation for the intensities of relevance for ablation; see also section 2.5.

Bourgeade *et al* [121] compare the approach of [113] to results obtained by applying a MRE description of the electrons in place of the temperature description. The authors find somewhat different optical response and attribute this to the possible failure of assigning a temperature to the excited electrons. A comparison with the experimental results from time-resolved interferometry [81] lends support to the results from the MRE model.

Although strictly speaking outside the scope of this review, let us just mention that focussing in the bulk of a dielectric has been treated by solving Maxwell propagation in three dimensions in combination with applying the MRE model for the electronic excitation [122].

2.4.4. Other approaches to propagation. Christensen and Balling [91] describe an approach to combining the MRE with propagation, which does not require solving the Maxwell equations. Instead these authors assume a local absorption coefficient described by $\alpha = 2\kappa\omega/c$ and calculate the energy density at a given depth by accounting for the accumulated loss down to that depth (similar to the WKB approximation, equation (21)). The absorption coefficient is
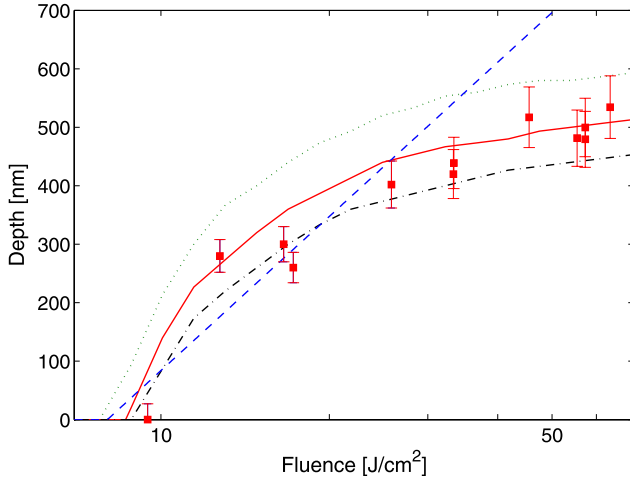
Figure 12. A comparison between hole depths measured by AFM (red squares) and a calculation using the MRE model in combination with propagation. The solid red line corresponds to an ablation criterion of 10%, while the green dotted and the black dashed–dotted lines correspond to 8% and 12%, respectively. The blue dashed line represents a logarithmic fit to data near the threshold. Reproduced with permission from Christensen *et al* [92], and with kind permission from Springer Science and Business Media.

Figure 13. The dependence of the damage fluence versus pulse duration; squares are experimental values. The red solid curve (1) represents Keldysh strong-field excitation with collisional excitation, while the blue dashed–dotted curve (2) is without collisional excitation. The similar results with multi-photon excitation are shown by the green dashed (3—no collisional excitation) and purple dotted (4—with collisional excitation). Reproduced with permission from Chimier *et al* [109]. Copyright (2011) by the American Physical Society.

used to calculate the cross section for single-photon excitation in the MRE model, equation (12), providing thus a self-consistent solution to the coupled excitation–propagation problem. With this approach the authors are able to carry out parametric investigations over a broad parameter space for the material band gap, pulse durations, and wavelength. The electron-scattering rate is taken as a sum of a constant electron–phonon scattering rate and an electron–electron scattering rate from semiclassical arguments, equation (19). In a later investigation, the model is compared with single-shot experiments on sapphire. As seen in figure 12, the agreement is reasonable if ablation is assumed to occur when the electron density exceeds 10% [92].

Although derived from quite simplifying assumptions, Puerto *et al* [53] obtain very good agreement between their measurements and an analytical expression for the maximum crater depth

$$d_{\max} = B_m - \frac{A_m}{F_0^{m-1}}, \qquad (22)$$

when a five-photon process is assumed (i.e. $m = 5$) and the constants $B_m = 1/((m-1)\alpha_m F_{th}^{m-1})$ and $A_m = 1/((m-1)\alpha_m)$ are used as fitting parameters for determining F_{th} and α_m, the m-photon absorption coefficient.

In a recent paper, Chimier *et al* [109] describe the results obtained from a single rate equation description combined with a two-temperature model (as in Jian *et al* [115]). This paper uses an elaborate description of the electron-scattering rates, which are taken as an interpolation between (i) at low electron temperatures the sum of electron–phonon scattering (cold solid matter, equation (16)) and electron–electron scattering (degenerate electron gas $\sim T_e^2/E_F$); (ii) at high temperatures the sum of electron–neutral (equation (18)) and electron–ion (Spitzer, equation (17)); (iii) an overall maximum possible scattering rate similar to equation (20). Since the paper focuses
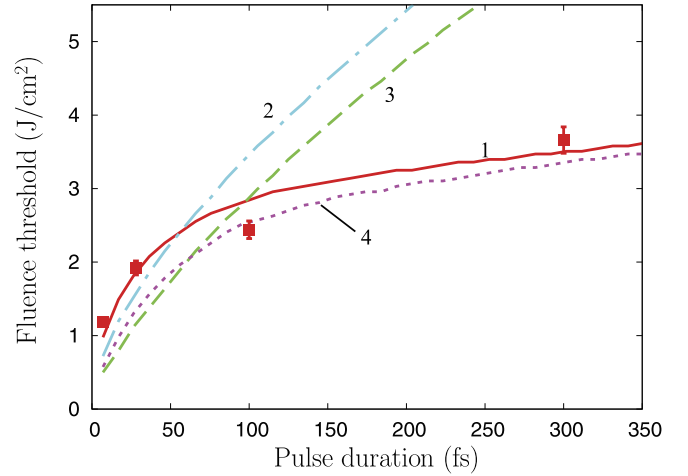
on surface phenomena, propagation is included somewhat indirectly by assuming an exponential energy distribution but with a time-dependent absorption length. The authors use the lattice temperature to determine the threshold for both damage (taken as melting) and ablation (cohesion temperature) and get good agreement with their measurements at a range of pulse durations. The authors are able to compare the results from calculations in different approximations; see figure 13. The calculation shows that the results obtained with a Keldysh description of SFI and inclusion of collisional excitation give the best agreement with the experimental results.

2.5. Relative significance of collisional excitation: avalanche or no avalanche?

As mentioned already on several occasions in this paper, the relative importance of the avalanche excitation is a topic of ongoing discussion. It is clear that the answer must depend strongly on the pulse duration, since at the shortest pulse durations there is no time for the electrons in the conduction band to acquire enough energy that the collisional excitation becomes energetically possible; see figure 2. However, at increasing pulse durations the current literature reports conflicting results about the importance of avalanche.

When evaluating the reported comparisons between model calculations and experiments, it should be noted that the apparent relative importance of the avalanche term is critically dependent on other model parameters. For instance, as mentioned previously, early models used the perturbative multi-photon excitation (i.e. power-law) expression for the excitation rate, which overestimates the rates significantly at medium and high intensities; see figure 3. This will reduce the apparent importance of avalanche. On the other hand, in some of the early studies, this effect may have been canceled
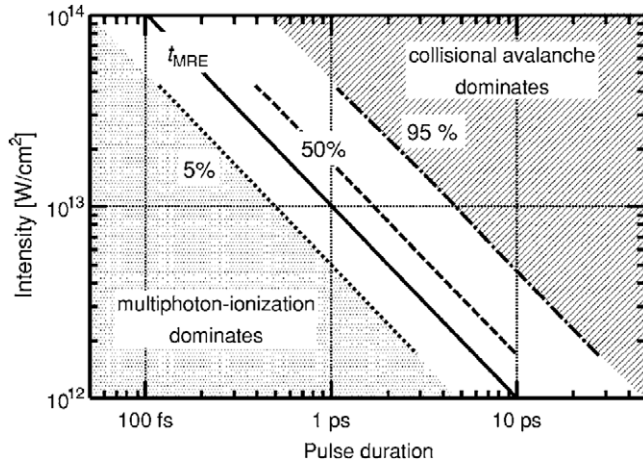
Figure 14. The percentage of impact-ionized electrons as a function of laser pulse duration and intensity as calculated from the MRE model, equation (12). The transition time t_{MRE} indicates the transition between the photo-ionization-dominated and avalanche-dominated regimes. A photon energy of 2.48 eV and a band gap of 9 eV have been applied. Reproduced with permission from Rethfeld [90]. Copyright (2006) by the American Physical Society.

by applying a comparison with experimental data obtained in the multi-shot regime, which will exhibit lower thresholds (section 2.7). With these precautions in mind, the conclusion of the early investigations is that for a 100 fs pulse, the avalanche becomes the dominating excitation mechanism [75, 76]; see figures 4 and 5.

Based on the MRE model calculations, Rethfeld [90] offers an overview of the relative importance of impact ionization for a range of intensities and pulse durations; see figure 14. The author defines a transition time, t_{MRE}, between the two regimes, which is inversely proportional to the applied intensity, $t_{MRE} \approx 100$ fs $\cdot (10^{14}$ W cm$^{-2})/I$ for the specific photon energy and band gap used to calculate figure 14.

The significance of the avalanche process has been extensively studied in the optical measurements of dielectric excitation. The first investigations were consistent with a model including only multi-photon excitation (i.e. no avalanche) [79]. This is further justified by measurements of the phase shift (assumed proportional to the final excitation level) being proportional to I^N, with N being the order for the multi-photon process [55]. It should be noted that these measurements are limited to intensity regimes, where the sample remains fairly transparent, which, e.g., for 60 fs, 800 nm pulses on SiO$_2$ is somewhat below 10^{14} W cm^{-2}. It is therefore not necessarily in conflict with the predictions by Rethfeld [90] (although it should be emphasized that the photon energy is lower in the experiment than in the calculation behind figure 14). In a more recent investigation, Guizard and et al have undertaken double-pulse experiments to gain more insight into the avalanche mechanisms [123]. The authors use a 50 fs pulse at 400 nm to excite a large density of carriers. A subsequent 800 nm pulse is then stretched in time to 10 ps (corresponding to 4×10^{12} W cm^{-2}) so that the strong-field excitation rate is small, but it should still heat any electrons

remaining in the conduction band. Surprisingly, the 800 nm pulse does not increase the observed phase shift (i.e. the excitation); rather the combined effect of the two pulses is to *reduce* the decay time of the observed phase shift.

In contrast to this observation, recent experiments by Sarpe *et al* using also time-resolved spectral interferometry to investigate the excitation of thin water jets showed that for asymmetrically shaped pulses, the excitation was much stronger when the intense part of the pulse arrives first [86]. By first considering the excitation by bandwidth-limited pulses of 35 fs duration and assuming negligible avalanche for these pulses, the authors of [86] extract both the five-photon excitation cross section and the electron-collision rate for water. Using these data for the asymmetric-pulse excitation, the authors then obtain a value for the avalanche coefficient. The simulations show that in the case, where the intense part of the pulse arrives first (peak intensity $\sim 10^{12}$ W cm^{-2}), the avalanche accounts for more than 85% of the final free-electron density.

The time-resolved reflectivity measurements by Jia *et al* [124] exhibit a strong increase in reflectivity during the last half of the exciting pulse, which leads the authors to conclude that impact ionization plays an important role in the generation of conduction-band electrons. The same is seen in simulations of the time-dependent reflectivity by Wædegaard *et al* [94], although these simulations are only compared with the overall reflectivity of the pulse.

In [114], Petrov and Davis discuss avalanche in the forest-fire model. When including the effect of holes on the strong-field excitation, the authors conclude that the limit between strong-field dominated and collision-dominated regions is essentially an energy criterion: strong-field excitation dominates, when the fluence is below 0.4 J cm^{-2}; otherwise collisional excitation dominates. Essentially this means that at fluences of relevance for laser ablation collisional excitation is always the main excitation mechanism. Note that the characteristic time scale t_{MRE} described above also corresponds to a fluence-dependent criterion, but from the MRE model by Rethfeld [90], this fluence is 10 J cm^{-2}, i.e. more than an order of magnitude larger than suggested by Petrov and Davis [114].

The recent results from a kinetic calculation by Schneblanov *et al* predict quite low kinetic energies of the excited electrons, which leads the authors to the conclusion that for wide-band-gap dielectrics, such as SiO$_2$, at pulse durations below 200 fs and laser intensities $\sim 10^{14}$ W cm^{-2}, the influence of impact ionization mechanism is negligibly small [74].

Conversely, the avalanche process is included in the modeling of both Christensen and Balling [91] and Chimier *et al* [109]. According to [91], a large fraction of the light energy is absorbed in the conduction-band electrons leading to significant avalanche. Chimier *et al* [109] compare results obtained from calculations with and without the avalanche term, and only the former agrees with the experimental data.

2.6. Recent experimental developments

As apparent from the previous sections, many experimental investigations have focused on measuring the damage or

ablation threshold and its dependence on controllable parameters. Much information has been obtained by measuring F_{th} versus the pulse duration [25, 63, 75–78, 109, 125–132]. In Louzon *et al* [126], a difference in the observed threshold between up- and down-chirped pulses is demonstrated. Englert *et al* [133, 134] apply more complex control of the electric field in the laser pulses and demonstrate markedly different hole geometries—in some cases holes much smaller than the diffraction limit—when different pulse shapes are applied. In [132], it is reported how changing the pulse duration can to a high extent control the hole depth, while the hole diameters are mainly controlled by the applied fluence.

In addition to variations in the pulse duration, other parametric investigations of the threshold fluence have also been reported. A few groups have investigated the threshold as a function of the laser wavelength. For relatively low band gap, one experiment demonstrates significant drops in the threshold when the photon energy changes over thresholds corresponding to the opening of a new—lower-order—channel [135]. For higher-band-gap materials, the changes were mainly attributed to changes in the optical properties of the laser-generated plasma [124].

The threshold fluence as a function of the material band-gap energy has been investigated by a few groups. In Mero *et al* [127], the damage fluence was observed to increase linearly with the band-gap energy. The same authors also investigated the scaling with pulse duration for a range of materials and found a power-law dependence with an exponent, which was roughly the same, 0.30 ± 0.03, for all materials. In contrast to the linear dependence in [127], Zavestovskaya *et al* [136] observe a power-law dependence of F_{th} versus the band gap with an exponent of 3.1.

In addition to these valuable parametric investigations of the threshold fluence, detailed information can also be obtained by measuring the ablation depth as a function of fluence; see section 2.4. However, much work remains before such investigations have been undertaken for a broad range of laser-pulse and material parameters under single-shot-irradiation conditions.

The conclusions from optical measurements by time-resolved spectral interferometry have been reviewed by Mao *et al* [55]. Optical measurements at excitation levels corresponding to ablation have been carried out by several groups [48, 53, 56, 57, 94, 124, 137–139]. At these excitation levels, the transmission becomes very low for interferometric measurements of the volume, so many investigations have deduced information from time-resolved (pump–probe or double-pulse reflectivity) experiments, in some cases with two different colors. The strong increase in reflectivity during the pulse has led to the concept of a 'plasma mirror' [137, 138]. Several authors have demonstrated that the reflectivity increases during the pulse, and even after the pulse is over [48, 53, 124, 139]. A few investigations of the reflectivity of the exciting pulse as a function of intensity have shown that following the initial increase, the reflectivity does, in fact, drop again. In Ziener *et al* [137] and Chowdhury *et al* [139] this is attributed to the onset of scattering from the generated plasma,

while Wædegaard *et al* [94] argue that the drop happens due to the optical properties of the highly excited plasma.

2.7. Single- versus multi-shot irradiation: incubation effects

It has been observed by a large number of investigations that the material response depends critically on the previous irradiation history of a dielectric sample. Quite generally, and as pointed out already in the first reports by Ashkenasi *et al* [140] and Lenzner *et al* [141], the threshold for damage or ablation decreases after repeated irradiation, and the decrease is often accompanied by a drop in the apparent penetration depth [141]. These observations may be explained by the accumulation of defects (e.g. F-center formation [142]), which gradually changes the optical properties and therefore increases the absorption. The formation of color centers has been demonstrated experimentally through their spectroscopic features by Hertwig *et al* [143].

Two different models have been introduced to quantify the changes in the threshold for increasing number of pulses: one assumes an exponentially decreasing threshold [140, 142], while the other uses the power-law expression for the decrease [144], which was originally suggested for metals [145].

Note that due to the statistical nature of damage formation, the damage threshold for a given laser fluence and a given number of pulses could in fact depend on the laser spot size, since a large spot size samples a larger area and therefore has a larger probability of localizing a sample location with a low (local) threshold, which will trigger damage. Nonetheless, this effect was not observed in the first investigations on SiO_2 [140], but it was, however, seen in a later investigation on BBS glass [146].

In a recent series of investigations by the Rudolph group, the incubation effects have been characterized by investigating the changes in material damage threshold both as a function of the number of pulses [147] and as a function of pulse separation for two-pulse irradiation [148] and comparing the observations with detailed modeling of the material excitation including defect states located inside the band gap with a finite lifetime.

In addition to the incubational changes in the optical properties, repeated irradiation may also gradually change the surface morphology. Typically, some kind of laser-induced periodic surface structures (often denoted as 'ripples') are formed. A detailed discussion about the origin and characteristics of these surface structures is beyond the scope of this report; for a recent review see Bonse *et al* [149]. In the present context, the important feature of the surface morphology is that it will also change the ablation threshold, presumably both due to changes in the laser energy coupling efficiency through, e.g. changes in reflectivity and local-field-enhancement effects, and due to changes in the thermal properties of the material induced by the associated high defect density.

3. Ejection and plume formation of heated material induced by femtosecond-laser impact

As discussed in section 2.3.4, in the thermal description of ablation, the electronic system and the lattice equilibrate a
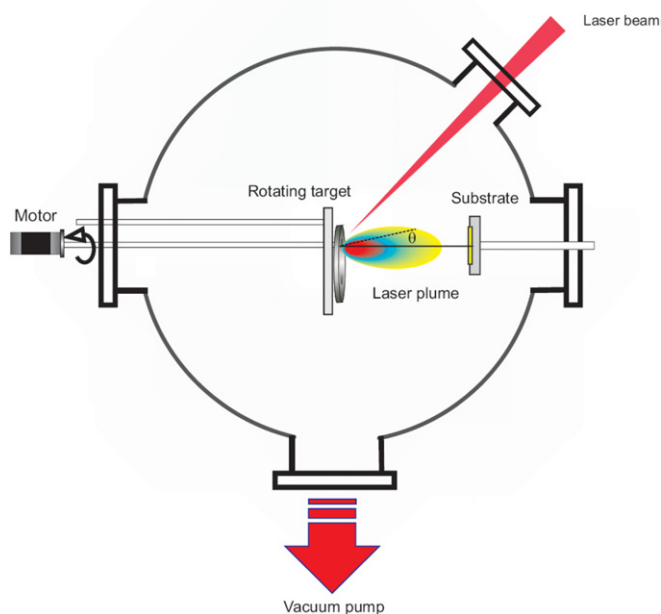
Figure 15. PLD system with target and substrate. The angle of emission from the ablation process, θ, is indicated as well.

few picoseconds after the termination of the femtosecond pulse. At this time the material starts the expansion and a lot of phenomena may occur such as evaporation, plume formation, homogeneous nucleation and decomposition, photomechanical ejection and spallation. Except for spallation, all these processes lead to ejection of material, which subsequently can be collected as a thin film on an appropriate substrate (figure 15). This film-production process PLD, which also comprises film production by nanosecond-lasers, has achieved a world-wide exploitation for fabrication of thin films, in particular with nanosecond-lasers for materials with a complicated stoichiometry [41, 150, 151]; see section 1.4.

However, as mentioned in the introduction, one important feature of femtosecond-laser ablation for thin film deposition differs strongly from that of nanosecond-laser ablation: the majority of particles from the ablated solid are ejected as nanoparticles [152–155]. Also the plume development has specific trends compared with nanosecond-laser ablation, and eventually the combination of the different size distribution of ablated particles and other properties of the plume leads to production of films that may exhibit other physical, e.g. structural and morphological, properties than those produced by nanosecond PLD. In the following section, we will describe the ejection and plume formation of the ablated particles prior to the arrival at the substrate.

3.1. The sudden heating of the target

The heating of material by a femtosecond laser is so fast that new thermodynamic regimes have become accessible. How violently the material is influenced by the laser impact is seen in a few snapshots from a combined Monte-Carlo and molecular-dynamics (MD) simulation of a silicon sample irradiated by a femtosecond laser in figure 16 [156]. The simulations show
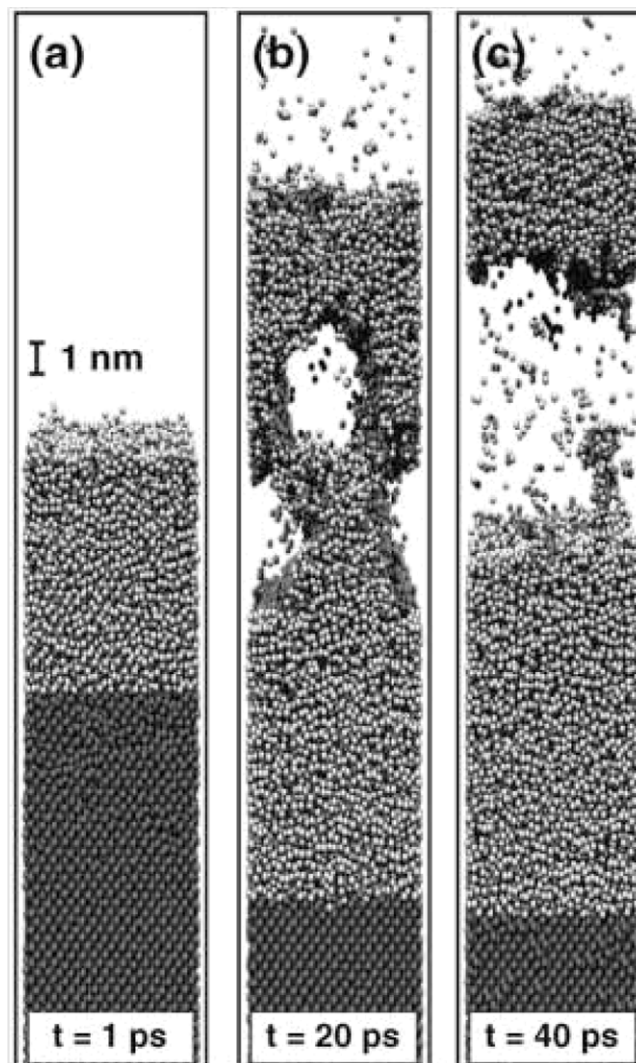
Figure 16. Snapshots of silicon expansion showing the ejection of molten material for a pulse duration of 500 fs at 266 nm at a fluence of 0.375 J cm^{-2}. Each pulse begins at $t = 0$ and is Gaussian in time, but constant in space. Dark gray: crystalline silicon; light gray: (metallic) liquid silicon [156]. Copyright (2003) by the American Physical Society.

clearly that the front of molten material propagates 20 nm into the silicon, before it stops. Close to the surface the relaxation of the pressure built up in the liquid material generates voids that nucleate and leads to ejection of nanoparticles. Actually the authors indicate that the nanoparticle in the snapshot moves with a velocity of 200 m s^{-1}, which turned out to be a typical velocity of a nanoparticle. Snapshots with similar trends have also been presented by other groups [157–163].

The attenuation of the laser beam due to the absorption processes described in section 2.3 leads to lower and lower electron-lattice equilibrium temperature with increasing depth. It was realized by several authors [152] that this temperature gradient also means that widely different mechanisms contribute to particle ejection from the same laser pulse. It is also clearly seen in figure 16 that the snapshots reflect the decreasing temperature from pure evaporation and nanocluster formation on the top of the plume to a melt zone at the deepest layer about 20 nm below the original surface.

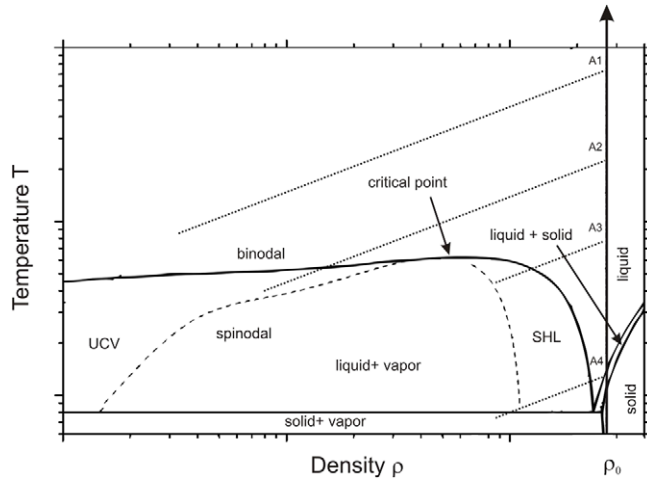**Figure 17.** Schematic phase diagram designed after [152, 155]. The trajectory of the volume element of an initial density ρ_0 is indicated as a thick, solid line along the T-axis. At different points on this trajectory, depending on the energy in the volume element (and in turn the depth in the target), e.g. denoted by A_1–A_4, the volume element starts cooling and expands along the straight dotted lines. SHL: superheated liquid; UCV: undercooled vapor.

The starting point for the discussion of the particle ejection is the thermodynamic phase diagram, usually shown as the temperature (T) dependence on the density ρ of the irradiated material in a ρ–T plot. Most authors have applied a diagram for a Lennard-Jones solid [153, 155, 164] which resembles dielectric materials with strongly localized binding. This analysis utilizes some concepts from fragmentation analysis around 1980–1990 [165–167]. As another approach some authors have modeled a metal system with free-electron dynamics and a delocalized metal binding, in all cases aluminum [152, 168, 169], while Cheng and Xu have modeled the phase diagram for nickel with a Morse potential [159]. In one case the two different approaches have been compared [161]. For our discussion, we will use a schematic ρ–T diagram (figure 17) based on [152–155]. The diagram from Lorazo *et al* [156, 170] for silicon based on an empirical interatomic potential with excited carriers that follows free-electron dynamics has a significant energy gap and resembles in this respect a dielectric material. However, silicon is a typical semiconductor, but has a metallic, liquid state, which is not very appropriate for dielectrics.

The thermodynamic system, figure 17, is characterized by the binodal (the limit at which liquid and vapor are in equilibrium). The maximum of the binodal is the well-known critical point. At each side of the binodal the thermodynamic space is metastable, either as superheated liquids to the right or as supercooled vapor to the left of the critical point. Below the binodal, the spinodal marks the limit at which the metastable matter mechanically decomposes instantaneously.

A typical trajectory for a volume element by impact of a femtosecond-laser pulse is seen in figure 17 as the solid line up to A_1–A_4 followed by adiabatic cooling to lower densities. Since no significant expansion occurs on the electron-lattice equilibrium time scale, the density ρ remains equal to the density ρ_0 of the solid. This isochoric (no change of volume)

heating is typical for femtosecond-laser impact on solids. How far up along the isochoric line a volume element reaches depends on the original depth of the volume element in the solid. For metals it has been seen in simulations that the element even induces a pressure wave with a loop at the turning point before it relaxes to lower density and temperature [169, 168]. At very high temperatures the volume element (A_1) cools along a curve driven by the pressure release via mechanical expansion toward low densities, which for metals appears to be very close to an adiabatic expansion [168, 171] as

$$T \propto \rho^{\gamma-1}, \tag{23}$$

where γ is the adiabatic constant ($\gamma = 5/3$ for an ideal atomic gas). For an ionic plume Hansen *et al* [172] found that $\gamma = 1.25$, which is also the value that Zel'dovich and Raizer recommended for a plasma [171]. For a typical nanosecond-second plume consisting of a mixture of ions and neutrals Toftmann *et al* [173] found that the value was about 1.4.

This component from A_1 represents the atomized vapor, which appears as a fast component in the plume. At lower start temperature the volume element also breaks up through pressure-induced fragmentation or critical phase separation, which occurs for trajectories arriving in the vicinity of the critical point from A_2 [159].

For the volume elements originating from deeper layers, the laser excitation brings the system to a temperature at A_3 from which the expansion is too slow to induce fragmentation, but fast enough such that no significant heat diffusion takes place. This volume element enters into the metastable zone, where homogeneous bubble formation, also called phase explosion, starts. The element splits up in a mixture of liquid and vapor, which becomes more and more pronounced, the closer the element is at the spinodal limit. This is the dominant trajectory for most of the material removal induced by a femtosecond laser not very far from the ablation threshold [169].

The behavior described above takes place when the heat diffusion is sufficiently slow. The adiabatic cooling must happen prior to a time of 10 ps, determined by a typical layer thickness (10 nm) and the speed of sound (1 km s^{-1}). At longer time, e.g. for nanosecond-laser impact, the heating is no longer isochoric, and the system will typically end up at the binodal and cool along the binodal under equilibrium conditions.

At the deepest layers, the heating brings the system up along the isochoric line to A_4. Eventually, no ablation will take place, but the material undergoes a phase change as in figure 17 or relaxes mechanically to a target surface with spallation of layers. For silicon this regime leads the system into a liquid phase (see figure 16). A thorough discussion is made in [153, 154, 162].

Upadhyay *et al* [161] show that most Lennard–Jones solids behave like a solid for laser excitations close to the ablation threshold, while metals behave like a liquid [152, 168]. For the silicon case shown in figure 16, material heated by the laser beam remaining in the solid after ablation of the upper layers melts to (metallic) liquid silicon. However, also for Lennard-Jones solids the volume passes the solid–liquid phase space and reaches the liquid space, when the initial energy
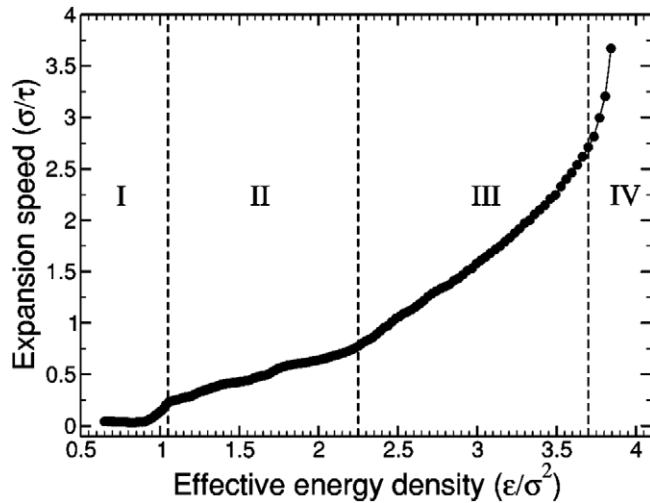
Figure 18. The expansion velocity in units of $\sigma/\tau = 1$ km s^{-1} of a Lennard-Jones material induced by a femtosecond laser of fluence $2.8F_{th}$ plotted as a function of the energy per area at a given depth in units of $\epsilon/\sigma^2 = 17.85$ eV nm^{-2} (F_{th} is the threshold fluence for ablation). The pulse width (FWHM) was 100 fs, and the attenuation depth $\alpha = 100$ nm. I is the coldest region of the laser spot volume with swelling and spallation, but no ablation, II is the volume with nanocluster formation, III and IV are top layers with fragmentation and atomization [153]. Copyright (2003) by the American Physical Society.

transfer is so high that the system starts the adiabatic cooling in the liquid phase space as shown in figure 17 [153].

An instructive plot was shown by Perez *et al*, figure 18. The expansion velocity of the material versus energy density is plotted in units of $\sigma/\tau = 1$ km s^{-1} (where σ is the Lennard–Jones length scale and 0.5τ is the pulse width of the laser at half maximum, 100 fs). These computations also show that particles originating from different regimes, i.e. different depths, have a different velocity in the plume. This is also shown in a convincing way for nickel with a comparison with experimental results by Amoruso *et al* [160].

The only existing simulation of a dielectric solid, LiF, was carried out for an ultrathin film of thickness 10 nm exposed to radiation of 89.3 eV photons [174]. The conclusion from this study is that the sequence of events leading to ablation seems to be similar to what happens in other materials. With increasing fluence the crystal is heated, then melts, then temporarily forms voids, until it finally ablates.

3.2. Nanoclusters in the plume

A consistent picture of the production of nanoclusters from metals as well as semiconductors during femtosecond-laser ablation emerged around 2004 [152, 175–177]. Also nanoparticles of compounds were produced, e.g. of TbDyFe and $Al_{65}Cu_{23}Fe_{12}$ [178], TiO [179] and ZrB_2 and ReB_2 [180]. The particles are produced by the decomposition after the isochoric heating as discussed above for phase trajectories that arrive at the metastable phase space at the right-hand side of the critical point. The particles were observed as a slow black-body radiator, and finally the particles were identified on a collecting material with AFM, typically on a mica substrate

on which the nanoclusters would not aggregate. This ejection of nanoparticles, which is completely absent in nanosecond-second laser ablation, is a unique feature of femtosecond-laser ablation.

For metals and semiconductors, the emission of light from the nanoclusters close to the target shows that the nanoclusters are not formed in the plume during the transfer to the substrate, but originate directly from the ejection process. The temperature T of the nanoclusters in the plume can be determined by the structureless broad background radiation from [171]

$$I(\lambda) \propto \lambda^{-5} \exp\left(\frac{-hc}{\lambda k_B T}\right), \qquad (24)$$

where the intensity I is given in terms of the emission wavelength λ, the Boltzmann constant k_B, Planck's constant h and the velocity of light c. The temperature, for example for silicon, was about 2000 K [176, 181]. These values are in agreement with the ablation models discussed above. The structureless background in the plume has also been seen for titanium oxide by Albert *et al* [179] and Sanz *et al* [182]. An example of nanoclusters of CdS collected on a mica substrate is seen in figure 19.

The black-body spectrum of the slow component in the emission spectra of TiO from Albert *et al* [179] is shown in figure 20. The plume was produced by an 80 fs laser at the wavelength 620 nm with 2 J cm^{-2}. The spectrum shown was the only light-emitting component 2–50 μs after the laser pulse and was found to move with a velocity below 1 km s^{-1} in vacuum. The emission spectrum was fitted to a black-body-like emission of a temperature of 4800 K. The authors confirmed by SEM that the surface of the deposit showed nanoclusters of size ranging from 10 to 100 nm.

The distribution of mass in the plume has been explored predominantly for metals. Amoruso *et al* [184] have shown that a fraction of 0.8 of the total mass is emitted as nanoparticles. This result was qualitatively confirmed by Noël and Hermann [185] for gold and copper, and Perriére *et al* [155] found as well that the atomic species only comprised a few percent of the emitted matter. These results were supported by hydrodynamic calculations by Povarnitsyn *et al* [169] who found that the dominant fraction of ablated material from aluminum was emitted as nanoclusters. Also Glover *et al* [186] found that the ejected material from silicon irradiated by 200 fs pulses only had a minor fraction (<0.1) ejected as atomic particles in the gas phase. The only existing study on mass distribution for dielectric materials, TiO, also showed that most of the material is ejected as nanoparticles [182]. It seems that also for dielectrics with fluences suitable for film production most of the particles will arrive as nanoclusters.

An additional feature observed for high fluences is the ejection of droplets of micrometer size from MgO and AlN targets in addition to the nanoclusters [155]. The droplets move with a characteristic velocity of 100 m s^{-1}, much slower than the nanoparticles and are clearly seen on the collecting substrate. At fluences exceeding 10 J cm^{-2} the luminescence signal from the droplets is significantly larger than that from nanoparticles. Since the two signals are clearly separated in time, the authors suggest that the droplets are not aggregated
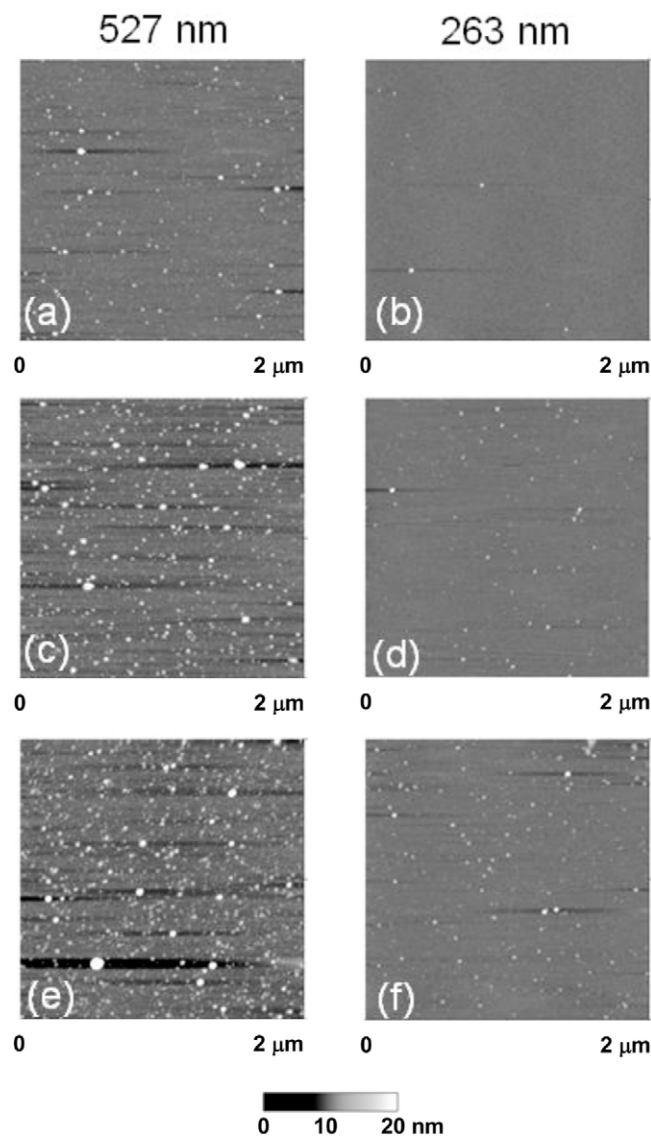
527 nm   263 nm

Figure 20. Black-body-like emission of oxidized Ti clusters in the plume from a Ti-target induced by an 80 fs laser with a wavelength of 620 nm at 2 J cm^{-2}. The composition of the nanoclusters is TiO$_x$, where $x < 0.55$. The signal is recorded 5 mm away from target in a time window of 2–50 μs appropriate for slow plume particles [179]. Reproduced with kind permission from Springer Science and Business Media.

Figure 19. AFM images of less-than-one layer CdS deposits on mica made at 527 nm with 440 μJ per pulse (left) and at 263 nm with 130 μJ per pulse (right). The number of pulses is 660 (a) and (b), 2640 (c) and (d), and 5280 (e) and (f). The dimensions of each AFM image are $2 \times 2 \, \mu m^2$. The bar indicates height from 0 to 20 nm [183]. Reprinted with permission from [183]. Copyright (2011) American Chemical Society.

nanoclusters but rather stress-induced release of material according to the model by Zhigilei [158].

3.3. Characteristic plume quantities: the velocity of the species

The typical picture of the expanding solid in figure 16 shows that the fastest atoms move with an average velocity of 3.5 km s^{-1}. This corresponds to a dense cloud of atoms with a front 70 nm outside the original surface after the electron–ion equilibrium time 20 ps, while the corresponding initial cloud from nanosecond-laser impact with a pulse of 20 ns has a thickness of 70 μm after termination of the laser pulse. After this time no more energy is transferred to the cloud and this initial plume will expand adiabatically into vacuum. This
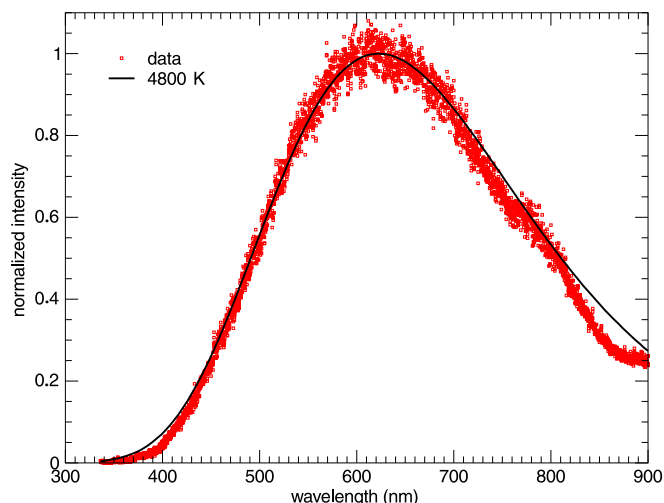
hydrodynamic expansion is primarily driven by the pressure gradients in the dense cloud [171]. The essential point is the different thicknesses of the initial cloud for femtosecond-laser impact and nanosecond-second laser impact, which as discussed below primarily influences the angular distribution of the emitted species. Both cases can be handled satisfactorily by Anisimov's isentropic treatment [187, 188].

Most of the treatments discussed above are for neutral atoms and do not include any electrostatic interaction in the plume, see the discussion on Coulomb explosion in section 2.3.4. Any deviation from charge neutrality in the initial plume may immediately lead to an enhanced acceleration in addition to the hydrodynamic flow. A number of models have been suggested, but no comprehensive treatment has appeared so far [189–192]. In this context it is interesting that Zhang *et al* [193] found that femtosecond pulses on aluminum are much more efficient in producing high-charge state (and high-energy) ions than nanosecond pulses.

It is well known that in addition to nanoclusters also atomic species and ions, even though they may constitute a minority, are seen in the luminescence spectra from metals irradiated by femtosecond lasers. Typically there is a small, fast component (mostly ions) with a velocity up to 50 km s^{-1} and a somewhat larger component with a velocity about 10 km s^{-1} (in addition to the nanoclusters with a velocity below 1 km s^{-1}) [154, 160, 177, 179].

Accurate measurements of a multi-component target were carried out with femtosecond-laser impact on La$_{0.6}$Ca$_{0.4}$CoO$_3$ with 500 fs pulses and a fluence of 3 J cm^{-2} at 248 nm by Canulescu *et al* [194]. The ionic components Ca$^+$ (15 km s^{-1}) and La$^+$ (19 km s^{-1}) were faster than the neutrals by a factor of 1.5. The velocity of the plume fronts of ions and neutrals ranged from 25 to 8 km s^{-1}. A similar behavior has been observed in two-component dielectrics for CdS irradiated with 300 fs pulses at 527 nm by Sanz *et al* [183]. The Cd-ions

showed a velocity about $30\,km\,s^{-1}$ while the Cd neutrals were moving with $10\,km\,s^{-1}$. An interesting point was that the velocity of Cd ions and atoms for UV laser pulses at 263 nm was twice as large. Also for TiO_2 Sanz *et al* [182] observed Ti atoms moving with a velocity around $10\,km\,s^{-1}$ as well as TiO molecules with a velocity of $2\,km\,s^{-1}$ after impact of 300 fs laser pulses at 527 nm. The spectrum also included fast hydrogen atoms originating from residual gas or from target impurities with a velocity of $100\,km\,s^{-1}$.

The velocity of the species produced by femtosecond-laser impact does not deviate in a pronounced way from the velocity seen in nanosecond-experiments with the same wavelength. The typical velocity found in ns experiments in vacuum ranges from 20 up to $40\,km\,s^{-1}$ at a medium fluence of $2.5\,J\,cm^{-2}$ at 355 nm [195] and up to $30\,km\,s^{-1}$ with a fluence of $8\,J\,cm^{-2}$ at 193 nm [196]. Albert *et al* [179] found that there was a fast component with a peak velocity of $50\,km\,s^{-1}$ in the fs spectrum which did not exist at nanosecond-laser impact with a comparable, but somewhat larger fluence for the same laser wavelength at 620 nm. The same group compared the velocities from ablated ZnO also at 620 nm and found that the excited plume particles induced by femtosecond pulses were substantially faster than those induced by nanosecond pulses [197]. However, the results from Canulescu *et al* [194] in the UV-regime indicate that the atom and ion velocity in the plume for nanosecond-laser and femtosecond-laser impact on $La_{0.6}Ca_{0.4}CoO_3$ at the same wavelength, 248 nm, largely are similar.

The consequence of these high velocities is that high-energy impact of ablated atoms and ions may cause sputtering of a growing film—similar to what has been observed for plumes produced by nanosecond-laser PLD. References [196, 198] have shown that a significant fraction—between 0.3 and 0.7 at a fluence of $5\,J\,cm^{-2}$—of the ablated particles at nanosecond-laser impact has an energy, which exceeds 200 eV. The atoms have sufficient energy to produce defects and preferential sputtering from a film during growth with PLD for nanosecond as well as femtosecond lasers. The effect of fast ions and neutrals bombarding nanoclusters in films produced by femtosecond lasers is not clear, but it may be a substantial effect if the atoms in the nanocluster are bound loosely compared with a uniform surface.

While the particles in a plume in vacuum eventually move with a uniform, asymptotic velocity, the particles in a plume in a background gas (with a pressure exceeding 0.01 mbar) will gradually stop and finally be confined as an ellipsoid of target plume material surrounded by a background gas. After the thermalization, the plume particles will diffuse through the background gas until they, for example, reach a substrate or a chamber wall [199]. This plume behavior in a background gas from the initial quasi-free expansion through a shockwave regime to complete slowing down is conveniently handled by the model of Predtechensky and Mayorov [200], which was extended by Amoruso *et al* [201]. This model was originally developed for nanosecond-laser impact, but turned out to be feasible for plumes produced by femtosecond lasers as well [184].
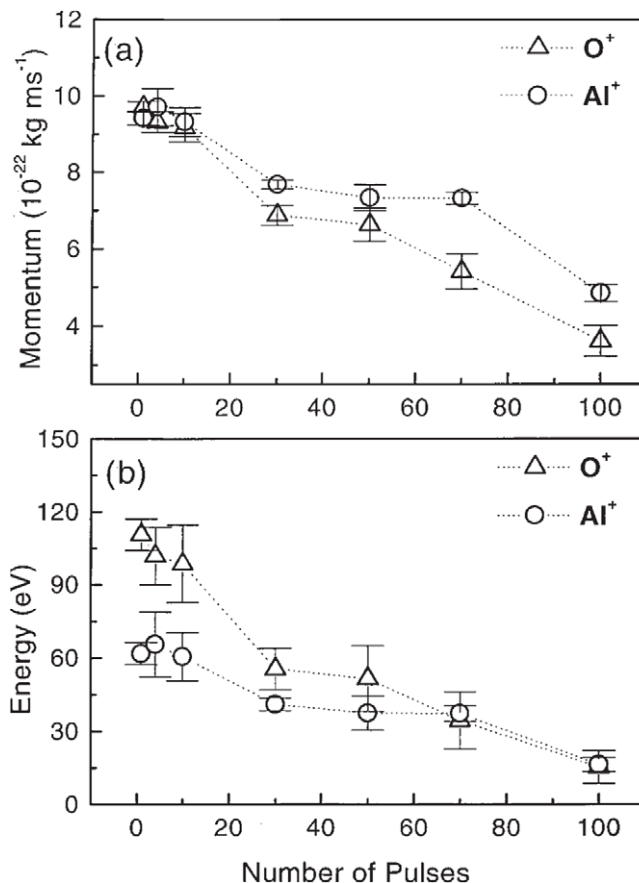
Figure 21. (*a*) Momentum and (*b*) energy of O^+ and Al^+ species within the plume emitted from a sapphire sample as a function of the number of laser shots. The values were calculated from the measured maxima in the velocity distributions. Circles, Al^+; triangles, O^+. The data show the transition from 'gentle' to strong ablation at $5\,J\,cm^{-2}$ with pulses of 100 fs at 800 nm [117]. Copyright (2000) by the American Physical Society.

3.4. Non-thermal-processes: Coulomb explosion

Until now we have considered ablation, which has been driven by laser-induced heating. A particular case of ablation occurs by non-thermal processes when subjecting dielectric materials to ultrafast irradiation, Coulomb explosion, as discussed shortly in section 2.3.4. Fast photoemission of electrons from the surface layers leads to charging and subsequent electrostatic repulsion of the atoms, of which many will be ejected out of the surface and some also be driven into the bulk. In contrast to desorption (see below), this is a macroscopic process, which includes up to more than 10^{12} atoms (or ions) per pulse. A major point is, of course, that no neutralization occurs before the atoms have been ejected. In dielectrics there is initially no pool of free electrons as in metals and partly in semiconductors, but in the high-intensity region of the dielectric, 'free' electrons in the conduction band will be generated. Thus for low intensities of ultrafast irradiation, in the so-called gentle regime [117, 118], the ions will survive sufficiently long to be ejected electrostatically in a Coulomb explosion.

The evidence of this process for sapphire is seen clearly in figure 21. The momenta of the two ions, O^+ and Al^+, have been

plotted as a function of the number of shots. The values of the momentum were calculated from values of the maximum of the velocity distributions measured [117]. The repulsion from a charged surface layer acts as long as the charges survive and exerts the constant electrostatic force F_e on the escaping (singly charged) ions. The momentum p of an ion is thus

$$p = F_e \tau_e, \tag{25}$$

where τ_e is the time duration of the surface field. For a low number of shots, the momenta of the two species in figure 21 are seen to be equal, which confirms the existence of the process. At these low shot numbers, the velocity of the ions is about $40 \, km \, s^{-1}$ for O^+ and $20 \, km \, s^{-1}$ for Al^+, which is actually comparable to the velocity observed for thermal ablation. The authors have estimated that ions from 2–3 nm of the surface are removed, while the total ablated depth is $25 \, nm \, pulse^{-1}$ of (neutral) atoms in the gentle regime. The observed momenta correspond to a surface charge of 0.65 according to the authors [117, 202]. At higher shot numbers, the defect density in the crater is so high that much more energy is absorbed and the yield becomes up to one order of magnitude larger with strong emission of plasma light and crater formation as a consequence of incubation at the impact spot; see section 2.7. In this strong ablation regime, the ions from the Coulomb explosion are still present but overshadowed by the large quantity of thermally induced ablated particles.

There is a clear parallel between the mechanisms of Coulomb explosion in a dielectric and in doubly charged nanoclusters. The cluster breaks up when the electrostatic force between the charges exceeds the binding energy of the cluster atoms [203] just as the electrostatic force per unit area on the dielectric surface also has to overcome the local stress at the surface in ablation driven by Coulomb repulsion (for the nanocluster case the momentum of the repulsing species is also observed to be equal).

An important, but not necessarily conclusive evidence of Coulomb explosion is that the ablated, doubly charged species have a velocity twice as large as the singly charged ions [117]. The non-elemental material sapphire is an exceptional system, because the momentum of the two species Al^+ and O^+ can be compared. The velocity comparison between singly and doubly charged ions of the same element is not unambiguous, since as Stoian *et al* point out [204], similar results can also be obtained from other mechanisms, such as ambipolar acceleration in plasma plumes.

Bulgakova *et al* have supported the existence of Coulomb explosion in laser ablation with a continuum model for electronic transport [202, 205]. The net charge at the surface of sapphire reaches a value of about 3×10^{21} charges cm^{-3} for a period of more than 50 fs for electrons supplied from $1 \, \mu m$ behind and for 200 fs for electrons supplied $10 \, \mu m$ behind the surface for a $4 \, J \, cm^{-2}$ pulse with a duration of 100 fs. For a critical electric field $E_e = 6 \times 10^{10} \, V \, m^{-1}$, the energy density per atomic volume of the electric field reaches the average binding energy of $5 \, eV \, atom^{-1}$ in sapphire. Under the same conditions as listed above, the calculated field $E_e = 8.4 \times 10^{10} \, V \, m^{-1}$ exceeds the critical value of the field considerably and can induce the electrostatic rupture of the

surface down to a depth of about 4 nm, which is very close to the experimentally observed value.

Coulomb explosion has been observed for a number of dielectrics such as Al_2O_3, SiO_2 [117, 118], CaF_2, BaF_2 and NaCl [206–208]. In the same setup Stoian *et al* [118] carried out pump–probe experiments on silicon and gold and found no signature of Coulomb explosion. The strong charging of sapphire at $4 \, J \, cm^{-2}$ compared with that for $0.8 \, J \, cm^{-2}$ on silicon and $1.2 \, J \, cm^{-2}$ laser pulses on gold is not the consequence of enhanced photoemission from sapphire according to Bulgakova *et al* [205]. The sapphire target loses less than 10^9 electrons, while 10^{11} electrons are removed from the silicon and gold targets. However, for semiconductors and metals, the much higher electron mobility and density of free electrons lead to a short-lived net-charging with a field about two orders below that necessary for electrostatic break-up of the surface layers as a Coulomb explosion.

The existence of Coulomb explosion as an active process in semiconductors and metals [209–211] is thus questionable. The scaling of the velocities of the doubly charged ions to twice of that of the singly charged ions and the observations of non-thermal peaks in the time-of-flight spectra may originate from other processes such as ambipolar plasma effects or desorption-like features for a fluence below the threshold. Deexcitation processes of individual atoms and molecules may also lead to ejection processes of non-thermal origin, e.g. atoms that leave a surface with a kinetic energy that is substantially larger than the thermal energy. This is also known from desorption and electronic sputtering, where a deexcitation process in an insulator releases an energy, which is sufficient to break the bonds of the atoms at the surface [212–214]. One should keep in mind that desorption as well Coulomb-explosion processes may contribute to the total ablation yield from dielectrics also at high fluences, but usually with a small fraction, which is not distinguishable in the velocity spectrum.

3.5. Characteristic plume quantities: the angular distribution of the species

The angular distribution of the plume particles determines the uniformity of a film. It has been known for decades [151, 215] that the laser ablation plume is strongly peaked in the forward direction. It means that the deposition rate on a substrate from a stationary beam spot on target is strongly non-uniform over a large area, unless the laser beam is mechanically scanned over an area of at least the same size. A second issue is that the composition of a plume from a multi-component target may change as a function of angle.

Even though the overall plume formation is similar for femtosecond and nanosecond pulses, the plume is considerably more peaked in the forward direction for femtosecond pulses than for nanosecond pulses [179, 197, 216]. This was experimentally verified for Ti, ZnO as well as $BaTiO_3$ at the same wavelength 620 nm. The plume from $BaTiO_3$ seen in figure 22 is clearly much narrower for femtosecond pulses. A similar trend was reported by Canulescu *et al* [194].

Measurements of the angular distributions of the ions/atoms as well of the total number of ablated particles at
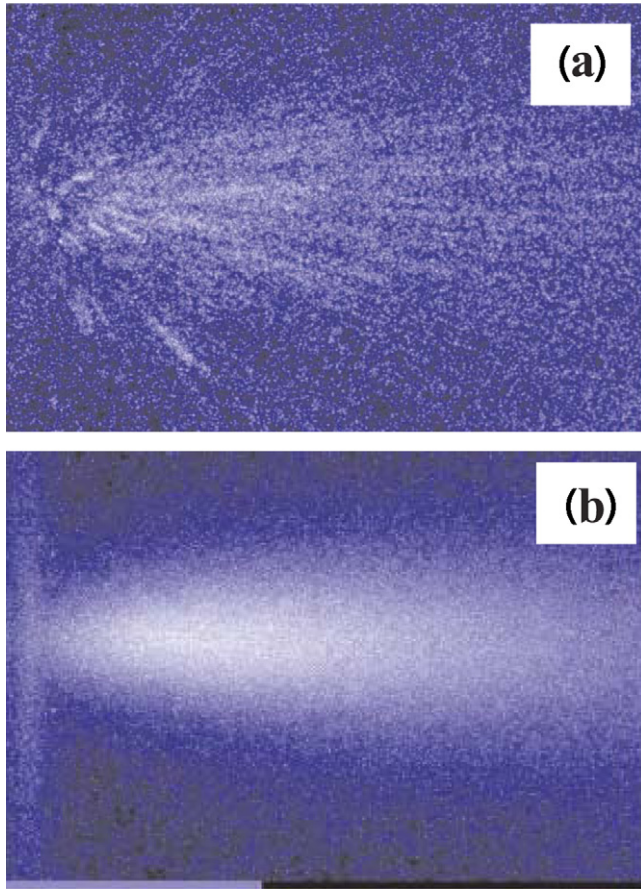
Figure 22. CCD camera plume images recorded from the laser ablation of BaTiO$_3$ 100 μs after the laser pulse of (*a*) 5 ns at 0.5 J cm^{-2} and (*b*) in the femtosecond regime for a pulse length at 90 fs and a fluence of 1 J cm^{-2}. Both pulses were at 620 nm. The size of each image is around 3 cm $\times$ 5 cm and the gray-scale intensities are on a log scale [216]. Reproduced with kind permission from Springer Science and Business Media.

fluences exceeding 1 J cm^{-2} show that the nanoclusters exhibit a much broader distribution in the UV [217] and the visible regime [218] than the ions alone or generally the 'atomic' particles do. However, at low fluences comparatively close to the threshold for ablation, Donnelly *et al* [219, 220] found the opposite behavior.

The angular distribution of the ions from a plume produced by a circular beam spot on a hemispherical surface can be well approximated with the distribution $F_A(\theta)$ derived from Anisimov's treatment [173]

$$F_A(\theta) = F_A(0) \left(1 + k^2 \tan^2 \theta\right)^{-3/2} \left(1 + \tan^2 \theta\right)^{-3/2}, \qquad (26)$$

where k is the ratio between the asymptotic plume front position Z and the lateral front position R of the plume. $F_A(0)$ is the value of the distribution for the angle $\theta = 0$ with respect to the target normal (see figure 15). Thus a high k-value means a strong peak in the forward direction and a typical value for a nickel target determined by Donnelly *et al* [219] for the total deposited material varied from $k = 9.5$ close to the threshold at 0.15 J cm^{-2} to $k = 5.6$ at 0.7 J cm^{-2} at 527 nm with 250 fs laser pulses. (The corresponding value of k for nanosecond-pulses at 248 nm on silver was found to be $k = 4.5$ for the

ionic component and 2.7 for the total mass [221]). The strong peak of the plume for femtosecond pulses reflects the fact that a small value $Z(0)/R(0)$, i.e. a very thin initial cloud prior to plume expansion, leads to a high value of k [187]. The recent results for the dielectric material, CdS, are consistent with the behavior predicted from Anisimov's theory [183].

For metals irradiated by femtosecond lasers in the UV regime at 248 nm, it has been confirmed by measurements on silver by Toftmann *et al* [217] that the angular distribution can be approximated well by Anisimov's model and also that the distribution of ions and the distribution of all ablated particles (including neutrals) are much narrower than the corresponding ones from nanosecond ablation at the same wavelength. Another evidence for the validity of Anisimov's model also for femtosecond laser ablation is the observation of the so-called flip-over effect. By this effect an elliptical ablation spot leads to a plume with the major axis orthogonal to the major axis of the ablation spot [217].

An interesting point is that the distribution of nanoclusters cannot be approximated well by Anisimov's formula at high fluence. Donnelly *et al* [219, 220] interpreted this deviation as an effect of the pressure exerted by the atomic plasma plume on the initial hydrodynamic evolution of the nanocluster component. Another point is that Claeyssens *et al* [222] demonstrated that the angular distribution of nanoclusters from a graphite target is more peaked in the forward direction for femtosecond ablation than for picosecond ablation. This agrees well with the arguments used above that a thin plume layer after termination of the femtosecond pulse leads to a narrower distribution than that generated from an initially thicker layer by a longer pulse.

There are no similar measurements for dielectric materials. However, there is no reason to believe that the angular distribution of plume particles deviates much from that of a metal as described above. Note that a complicating feature is that dielectrics are almost always multi-component materials, and the relative composition may vary for different angles. Perriére *et al* report that the Ba concentration relative to that of Ti in the angular distribution from BaTiO$_3$ increases strongly with angle for angles larger than 50° [155], while Teghil *et al* report loss of V relative to O for V$_2$O$_5$ films with increasing distance from the center of the substrate [218]. We shall return to the issue of identical stoichiometry in the target and in the films produced by femtosecond lasers in connection with the discussion of the films in section 4.

4. Films produced by femtosecond laser ablation

The early attempts to produce films by femtosecond PLD were not particularly promising [39, 216]. The optimum parameters turned out to be difficult to identify, and also different from those found in nanosecond PLD. In many cases it was found as well that the electric, structural and surface morphological properties of the films were inferior to those obtained by nanosecond PLD. However, the recent reports indicate that the picture is far more complex, and that there actually are new opportunities for femtosecond-laser produced films, and

that some of the properties of the films may not be achieved with the 'classical' nanosecond PLD.

A comprehensive list of films of 'band-gap' materials produced by femtosecond-laser ablation is shown in table 2.

4.1. Film production: special features by femtosecond lasers

The classical features, which favor the use of femtosecond lasers for film fabrication, are primarily the short interaction time with light in the solid, which as discussed above means that the impact zone is heated so rapidly that essentially no energy is lost to the surroundings by heat conduction during the laser pulse, and that the plume is generated after the termination of the pulse [154, 222]. In the latter case there is no absorption or scattering of laser light in the plume in contrast to the considerable absorption at nanosecond-laser impact already at a fluence of a few J cm^{-2}.

For dielectric materials it is possible to fabricate films by PLD for materials with low absorption, e.g. with a photon energy below the band gap, since the laser intensity is typically sufficient for multi-photon processes to take place [183]; see the discussion in section 2.3. Another point is that the appearance of microstructures (particulates >100 nm) is avoided or considerably reduced [155, 183, 246, 257].

However, although film production by femtosecond lasers thus has very promising aspects, one must consider the very important issue: the low pulse energy. Most of the current lasers have maximum pulse energies around 1 mJ, which should be compared with a typical pulse energy of 100–200 mJ for nanosecond lasers. The deposition rate on a substrate as that shown in figure 15 is determined by the total yield of ablated atoms and the angular distribution as discussed in section 3. The total number of ablated atoms per unit energy is higher for femtosecond lasers, and the distribution is more strongly peaked in the forward direction, but this does not compensate for the much smaller energy of the fs-pulses. With a large pulse energy, it is always possible to adjust the laser spot size on the target in order to work under optimum laser-fluence conditions. This means that once the energy exceeds the threshold, the deposition rate may increase roughly proportional to the pulse energy. Unfortunately, there are very few measurements of the deposition rate performed under similar conditions. Table 3 shows the rates for few examples that exist in the literature. It is clear that fs-lasers are much more efficient for film production at fluences around 1 J cm^{-2}. However, at higher pulse energies for the nanosecond lasers, the deposition rate increases strongly and is clearly superior to that of femtosecond lasers with respect to fast, practical deposition of films.

For band-gap materials the difference between the two laser types is even more striking. The practical deposition rate for the sulfides, CdS and ZnS (table 3) is at least one order of magnitude higher for the nanosecond lasers than for femtosecond lasers with a similar production geometry. This is also seen for ZnO in table 3, where the high practical deposition rate actually reflects that the laser beam spot is correspondingly larger.

It is thus clear that the deposition per pulse will be lower for femtosecond lasers. However, as discussed in section 1.1, recent developments of femtosecond lasers have demonstrated systems with a fairly high repetition rate and therefore average powers that compete with those of nanosecond lasers. Nonetheless, in order for these systems to be of use for film production, the maximum useful repetition rate is limited, since the time between pulses must exceed the time scale for the plume-expansion dynamics to avoid absorption in the plume remaining from previous laser pulses. Taking, for instance, a minimum time between pulses of 100 μs (see figure 22), the repetition rate should not exceed 10 kHz. However, with current state-of-the-art lasers, it is actually possible to have pulse energies of 1 mJ at these repetition rates. By comparing with the results in table 3, it should then be possible to increase the deposition rate of femtosecond-laser-PLD films by a factor of 300 relative to the values given in the table. For comparison, the state-of-the-art nanosecond lasers will have repetition rates that are about one order of magnitude higher than the results given in the table. This will provide quite similar deposition rates from the two laser types. Thus, it will be interesting to see whether the new femtosecond laser systems will be able to increase the deposition rates of films.

4.2. 'Nanocluster' films

A representative example of a nanoparticle-assembled film is shown in figure 23 for TiO$_2$ [182]. The films are obviously covered with a cauliflower-like agglomerate of nanoparticles and small aggregates, but no microparticulates. A similar picture was obtained for all the early works on films produced by femtosecond-lasers [152, 155, 179, 232]. From table 2, it is clear that production of nanoclusters during the film deposition is the rule rather than an exception. For the early works before 2004, it was not always recognized that nanoclusters on the film were a dominant fraction of the total deposited material.

The size of the nanoparticles has been found by employing a relatively low number of pulses for deposition on a mica substrate such that the particles size could be measured directly by AFM. A characteristic distribution of CdS nanoparticles at two different wavelengths is shown in figure 24 [183]. In both cases the most probable is value below 5 nm. The nanoparticles may land on or close to nanoparticles already present on the surface and may agglomerate to larger aggregates. This distribution is typical for femtosecond-laser deposition and has also been observed for other materials than dielectrics, including metals [176].

An interesting feature is the effect of the laser wavelength on the size of the nanoclusters. At similar fluence with respect to the ablation threshold UV ablation is characterized by a higher degree of atomization. Sanz *et al* reported that also for ZnS, the nanoclusters formed by light at a wavelength of 263 nm are smaller than those obtained at 527 nm [183]. This effect can be interpreted in terms of the thermodynamic models for isochoric heating discussed in section 3. With 263 nm light, linear absorption is possible, while for the longer wavelength, a strong-field excitation (two-photon) process is needed; see section 2.3. Nonetheless, the authors compare the effective absorption length, for the two wavelengths and find that it is somewhat smaller for UV light (a factor of 2.5 for CdS and 5 for

Table 2. Films of 'band-gap' materials produced by femtosecond-lasers.

Material	Reference	Band gap [a] (eV)	Wavelength (nm)	Nanoclusters observed	Stoichiometry preserved	Compare nanosecond lasers
$AlMgB_{10}$	Stock 2004 [223]		800	Probably	Large deviation	[b]
AlN	Ristoscu 2011 [224]	6.2 *A*	800	Yes	Prevalently AlN, traces of metallic Al	
AlN	Perriére 2007 [155]	6.2	620	Yes	Also crystallites of Al and Al_2O_3	
AlN	Gyorgy 2001 [225]	6.2 *A*	248	Probably	Stoichiometric and epitaxial films	[c]
$BaTiO_3$	Millon 2003 [216]	3.5–3.9 *A*	620	Yes	Partly	[d]
BN	Zhang 2000 [226]	∼6 [227]	780	Possibly	BN/TiN multilayer films	
CdS	Sanz 2011 [183]	2.25–2.45 *A*	263, 527	Yes	Deficit of Cd at 263 nm	
CdS	Sanz 2010 [228]	2.42 A	266, 400, 800	yes	Almost	
CdS	Tong 2008 [229]	2.48 A	800	Apparently	Yes, at lower temp.	[e]
CdS	Tong 2008 [230]		800	Yes	No information	
Cr_3C_2	Teghil 2009 [231]		527	Yes	Yes, but also presence of C	
GaAs	Dinh 2002 [232]	1.43	810	Yes	Yes	
GaAs	Trelenberg 2004 [233]	1.43	820	Yes	Yes at certain background pressure	
GaN	Tong 2008 [234]	3.4	800	Yes	Yes	[f]
Ge	Pronko 2003 [235]	0.67	780	not clear	Yes	
HfC	Teghil 2005 [236]		527	Yes	Yes	[g]
MgO	Perriére 2007 [155]	6.1–7.8 [237]	620	Yes	No information	
$Nd:Gd_3Ga_5O_{12}$ (GGG)	Darby 2008 [238]	5.4 *A*	800	Not clear, possibly	Yes, optimum for epitaxial growth found	
ReB_2	De Bonis 2011 [180]		527	Yes	Probably, no precise info	
SiC	Ghica 2006 [239]	2.9–3.0 [240]	800	Yes	Yes, but interface of β-SiC	
SnO_2	Dominguez 2002 [241]	3.6 [242]	780	Not clear	At a certain pressure epitaxial, high quality SnO_2	
TaC	Teghil 2007 [243]		250	Yes	Predominantly Ta_2C	[h]
Ti (O from residual gas)	Albert 2003 [179]		620	Yes	$TiO_{0.55}$	
TiC	Teghil 2006 [244]		529	Yes	Yes	
TiC	Teghil 2005 [236]		527	Yes	Yes	[g]
TiO_2	Sanz 2010 [182]	3.0–3.2 *A*	527	Yes	Yes, small fraction of Ti_2O_3	
TiO_2	Gámez 2010 [245]	3.0–3.2 *A*	266, 400, 800	Yes	Yes - amorphous films	[i]
TiO_2	Sanz 2009 [246]	3.0–3.2 *A*	266, 400, 800	Yes	Yes	
VC	Teghil 2009 [247]		527	Yes	No, mostly VC_2	
V_2O_5	Teghil 2009 [218]	2.3 [248]	527	Yes	Partly V_2O_5 and V_2O	[j]
WB_4	Rau 2011 [249]		527	Not directly indicated	Yes	
WC	De Bonis 2012 [250]		527	Yes	Mixture of WC and WC_{1-x} ($x < 1$)	
ZnO	Chau 2010 [251]	3.4	790	Not clear	ZnO films grown under vacuum.	
ZnO	Yang 2009 [252]	3.5	800	Yes	c-axis oriented films	[k]
ZnO	Liu 2008 [253]	3.4	1030	Yes	Yes, crystalline nanopart.	
ZnO	Yang 2008 [254]	3.4	800	Yes	c-axis oriented films	
ZnO	Klini 2005 [255]	3.4	248	Yes	Yes, apparently	[l]
ZnO	Perriére 2002 [197]	3.3 *A*	620	Yes	Yes	[m]
ZnO	Millon 2000 [40]	3.3 *A*	620	Yes	Perhaps	[n]
ZnO	Okoshi 2000 [39]	3.3	790	Not observed	Probably	[o]
ZnO:A (AZO)	Okoshi 2001 [256]		395, 790	Not identified	Not clear	

Table 2. (Continued.)

Material	Reference	Band gap [a] (eV)	Wavelength (nm)	Nanoclusters observed	Stoichiometry preserved	Compare nanosecond lasers
ZnS	Sanz 2011 [183]	3.5–3.8 *A*	263, 527	Yes	Surplus of Zn at 263 nm	
ZrB$_2$	De Bonis 2011 [180]		527	Yes	Probably, no precise info	
ZrC	Teghil 2005 [236]		527	Yes	Yes	[g]

[a] An *A* indicates that the value for the band gap is provided by the authors or from other references with the same film material. Otherwise table values from Bäuerle are used [41].

[b] Better quality (smoothness and less cracks) for femtosecond pulses, but the stoichiometry much closer to target for nanosecond pulses.

[c] All depositions performed at a substrate temperature of 900 °C. The film quality was highest for femtosecond ablation.

[d] Stoichiometry measured for films at different oxygen pressures and emission angle compared with nanosecond-laser deposition.

[e] The authors indicate that the crystal orientation at femtosecond-laser deposition is much less sensitive to substrate temperature.

[f] Optical properties better for femtosecond-laser deposition.

[g] Plasma plume characteristics different from nanosecond-produced plumes.

[h] Stoichiometric tantalum monocarbide deposited by nanosecond-PLD.

[i] Anatase and rutile crystalline phases were found in the films fabricated with nanosecond pulses (also with much larger grain size).

[j] With nanosecond-pulses films of V$_2$O$_5$ can be grown in a controlled way.

[k] Higher grain size for nanosecond-pulses.

[l] Higher mosaicity and roughness for femtosecond-ablation.

[m] Substrate at 700 °C.

[n] The crystalline quality is not as good as that obtained with nanosecond pulses.

[o] The crystallinity of the films deposited by femtosecond PLD turned out to be worse than that of the films deposited by nanosecond-pulses, but ZnO films could be produced without an oxygen background gas.

Table 3. Comparison of deposition rates by femtosecond and nanosecond lasers in the normal direction. All densities taken from Bäuerle [41].

Material, technique	Reference	Laser wavelength and repetition frequency	Fluence, pulse energy and substrate–target distance	Deposition rate per cm^2 and pulse	Practical deposition rate (nm min^{-1})
CdS fs-PLD	Sanz 2011 [183]	527 nm 33 Hz	1.5 J cm^{-2} 440 μJ 30 mm	2.86×10^{12} CdS	2.8
CdS ns-PLD	Acharya 2010 [258]	532 nm 10 Hz	1.65 J cm^{-2} — 60 mm[a]	1.18×10^{14} CdS molec	35
ZnO fs-PLD[b]	Klini 2005 [255]	248 nm 4 Hz	1.7 J cm^{-2} 3.8 mJ 60 mm	2.1×10^{13} ZnO molec	1.2
ZnO ns-PLD[b]	Klini 2005 [255]	248 nm 10 Hz	1.7 J cm^{-2} 110 mJ 60 mm	3.5×10^{14} ZnO molec.	50
ZnS fs-PLD	Sanz 2011 [183]	263 nm 33 Hz	3.5 J cm^{-2} 260 μJ 30 mm	6.25×10^{11} ZnS molec	0.5
ZnS ns-PLD	McLaughlin 1993 [259]	248 nm 50 Hz	2.5 J cm^{-2} — 30 mm	1.67×10^{14} ZnS molec.	200
Ni fs-PLD	Donnelly 2010 [220]	527 nm 33 Hz	0.35 J cm^{-2c} 455 μJ 77 mm	3.5×10^{12} Ni atoms	0.85
Ni ns-PLD	Svendsen 1996 [260]	532 nm 10 Hz[d]	1 J cm^{-2c} 10 mJ 66 mm	6.45×10^{12} Ni atoms	0.4

[a] An estimate for the deposition at a distance of 30 mm would lead to a rate twice as high, and a practical deposition rate of 70 nm min^{-1} according to the trend observed by Svendsen *et al* [260].

[b] Exactly the same setup except for pulse length of laser.

[c] The deposition rate for nickel can be approximated by a linear function of the fluence. At 1 J cm^{-2} the rate would be about 6×10^{12} Ni-atom/pulse for the femtosecond laser. However, the rate for nanosecond lasers is also proportional to the fluence and the fluence can easily be enhanced to 10 J cm^{-2}, which would lead to about 6.45×10^{13} Ni-atoms per pulse.

[d] The laser was because of the sensitive substrate, a quartz crystal microbalance, operated with 6 s between each shot.

ZnS). This means that the volume element corresponding to the shorter wavelength reaches the decomposition and atomization regime. In contrast, the visible light does not heat the laser-excited volume to similarly high temperatures, but starts the cooling in the regime, where it induces phase explosion and fragmentation. The same trend was also reported for other combinations of wavelengths for CdS [228]. For large-size aggregates formed by accumulation of individual nanoclusters arriving nearby at the same location on the substrate this dependence on wavelength was seen as well [183].
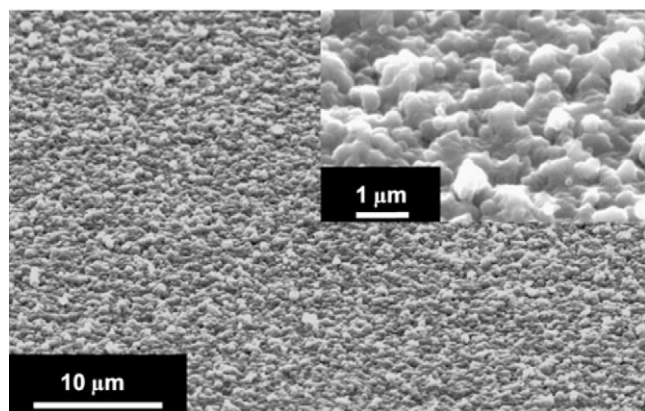
Figure 23. Representative environmental SEM (E-SEM) image of NP-assembled TiO$_2$ film deposited at a laser fluence $F \simeq 3 \times F_{th}$. The *inset* in the upper-right corner shows a magnified image. A scale bar appears in each image [182]. Reproduced with kind permission from Springer Science and Business Media.

Obviously, the structure of the 'nanocluster'-films reflects the origin of the nanoclusters. Sanz *et al* [183] indicate that the nanoclusters are likely to be single-crystalline particles.

For large nanoclusters of metals, it is known that the tail of the size distribution falls off as $r^{-3.5}$, where r is the radius [261]. Similar studies of the size distribution of nanocluster radii of dielectrics are not directly available.

4.3. Stoichiometry of femtosecond-laser films

A very important point is whether or not the stoichiometry is conserved during femtosecond-laser PLD. It is clear from table 2 that the material transfer from target to film in a stoichiometric way actually occurs for many target materials, but also that there are combinations of laser fluence, target material and background pressure, where the composition of the film deviates significantly from that of the target. This is not different from the PLD process with nanosecond-laser ablation [150]. As discussed above, the material transfer in nanoclusters tends to give a composition close to that of the target. However, this is counteracted by the enhanced number of fast ions generated during femtosecond-laser ablation compared with nanosecond-laser ablation, which can induce preferential sputtering of the film and partly dilute the least bound component on the film surface (often oxygen) [197, 198, 218].

Another point is the non-stoichiometric evaporation from a target under laser irradiation, which was observed by Trelenberg *et al* [233]. These authors have pointed out that the effect could be reduced by a background gas, which could lead to an enhanced cooling of the target compared with the vacuum case.

Teghil *et al* [218] pointed out that since the films produced by femtosecond-laser pulses largely consist of aggregated nanoclusters, evaporation from the nanoclusters during the flight from the target to the substrate may have a substantial influence on the composition of the film. The evaporation from the nanoclusters leads to dilution of the most volatile component of the nanocluster. These authors have found
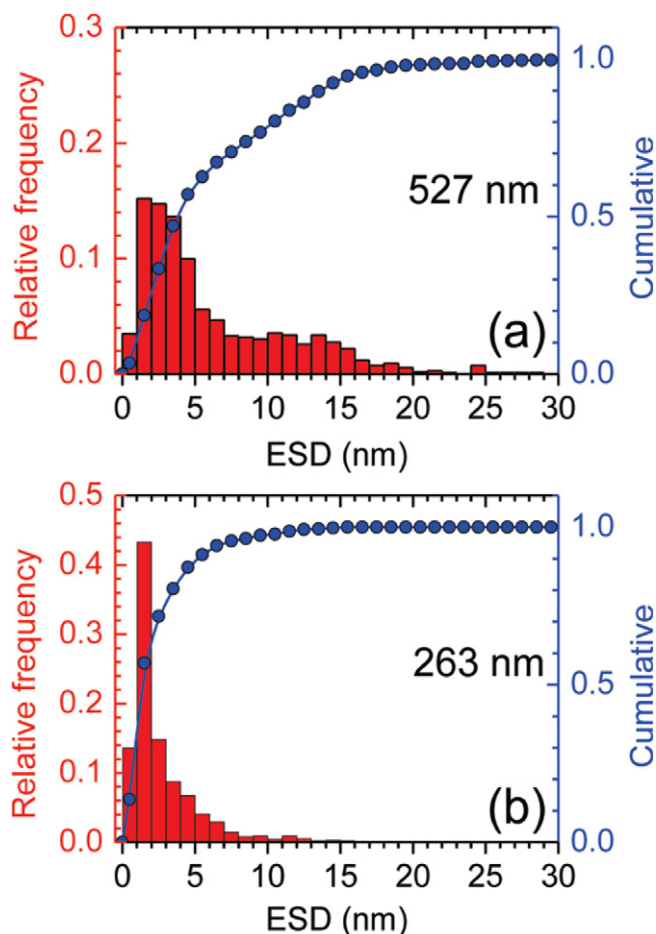

Figure 24. Size distribution of the equivalent spherical diameter (ESD) of CdS-deposited nanoparticles grown with 2640 pulses (*a*) of 440 μJ at 527 nm and (*b*) of 130 μJ at 263 nm [183]. Reprinted with permission from [183]. Copyright (2011) American Chemical Society.

that, for example, the oxygen content in V$_2$O$_5$ cannot be maintained even in an oxygen background atmosphere, since the nanocluster (which has a high temperature, see, e.g., figure 20) has very little uptake of oxygen atoms during the flight. Apparently, the compensation for loss of oxygen by collisions with the background gas molecules works much better for nanosecond PLD, in which the particle flow largely is atomized.

5. Conclusion and outlook

The mechanisms governing femtosecond-laser excitation of dielectric materials are quite complex. The understanding of the interplay between the excitation, the optical properties and the material response is still improving, and although the basic mechanisms have been identified for years, a detailed quantitative description, which can reproduce—and hopefully even predict—experimental observables from first principles, has yet to be developed. On the theoretical side, the development is closely linked to a good description of the optical properties of warm dense matter and to more complete theoretical descriptions of highly excited solid

materials including the excitation-dependent band structure and the response of such materials to strong electromagnetic fields. From the experimental side, much information can still be obtained from systematic measurements of such apparently simple quantities as hole geometries (depth and diameter) *versus* various laser parameters (fluence, pulse duration and wavelength). A few systematic investigations have been undertaken, but many regions of parameter space remain unexplored, particularly when considering the important case of single-shot irradiation. In addition, such measurements should be undertaken on a range of materials of both different material structure and band gap. Time-resolved optical measurements can be used to benchmark the theoretical description of the time-dependent optical properties, particularly at comparatively low excitation levels. Time-resolved structural measurements (e.g. time-resolved x-ray diffraction) have been used to gain insight into the ultrafast structural dynamics of semiconductors, and in the future—through the use of modern short-x-ray sources such as x-ray free-electron lasers—one can hope that similar experiments can provide a deeper insight into the dynamics of femtosecond-laser-excited dielectrics.

The material ejected by femtosecond-laser ablation can be used to produce films with properties that differ from those obtainable with longer (nanosecond) pulse lasers. The structure of the films is a signature of the different ejection and plume dynamics, which generally leads to the formation of a large fraction of nanoclusters. Furthermore, the femtosecond lasers facilitate the ablation of materials, which are otherwise inaccessible by laser excitation, e.g. because they are transparent to light. The demonstrated strong effect of the pulse duration on the film properties holds the promise that in the future, it will be possible to use the detailed control of laser pulses, which is possible with ultrashort lasers, to control the film growth and quality in new directions. The future of femtosecond-laser-based film growth is also dependent on the successful demonstration of efficient film production by the newly developed high-average-power femtosecond laser systems.

Acknowledgments

References

[1] Bäuerle D 2010 Laser chemical processing: an overview to the 30th anniversary *Appl. Phys.* A **101** 447–59
[2] Keldysh L V 1965 Ionization in field of a strong electromagnetic wave *Sov. Phys. JETP—USSR* **20** 1307
[3] Bloembergen N 1974 Laser-induced electric breakdown in solids *IEEE J. Quantum Electron.* **QE10** 375–86
[4] Bloembergen N 1997 A brief history of light breakdown *1996 Conf. on Nonlinear Optics (NLO 96) (Maio, Hawaii, 8 July 1996) J. Nonlinear Opt. Phys. Mater.* **6** 377–85

[5] Campbell E E B, Ashkenasi D and Rosenfeld A 1999 Ultra-short-pulse laser irradiation and ablation of dielectrics *Lasers in Materials Science* (*Materials Science Forum* vol 301) (Zurich-uetikon, Switzerland: Transtec publications Ltd) pp 123–44
[6] Kruger J and Kautek W 2004 Ultrashort pulse laser interaction with dielectrics and polymers *Polymers and Light* (*Advances in Polymer Science* vol 168) ed T K Lippert (Springer: Berlin) pp 247–89
[7] Gamaly E G 2011 The physics of ultra-short laser interaction with solids at non-relativistic intensities *Phys. Rep.* **508** 91–243
[8] Gattass R R and Mazur E 2008 Femtosecond laser micromachining in transparent materials *Nature Photon.* **2** 219–25
[9] Poumellec B, Lancry M, Chahid-Erraji A and Kazansky P G 2011 Modification thresholds in femtosecond laser processing of pure silica: review of dependencies on laser parameters [Invited] *Opt. Mater. Express* **1** 766–82
[10] Krausz F, Fermann M E, Brabec T, Curley P F, Hofer M, Ober M H, Spielmann C, Wintner E and Schmidt A J 1992 Femtosecond solid-state lasers *IEEE J. Quantum Electron.* **28** 2097–122
[11] French P M W 1995 The generation of ultrashort laser-pulses *Rep. Prog. Phys.* **58** 169–262
[12] Backus S, Durfee C G, Murnane M M and Kapteyn H C 1998 High power ultrafast lasers *Rev. Sci. Instrum.* **69** 1207–23
[13] Brabec T and Krausz F 2000 Intense few-cycle laser fields: frontiers of nonlinear optics *Rev. Mod. Phys.* **72** 545–91
[14] Keller U 2004 Ultrafast solid-state lasers *Progress in Optics* (*Progress in Optics* vol 46) (Amsterdam: Elsevier) pp 1–115
[15] Shank C V 1988 Generation of ultrashort optical pulses *Top. Appl. Phys.* **60** 5–34
[16] De Spence, Kean P N and Sibbett W 1991 60 fsec pulse generation from a self-mode-locked Ti-sapphire laser *Opt. Lett.* **16** 42–4
[17] Strickland D and Mourou G 1985 Compression of amplified chirped optical pulses *Opt. Commun.* **56** 219–21
[18] Fermann M E 2003 Ultrafast fiber oscillators *Ultrafast Lasers: Technology and Applications* (*Optical Engineering*) ed M E Fermann *et al* (New York: Marcel Dekker Inc) pp 89–154
[19] Limpert J, Roser F, Schreiber T and Tunnermann A 2006 High-power ultrafast fiber laser systems *IEEE J. Sel. Top. Quantum Electron.* **12** 233–44
[20] Tuennermann A, Schreiber T and Limpert J 2010 Fiber lasers and amplifiers: an ultrafast performance evolution *Appl. Opt.* **49** F71–8
[21] Shank C V, Yen R and Hirlimann C 1983 Time-resolved reflectivity measurements of femtosecond-optical-pulse induced phase-transitions in silicon *Phys. Rev. Lett.* **50** 454–7
[22] Kuper S and Stuke M 1987 Femtosecond UV excimer laser ablation *Appl. Phys.* B **44** 199–204
[23] Ihlemann J, Wolff B and Simon P 1992 Nanosecond and femtosecond excimer laser ablation of fused-silica *Appl. Phys.* A **54** 363–8
[24] Kautek W and Kruger J 1994 Femtosecond Pulse Laser-Ablation Of Metallic, Semiconducting, Ceramic, And Biological-Materials *Laser Materials Processing: Industrial And Microelectronics Applications* (*Proceedings of the Society of Photo-Optical Instrumentation Engineers (SPIE)* vol 2207) ed E Beyer *et al SPIE—Int. Soc Optical Engineering. Symp. on Laser Materials Processing: Industrial and Microelectronics Applications (Vienna, Austria, 5–8 April 1994)* pp 600–11 (doi:10.1117/12.184768)

[25] Du D, Liu X, Korn G, Squier J and Mourou G 1994 Laser-induced breakdown by impact ionization in SiO_2 with pulse widths from 7 ns to 150 fs *Appl. Phys. Lett.* **64** 3071–3

[26] Pronko P P, Dutta S K, Squier J, Rudd Jv, Du D and Mourou G 1995 Machining of submicron holes using a femtosecond laser at 800 nm *Opt. Commun.* **114** 106–10

[27] Preuss S, Demchuk A and Stuke M 1995 Subpicosecond uv laser-ablation of metals *Appl. Phys.* A **61** 33–7

[28] Chichkov B N, Momma C, Nolte S, vonAlvensleben F and Tunnermann A 1996 Femtosecond, picosecond and nanosecond laser ablation of solids *Appl. Phys.* A **63** 109–15

[29] Smith D L 1995 *Thin-film Deposition: Principles and Practice* (New York: McGraw-Hill)

[30] Musil J, Vlcek J and Baroch P 2006 Magnetron discharges for thin films plasma processing *Materials Surface Processing by Direct Energy Techniques* ed Y Pauleau (Amsterdam: Elsevier) pp 67–110

[31] Cheung J T 1994 History and fundamentals of pulsed laser deposition *Pulsed Laser Deposition of Thin Films* ed D B Chrisey and G Hubler (New York: Wiley) pp 1–22

[32] Smith H M and Turner A F 1965 Vacuum deposited thin films using a ruby laser *Appl. Opt.* **4** 147–8

[33] Hass G and Ramsey J B 1969 Vacuum deposition of dielectric and semiconductor films by a CO_2 laser *Appl. Opt.* **8** 1115–8

[34] Desserre J and Eloy J F 1975 Interaction of pulsed coherent light-beam with complex target—application to production of thin-film compounds *Thin Solid Films* **29** 29–41

[35] Dijkkamp D, Venkatesan T, Wu X D, Shaheen S A, Jisrawi N, Minlee Y H, Mclean W L and Croft M 1987 Preparation of Y–Ba–Cu oxide superconductor thin-films using pulsed laser evaporation from high-T_c bulk material *Appl. Phys. Lett.* **51** 619–21

[36] Rijnders G and Blank D H A 2007 Growth kinetics during pulsed laser deposition *Pulsed Laser Deposition of Thin Films* ed R Eason (Hoboken: Wiley) pp 177–90

[37] Qian F, Singh R K, Dutta S K and Pronko P P 1995 Laser deposition of diamond-like carbon-films at high intensities *Appl. Phys. Lett.* **67** 3120–2

[38] Okoshi M, Higuchi S and Hanabusa M 1999 Femtosecond laser ablation of frozen acetone for deposition of diamond-like carbon films *J. Appl. Phys.* **86** 1768–70

[39] Okoshi M, Higashikawa K and Hanabusa M 2000 Pulsed laser deposition of ZnO thin films using a femtosecond laser *Symp. A on Photo-Excited Processes, Diagnostics and Applications of the 1999 E-MRS Spring Conf. (Strasbourg, France, 1–4 June 1999) Appl. Surf. Sci.* **154** 424–7

[40] Millon E, Albert O, Loulergue J C, Etchepare J, Hulin D, Seiler W, and Perrière J 2000 Growth of heteroepitaxial ZnO thin films by femtosecond pulsed-laser deposition *J. Appl. Phys.* **88** 6937–9

[41] Bäuerle D 2011 *Laser Processing and Chemistry* 4th edn (Berlin: Springer)

[42] Ready J F 2001 *LIA Handbook of Laser Materials Processing* (Orlando: Laser Institute of America)

[43] Sokolowski-Tinten K and von der Linde D 2004 Ultrafast phase transitions and lattice dynamics probed using laser-produced x-ray pulses *J. Phys.: Condens. Matter* **16** R1517–36

[44] Hsu E M, Mailman N A, Botton G A and Haugen H K 2011 Microscopic investigation of single-crystal diamond following ultrafast laser irradiation *Appl. Phys.* A **103** 185–92

[45] Lausten R and Balling P 2001 On-the-fly depth profiling during ablation with ultrashort laser pulses: a tool for accurate micromachining and laser surgery *Appl. Phys. Lett.* **79** 884–6

[46] Webster P J L, Yu J X Z, Leung B Y C, Anderson M D, Yang V X D and Fraser J M 2010 *In situ* 24 kHz coherent imaging of morphology change in laser percussion drilling *Opt. Lett.* **35** 646–8

[47] Liu J M 1982 Simple technique for measurements of pulsed gaussian-beam spot sizes *Opt. Lett.* **7** 196–8

[48] Puerto D, Gawelda W, Siegel J, Bonse J, Bachelier G and Solis J 2008 Transient reflectivity and transmission changes during plasma formation and ablation in fused silica induced by femtosecond laser pulses *Appl. Phys.* A **92** 803–8

[49] Vestentoft K and Balling P 2006 Formation of an extended nanostructured metal surface by ultra-short laser pulses: single-pulse ablation in the high-fluence limit *Appl. Phys.* A **84** 207–13

[50] Christensen B H, Vestentoft K and Balling P 2007 Short-pulse ablation rates and the two-temperature model *Appl. Surf. Sci.* **253** 6347–52

[51] Preuss S, Spath M, Zhang Y and Stuke M 1993 Time resolved dynamics of subpicosecond laser ablation *Appl. Phys. Lett.* **62** 3049–51

[52] Kruger J and Kautek W 1999 The femtosecond pulse laser: a new tool for micromachining *Laser Phys.* **9** 30–40

[53] Puerto D, Siegel J, Gawelda W, Galvan-Sosa M, Ehrentraut L, Bonse J and Solis J 2010 Dynamics of plasma formation, relaxation, and topography modification induced by femtosecond laser pulses in crystalline and amorphous dielectrics *J. Opt. Soc. Am.* B **27** 1065–76

[54] Audebert P *et al* 1994 Space-time observation of an electron-gas in SiO_2 *Phys. Rev. Lett.* **73** 1990–3

[55] Mao S S, Quere F, Guizard S, Mao X, Russo R E, Petite G and Martin P 2004 Dynamics of femtosecond laser interactions with dielectrics *Appl. Phys.* A **79** 1695–709

[56] Vu B T V, Landen O L and Szoke A 1995 Time-resolved probing of femtosecond laser-produced plasmas in transparent solids by electron thermal transport *Phys. Plasmas* **2** 476–85

[57] vonderLinde D and Schuler H 1996 Breakdown threshold and plasma formation in femtosecond laser–solid interaction *J. Opt. Soc. Am.* B **13** 216–22

[58] Seuthe T, Höfner M, Reinhardt F, Tsai W J, Bonse J, Eberstein M, Eichler H J and Grehn M 2012 Femtosecond laser-induced modification of potassium-magnesium silicate glasses: an analysis of structural changes by near edge x-ray absorption spectroscopy *Appl. Phys. Lett.* **100** 224101

[59] Chan J W, Huser T, Risbud S and Krol D M 2001 Structural changes in fused silica after exposure to focused femtosecond laser pulses *Opt. Lett.* **26** 1726–8

[60] Little D J, Ams M, Gross S, Dekker P, Miese C T, Fuerbach A and Withford M J 2011 Structural changes in BK7 glass upon exposure to femtosecond laser pulses *J. Raman Spectrosc.* **42** 715–18

[61] Couprie M-E and Filhol J-M 2008 X radiation sources based on accelerators *C. R. Phys.* **9** 487–506

[62] Abramowitz M and Stegun I A 1964 *Handbook of Mathematical Functions with Gormulas, Graphs, and Mathematical Tables* (Washington, DC: National Bureau of Standards)

[63] Tien A C, Backus S, Kapteyn H, Murnane M and Mourou G 1999 Short-pulse laser damage in transparent materials as a function of pulse duration *Phys. Rev. Lett.* **82** 3883–6

[64] Gruzdev V E 2004 Laser-induced ionization of solids: back to Keldysh *Laser-Induced Damage In Optical Materials: 2004* (*Proceedings of the Society of Photo-Optical Instrumentation Engineers (SPIE)* vol 5647) ed G J Exarhos *et al 36th Annual Boulder Damage*

Symposium on Optical Materials for High Power Lasers, NIST (Boulder, CO, 20–22 September 2004) pp 480–92 (doi:10.1117/12.585170)

[65] Kaiser A, Rethfeld B, Vicanek M and Simon G 2000 Microscopic processes in dielectrics under irradiation by subpicosecond laser pulses *Phys. Rev.* B **61** 11437–50

[66] Ammosov M V, Delone N B and Krainov V P 1986 Tunnel ionization of complex atoms and of atomic ions in an alternating electromagnetic field *Sov. Phys. JETP—USSR* **64** 1191

[67] Du D, Liu X and Mourou G 1996 Reduction of multi-photon ionization in dielectrics due to collisions *Appl. Phys.* B **63** 617–21

[68] Temnov V V, Sokolowski-Tinten K, Zhou P, El-Khamhawy A and von der Linde D 2006 Multiphoton ionization in dielectrics: Comparison of circular and linear polarization *Phys. Rev. Lett.* **97** 237403

[69] Gertsvolf M, Spanner M, Rayner D M and Corkum P B 2010 Demonstration of attosecond ionization dynamics inside transparent solids *J. Phys. B: At. Mol. Opt. Phys.* **43** 131002

[70] Gaier L N, Lein M, Stockman M I, Yudin G L, Corkum P B, Ivanov M Y and Knight P L 2005 Hole-assisted energy deposition in dielectrics and clusters in the multiphoton regime *J. Mod. Opt.* **52** 1019–30

[71] Gruzdev V E 2007 Photoionization rate in wide band-gap crystals *Phys. Rev.* B **75** 205106

[72] Gruzdev V E and Chen J K 2008 Laser-induced ionization and intrinsic breakdown of wide band-gap solids *Appl. Phys.* A **90** 255–61

[73] Itina T E and Shcheblanov N 2010 Electronic excitation in femtosecond laser interactions with wide-band-gap materials *Appl. Phys.* A **98** 769–75

[74] Shcheblanov N S, Silaeva E P and Itina T E 2012 Electronic excitation and relaxation processes in wide band gap dielectric materials in the transition region of the Keldysh parameter *Appl. Surf. Sci.* **258** 9417–20

[75] Stuart B C, Feit M D, Rubenchik A M, Shore B W and Perry M D 1995 Laser-induced damage in dielectrics with nanosecond to subpicosecond pulses *Phys. Rev. Lett.* **74** 2248

[76] Stuart B C, Feit M D, Herman S, Rubenchik A M, Shore B W and Perry M D 1996 Nanosecond-to-femtosecond laser-induced breakdown in dielectrics *Phys. Rev.* B **53** 1749

[77] Varel H, Ashkenasi D, Rosenfeld A, Herrmann R, Noack F and Campbell E E B 1996 Laser-induced damage in SiO$_2$ and CaF$_2$ with picosecond and femtosecond laser pulses *Appl. Phys.* **62** 293–4

[78] Lenzner M, Kruger J, Sartania S, Cheng Z, Spielmann C, Mourou G, Kautek W and Krausz F 1998 Femtosecond optical breakdown in dielectrics *Phys. Rev. Lett.* **80** 4076–9

[79] Guizard S, Martin P, Daguzan P, Petite G, Audebert P, Geindre J P, Dossantos A and Antonnetti A 1995 Contrasted behavior of an electron-gas in MgO, Al$_2$O$_3$ and SiO$_2$ *Europhys. Lett.* **29** 401–6

[80] Petite G, Daguzan P, Guizard S and Martin P 1996 Conduction electrons in wide-bandgap oxides: A subpicosecond time-resolved optical study *3rd Int. Conf. on Swift Heavy Ions in Matter (SHIM 95) (Caen, France, 15–19 May, 1995) Nucl. Instrum. Methods Phys. Res.* **107** 97–101

[81] Martin P, Guizard S, Daguzan P, Petite G, DOliveira P, Meynadier P and Perdrix M 1997 Subpicosecond study of carrier trapping dynamics in wide-band-gap crystals *Phys. Rev.* B **55** 5799–810

[82] Li M, Menon S, Nibarger J P and Gibson G N 1999 Ultrafast electron dynamics in femtosecond optical breakdown of dielectrics *Phys. Rev. Lett.* **82** 2394–7

[83] Petite G, Guizard S, Martin P and Quere F 1999 Comment on 'Ultrafast electron dynamics in femtosecond optical breakdown of dielectrics' *Phys. Rev. Lett.* **83** 5182

[84] Noack J and Vogel A 1999 Laser-induced plasma formation in water at nanosecond to femtosecond time scales: calculation of thresholds, absorption coefficients, and energy density *IEEE J. Quantum Electron.* **35** 1156–67

[85] Kennedy P K 1995 A first-order model for computation of laser-induced breakdown thresholds in ocular and aqueous-media: I. Theory *IEEE J. Quantum Electron.* **31** 2241–9

[86] Sarpe C, Koehler J, Winkler T, Wollenhaupt M and Baumert T 2012 Real-time observation of transient electron density in water irradiated with tailored femtosecond laser pulses *New J. Phys.* **14** 075021

[87] Vogel A, Noack J, Huttman G and Paltauf G 2005 Mechanisms of femtosecond laser nanosurgery of cells and tissues *Appl. Phys.* B **81** 1015–47

[88] Gamaly E G, Rode A V, Luther-Davies B and Tikhonchuk V T 2002 Ablation of solids by femtosecond lasers: ablation mechanism and ablation thresholds for metals and dielectrics *Phys. Plasmas* **9** 949–57

[89] Rethfeld B 2004 Unified model for the free-electron avalanche in laser-irradiated dielectrics *Phys. Rev. Lett.* **92** 187401

[90] Rethfeld B 2006 Free-electron generation in laser-irradiated dielectrics *Phys. Rev.* B **73** 035101

[91] Christensen B H and Balling P 2009 Modeling ultrashort-pulse laser ablation of dielectric materials *Phys. Rev.* B **79** 155424

[92] Christensen M N, Byskov-Nielsen J, Christensen B H and Balling P 2010 Single-shot ablation of sapphire by ultrashort laser pulses *Appl. Phys.* A **101** 279–82

[93] Wædegaard K, Frislev M, Kjær L A and Balling P 2012 Femtosecond laser excitation of dielectric materials: optical properties and ablation (*AIP Conference Proceedings* vol 1464) ed C Phipps *Int. Symposium on High Power Laser Ablation (HPLA) (Santa Fe, NM, 30 April-3 May 2012)* pp 32–43 (doi:10.1063/1.4739858)

[94] Wædegaard K, Frislev M and Balling P 2012 Femtosecond laser excitation of dielectric materials: experiments and modeling of optical properties and ablation depths *Appl. Phys.* A DOI:10.1007/s00339-012-7136-7

[95] Landau L D and Lifshitz E M 1960 *Electrodynamics of Continuous Media* (Oxford: Pergamon)

[96] Ashcroft N W and Mermin N D 1976 *Solid State Phys.* (Philadelphia, PA, USA: Brooks/Cole)

[97] Guizard S, Semerok A, Gaudin J, Hashida A, Martin P and Quere F 2002 Femtosecond laser ablation of transparent dielectrics: measurement and modelisation of crater profiles *Spring Meeting of the European-Materials-Research-Society (Strasbourg, France, 5–8 June, 2001) Appl. Surf. Sci.* **186** 364–8

[98] Quere F, Guizard S and Martin P 2001 Time-resolved study of laser-induced breakdown in dielectrics *Europhys. Lett.* **56** 138–44

[99] Rethfeld B, Krutsch H and Hoffmann D H H 2010 Tracing laser-induced dielectric breakdown in solids *13th Int. Conf. on Physics of Non-Ideal Plasmas (Chemogolovka, Russia, 13–18 September, 2009) Contrib. Plasma Phys.* **50** 16–20

[100] Rethfeld B, Brenk O, Medvedev N, Krutsch H and Hoffmann D H H 2010 Interaction of dielectrics with femtosecond laser pulses: application of kinetic approach and multiple rate equation *Appl. Phys.* A **101** 19–25

[101] Feit M D, Komashko A M and Rubenchik A M 2004 Ultra-short pulse laser interaction with transparent dielectrics *Appl. Phys.* A **79** 1657–61

[102] Yakovlev D G and Urpin V A 1980 Thermal and electrical conductivity in white dwarfs and neutron stars *Sov. Astron.* **24** 303–10

[103] Eidmann K, Meyer-ter Vehn J, Schlegel T and Huller S 2000 Hydrodynamic simulation of subpicosecond laser interaction with solid-density matter *Phys. Rev.* E **62** 1202–14

[104] Arnold D, Cartier E and Dimaria D J 1992 Acoustic-phonon runaway and impact ionization by hot-electrons in silicon dioxide *Phys. Rev.* B **45** 1477–80

[105] Arnold D, Cartier E and Dimaria D J 1994 Theory of high-field electron-transport and impact ionization in silicon dioxide *Phys. Rev.* B **49** 10278–97

[106] Huba J D 2011 *NRL Plasma Formulary* Naval Research Laboratory Publication, Washington, DC

[107] Lee Y T and More R M 1984 An electron conductivity model for dense-plasmas *Phys. Fluids* **27** 1273–86

[108] Kruer W L 1988 *The Physics of Laser Plasma Interactions* (Redwood City, CA: Addison-Wesley Publishing Company)

[109] Chimier B, Uteza O, Sanner N, Sentis M, Itina T, Lassonde P, Legare F, Vidal F and Kieffer J C 2011 Damage and ablation thresholds of fused-silica in femtosecond regime *Phys. Rev.* B **84** 094104

[110] Jiang L and Tsai H L 2005 Energy transport and material removal in wide bandgap materials by a femtosecond laser pulse *Int. J. Heat Mass Transfer* **48** 487–99

[111] Rudolph W, Emmert L A, Ngyuen D, Karras C, Sun Z and Weber R 2011 Subpicosecond laser breakdown in optical thin films *Pacific Rim Laser Damage 2011: Optical Materials For High Power Lasers* (*Proceedings of SPIE* vol 8206) ed C J Shao *et al 1st Pacific Rim Laser Damage Symposium on Optical Materials for High Power Lasers (PLD) (Shanghai, Peoples Republic of China, 6–9 November, 2011*)

[112] Quere F, Guizard S, Martin P, Petite G, Gobert O, Meynadier P and Perdrix M 1999 Ultrafast carrier dynamics in laser-excited materials: subpicosecond optical studies *206th WE Heraeus Seminar Nonlinear Optics at Interfaces (NOPTI 98) (Berlin, Germany, 21–24 September 1998) Appl. Phys.* B **68** 459–63

[113] Penano J R, Sprangle P, Hafizi B, Manheimer W and Zigler A 2005 Transmission of intense femtosecond laser pulses into dielectrics *Phys. Rev.* E **72** 036412

[114] Petrov G M and Davis J 2008 Interaction of intense ultra-short laser pulses with dielectrics *J. Phys. B: At. Mol. Opt. Phys.* **41** 025601

[115] Jiang L and Tsai H-L 2008 A plasma model combined with an improved two-temperature equation for ultrafast laser ablation of dielectrics *J. Appl. Phys.* **104** 093101

[116] Brenk O and Rethfeld B 2011 Electron dynamics in transparent materials under high-intensity laser irradiation *Laser-Induced Damage In Optical Materials: 2011* (*Proceedings of SPIE* vol 8190) ed G J Exarhos *et al 43rd Annual Laser Damage Symposium on Optical Materials for High Power Lasers (Natl Inst Stand & Technol, Boulder, CO, 18–21 September, 2011*) (doi:10.1117/12.899189)

[117] Stoian R, Ashkenasi D, Rosenfeld A and Campbell E E B 2000 Coulomb explosion in ultrashort pulsed laser ablation of Al_2O_3 *Phys. Rev.* B **62** 13167–73

[118] Stoian R, Rosenfeld A, Ashkenasi D, Hertel I V, Bulgakova N M and Campbell E E B 2002 Surface charging and impulsive ion ejection during ultrashort pulsed laser ablation *Phys. Rev. Lett.* **88** 097603

[119] Jiang L and Tsai H L 2004 Prediction of crater shape in femtosecond laser ablation of dielectrics *J. Phys. D: Appl. Phys.* **37** 1492–6

[120] Jiang L and Tsai H L 2006 Plasma modeling for ultrashort pulse laser ablation of dielectrics *J. Appl. Phys.* **100** 023116

[121] Bourgeade A, Mezel C and Saut O 2010 Modeling the early ionization of dielectrics by ultrashort laser pulses *J. Sci. Comput.* **44** 170–90

[122] Arnold C L, Heisterkamp A, Ertmer W and Lubatschowski H 2007 Computational model for nonlinear plasma formation in high NA micromachining of transparent materials and biological cells *Opt. Express* **15** 10303–17

[123] Guizard S, Fedorov N, Mouskeftaras A and Klimentov S 2010 *Femtosecond Laser Ablation of Dielectrics: Experimental Studies of Fundamental Processes* (*AIP Conference Proceedings* vol 1278) ed C R Phipps *Int. Symp. on High Power Laser Ablation 2010 (Santa Fe, NM, 18–22 April, 2010)* pp 336–46

[124] Jia T Q *et al* 2006 Ultraviolet-infrared femtosecond laser-induced damage in fused silica and CaF_2 crystals *Phys. Rev.* B **73** 054105

[125] Kautek W, Kruger J, Lenzner M, Sartania S, Spielmann C and Krausz F 1996 Laser ablation of dielectrics with pulse durations between 20 fs and 3 ps *Appl. Phys. Lett.* **69** 3146–8

[126] Louzon E, Henis Z, Pecker S, Ehrlich Y, Fisher D, Fraenkel M and Zigler A 2005 Reduction of damage threshold in dielectric materials induced by negatively chirped laser pulses *Appl. Phys. Lett.* **87** 241903

[127] Mero M, Liu J, Rudolph W, Ristau D and Starke K 2005 Scaling laws of femtosecond laser pulse induced breakdown in oxide films *Phys. Rev.* B **71** 115109

[128] Xu S Z, Jia T Q, Sun H Y, Li C B, X Li, Feng D H, Qiu J R and Xu Z Z 2006 Mechanisms of femtosecond laser-induced breakdown and damage in MgO *Opt. Commun.* **259** 274–80

[129] Giguere D, Olivie G, Vidal F, Toetsch S, Girard G, Ozaki T, Kieffer J-C, Nada O and Brunette I 2007 Laser ablation threshold dependence on pulse duration for fused silica and corneal tissues: experiments and modeling *J. Opt. Soc. Am.* A **24** 1562–8

[130] Xu S, Qiu J, Jia T, Li C, Sun H and Xu Z 2007 Femtosecond laser ablation of crystals SiO_2 and YAG *Opt. Commun.* **274** 163–6

[131] Sanner N, Uteza O, Chimier B, Sentis M, Lassonde P, Legare F and Kieffer J C 2010 Toward determinism in surface damaging of dielectrics using few-cycle laser pulses *Appl. Phys. Lett.* **96** 071111

[132] Uteza O, Sanner N, Chimier B, Brocas A, Varkentina N, Sentis M, Lassonde P, Legare F and Kieffer J C 2011 Control of material removal of fused silica with single pulses of few optical cycles to sub-picosecond duration *Appl. Phys.* A **105** 131–41

[133] Englert L, Rethfeld B, Haag L, Wollenhaupt M, Sarpe-Tudoran C and Baumert T 2007 Control of ionization processes in high band gap materials via tailored femtosecond pulses *Opt. Express* **15** 17855–62

[134] Englert L, Wollenhaupt M, Haag L, Sarpe-Tudoran C, Rethfeld B and Baumert T 2008 Material processing of dielectrics with temporally asymmetric shaped femtosecond laser pulses on the nanometer scale *Appl. Phys.* A **92** 749–53

[135] Carr C W, Radousky H B and Demos S G 2003 Wavelength dependence of laser-induced damage: determining the damage initiation mechanisms *Phys. Rev. Lett.* **91** 127402

[136] Zavestovskaya I N, Eliseev P G, Krokhin O N and Men'kova N A 2008 Analysis of the nonlinear absorption mechanisms in ablation of transparent materials by high-intensity and ultrashort laser pulses *Appl. Phys.* A **92** 903–6

[137] Ziener C, Foster P S, Divall E J, Hooker C J, Hutchinson M H R, Langley A J and Neely D 2003 Specular reflectivity of plasma mirrors as a function of intensity, pulse duration, and angle of incidence *J. Appl. Phys.* **93** 768–70

[138] Doumy G, Quere F, Gobert O, Perdrix M, Martin P, Audebert P, Gauthier J C, Geindre J P and Wittmann T 2004 Complete characterization of a plasma mirror for the production of high-contrast ultraintense laser pulses *Phys. Rev.* E **69** 026402

[139] Chowdhury I H, Wu A Q, Xu X and Weiner A M 2005 Ultra-fast laser absorption and ablation dynamics in wide-band-gap dielectrics *Appl. Phys.* A **81** 1627–32

[140] Ashkenasi D, Lorenz M, Stoian R and Rosenfeld A 1999 Surface damage threshold and structuring of dielectrics using femtosecond laser pulses: the role of incubation *Appl. Surf. Sci.* **150** 101–6

[141] Lenzner M, Kruger J, Kautek W and Krausz F 1999 Incubation of laser ablation in fused silica with 5-fs pulses *Appl. Phys.* A **69** 465–6

[142] Rosenfeld A, Lorenz M, Stoian R and Ashkenasi D 1999 Ultrashort-laser-pulse damage threshold of transparent materials and the role of incubation *Appl. Phys.* A **69** *Laser Ablation. 5th Int. Conf. COLA'99, (Gottingen, Germany, July 19–23 1999)* (Berlin: Springer) pp 373–6

[143] Hertwig A, Martin S, Kruger J and Kautek W 2004 Surface damage and color centers generated by femtosecond pulses in borosilicate glass and silica *Appl. Phys.* A **79** 1075–7

[144] Bonse J, Wrobel J M, Kruger J and Kautek W 2001 Ultrashort-pulse laser ablation of indium phosphide in air *Appl. Phys.* A **72** 89–94

[145] Jee Y, Becker M F and Walser R M 1988 Laser-Induced Damage on Single-Crystal Metal-Surfaces *J. Opt. Soc. Am.* B **5** 648–59

[146] Martin S, Hertwig A, Lenzner M, Kruger J and Kautek W 2003 Spot-size dependence of the ablation threshold in dielectrics for femtosecond laser pulses *Appl. Phys.* A **77** 883–4

[147] Emmert L A, Mero M and Rudolph W 2010 Modeling the effect of native and laser-induced states on the dielectric breakdown of wide band gap optical materials by multiple subpicosecond laser pulses *J. Appl. Phys.* **108** 043523

[148] Nguyen D N, Emmert L A, Patel D, Menoni C S and Rudolph W 2010 Transient phenomena in the dielectric breakdown of HfO2 optical films probed by ultrafast laser pulse pairs *Appl. Phys. Lett.* **97** 191909

[149] Bonse J, Kruumlger J, Houmlhm S and Rosenfeld A 2012 Femtosecond laser-induced periodic surface structures *J. Laser Appl.* **24** 042006

[150] Eason R 2007 *Pulsed Laser Deposition of Thin Films* (Hoboken, NJ: Wiley)

[151] Chrisey D B and Hubler G K 1994 *Pulsed Laser Deposition of Thin Films* (New York: Wiley)

[152] Eliezer S *et al* 2004 Synthesis of nanoparticles with femtosecond laser pulses *Phys. Rev.* B **69** 144119

[153] Perez D and Lewis L J 2003 Molecular-dynamics study of ablation of solids under femtosecond laser pulses *Phys. Rev.* B **67** 184102

[154] Vitello M, Amoruso S and Wang X 2005 Femtosecond laser ablation and deposition *Pulsed Laser Deposition of Optoelectronic Films (Optoelectronic Materials and Devices)* vol 2, ed M Popescu (Bucharest, Romania: INOE) pp 41–80

[155] Perrière J, Boulmer-Leborgne C, Benzerga R and Tricot S 2007 Nanoparticle formation by femtosecond laser ablation *J. Phys. D: Appl. Phys.* **40** 7069–76

[156] Lorazo P, Lewis L J and Meunier M 2003 Short-pulse laser ablation of solids: from phase explosion to fragmentation *Phys. Rev. Lett.* **91** 225502

[157] Zhigilei L V and Garrison B J 2000 Microscopic mechanisms of laser ablation of organic solids in the thermal and stress confinement irradiation regimes *J. Appl. Phys.* **88** 1281–98

[158] Zhigilei L V 2003 Dynamics of the plume formation and parameters of the ejected clusters in short-pulse laser ablation *Appl. Phys.* A **76** 339–50

[159] Cheng C R and Xu X F 2005 Mechanisms of decomposition of metal during femtosecond laser ablation *Phys. Rev.* B **72** 165415

[160] Amoruso S, Bruzzese R, Wang X, Nedialkov N N and Atanasov P A 2007 Femtosecond laser ablation of nickel in vacuum *J. Phys. D: Appl. Phys.* **40** 331–40

[161] Upadhyay A K, Inogamov N A, Rethfeld B and Urbassek H M 2008 Ablation by ultrashort laser pulses: atomistic and thermodynamic analysis of the processes at the ablation threshold *Phys. Rev.* B **78** 045437

[162] Zhigilei L V, Lin Z and Ivanov D S 2009 atomistic modeling of short pulse laser ablation of metals: connections between melting, spallation, and phase explosion *J. Phys. Chem.* C **113** 11892–906

[163] Zhigilei L V, Lin Z, Ivanov D S, Leveugle E, Duff W H, Thomas D, Sevilla C and Guy S T 2010 Atomic/molecular-level simulations of laser-material interactions *Laser-Surface Interactions for New Materials Production: Tailoring Structure and Properties* (*Springer Series in Materials Science* vol 130) ed A Miotello and P M Ossi (New York: Springer) pp 43–79

[164] Perez D and Lewis L J 2002 Ablation of solids under femtosecond laser pulses *Phys. Rev. Lett.* **89** 255504

[165] Blink J A and Hoover W G 1985 Fragmentation of suddenly heated liquids *Phys. Rev.* A **32** 1027–35

[166] Barker J A, Henderson D and Abraham F F 1981 Phase-diagram of the two-dimensional lennard-jones system—evidence for 1st-order transitions *Physica* A **106** 226–38

[167] Holian B L and Grady D E 1988 Fragmentation by molecular-dynamics—the microscopic big-bang *Phys. Rev. Lett.* **60** 1355–8

[168] Vidal F, Johnston T W, Laville S, Barthelemy O, Chaker M, Le Drogoff B, Margot J and Sabsabi M 2001 Critical-point phase separation in laser ablation of conductors *Phys. Rev. Lett.* **86** 2573–6

[169] Povarnitsyn M E, Itina T E, Sentis M, Khishchenko K V and Levashov P R 2007 Material decomposition mechanisms in femtosecond laser interactions with metals *Phys. Rev.* B **75** 235414

[170] Lorazo P, Lewis L J and Meunier M 2006 Thermodynamic pathways to melting, ablation, and solidification in absorbing solids under pulsed laser irradiation *Phys. Rev.* B **73** 134108

[171] Zel'dovich Ya B and Raizer Yu P 2002 *Physics of Shock Waves and High-Temperature Hydrodynamic Phenomena* (New York: Dover)

[172] Hansen T N, Schou J and Lunney J G 1999 Langmuir probe study of plasma expansion in pulsed laser ablation *5th Int. Conf. on Laser Ablation COLA'99 (Gottingen, Germany, 19–23 July, 1999) Appl. Phys.* A **69** S601–4

[173] Toftmann B, Schou J and Lunney J G 2003 Dynamics of the plume produced by nanosecond ultraviolet laser ablation of metals *Phys. Rev.* B **67** 104101

[174] Cherednikov Y, Inogamov N A and Urbassek H M 2011 Atomistic modeling of ultrashort-pulse ultraviolet laser ablation of a thin LiF film *J. Opt. Soc. Am.* B **28** 1817–24

[175] Amoruso S, Bruzzese R, Spinelli N, Velotta R, Vitiello M and Wang X 2004 Emission of nanoparticles during ultrashort laser irradiation of silicon targets *Europhys. Lett.* **67** 404–10

[176] Amoruso S, Ausanio G, Bruzzese R, Vitiello M and Wang X 2005 Femtosecond laser pulse irradiation of solid targets as a general route to nanoparticle formation in a vacuum *Phys. Rev.* B **71** 033406

[177] Grojo D, Hermann J and Perrone A 2005 Plasma analyses during femtosecond laser ablation of Ti, Zr, and Hf *J. Appl. Phys.* **97** 063306

[178] Teghil R, D'Alessio L, Santagata A, Zaccagnino M, Ferro D and Sordelet D J 2003 Picosecond and femtosecond pulsed laser ablation and deposition of quasicrystals *Appl. Surf. Sci.* **210** 307–17

[179] Albert O, Roger S, Glinec Y, Loulergue J C, Etchepare J, Boulmer-Leborgne C, Perrière J and Millon E 2003 Time-resolved spectroscopy measurements of a titanium plasma induced by nanosecond and femtosecond lasers *Appl. Phys.* A **76** 319–23

[180] De Bonis A, Teghil R, Rau J V, Galasso A, Orlando S and Santagata A 2011 Characterization of gaseous phase and nanoparticles produced in ultra-short pulsed laser ablation of transition metal borides *Appl. Surf. Sci.* **257** 5315–18

[181] Amoruso S, Bruzzese R, Spinelli N, Velotta R, Vitiello M, Wang X, Ausanio G, Iannotti V and Lanotte L 2004 Generation of silicon nanoparticles via femtosecond laser ablation in vacuum *Appl. Phys. Lett.* **84** 4502–4

[182] Sanz M, Castillejo M, Amoruso S, Ausanio G, Bruzzese R and Wang X 2010 Ultra-fast laser ablation and deposition of TiO_2 *Appl. Phys.* A **101** 639–44

[183] Sanz M, Lopez-Arias M, Marco J F, de Nalda R, Amoruso S, Ausanio G, Lettieri S, Bruzzese R, Wang X, and Castillejo M 2011 Ultrafast laser ablation and deposition of wide band gap semiconductors *J. Phys. Chem.* C **115** 3203–11

[184] Amoruso S, Bruzzese R, Wang X and Xia J 2008 Propagation of a femtosecond pulsed laser ablation plume into a background atmosphere *Appl. Phys. Lett.* **92** 041503

[185] Noel S and Hermann J 2009 Reducing nanoparticles in metal ablation plumes produced by two delayed short laser pulses *Appl. Phys. Lett.* **94** 053120

[186] Glover T E *et al* 2003 Metal–insulator transitions in an expanding metallic fluid: particle formation kinetics *Phys. Rev. Lett.* **90** 236102

[187] Anisimov S I, Bauerle D and Lukyanchuk B S 1993 Gas-dynamics and film profiles in pulsed-laser deposition of materials *Phys. Rev.* B **48** 12076–81

[188] Anisimov S I, Lukyanchuk B S and Luches A 1996 An analytical model for three-dimensional laser plume expansion into vacuum in hydrodynamic regime *3rd Int. Conf. on Laser Ablation (COLA 95) (Strasbourg, France, 22–26 May, 1995) Appl. Surf. Sci.* **96–8** 24–32

[189] Dreyfus R W 1991 CU^0, CU^+, and Cu_2 from excimer-ablated copper *J. Appl. Phys.* **69** 1721–9

[190] Willmott P R and Huber J R 2000 Pulsed laser vaporization and deposition *Rev. Mod. Phys.* **72** 315–28

[191] Amoruso S, Wang X, Altucci C, de Lisio C, Armenante M, Bruzzese R, Spinelli N and Velotta R 2002 Double-peak distribution of electron and ion emission profile during femtosecond laser ablation of metals *Spring Meeting of the European-Materials-Research-Society (Strasbourg, France, 5–8 June, 2001) Appl. Surf. Sci.* **186** 358–63

[192] Claeyssens F, Henley S J and Ashfold M N R 2003 Comparison of the ablation plumes arising from ArF laser ablation of graphite, silicon, copper, and aluminum in vacuum *J. Appl. Phys.* **94** 2203–11

[193] Zhang Z, VanRompay P A, Nees J A and Pronko P P 2002 Multi-diagnostic comparison of femtosecond and nanosecond pulsed laser plasmas *J. Appl. Phys.* **92** 2867–74

[194] Canulescu S, Papadopoulou E, Anglos D, Lippert T, Montenegro M J, Georgiou S, Doebeli M and Wokaun A 2011 Nanosecond and femtosecond ablation of $La_{0.6}Ca_{0.4}CoO_3$: a comparison between plume dynamics and composition of the films *Appl. Phys.* A **105** 167–76

[195] Thestrup B, Toftmann B, Schou J, Doggett B and Lunney J G 2002 Ion dynamics in laser ablation plumes from selected metals at 355 nm *6th Int. Conf. on Laser Ablation (Tsukuba, Japan, 1–5 October, 2001) Appl. Surf. Sci.* **197–198** 175–80

[196] Baraldi G, Perea A and Afonso C N 2011 Dynamics of ions produced by laser ablation of several metals at 193 nm *J. Appl. Phys.* **109** 043302

[197] Perrière J, Millon E, Seiler W, Boulmer-Leborgne C, Craciun V, Albert O, Loulergue J C and Etchepare J 2002 Comparison between ZnO films grown by femtosecond and nanosecond laser ablation *J. Appl. Phys.* **91** 690–6

[198] Schou J 2009 Physical aspects of the pulsed laser deposition technique: the stoichiometric transfer of material from target to film *Appl. Surf. Sci.* **255** 5191–8

[199] Amoruso S, Toftmann B and Schou J 2004 Thermalization of a UV laser ablation plume in a background gas: from a directed to a diffusionlike flow *Phys. Rev.* E **69** 056403

[200] Predtechensky M R and Mayorov A P 1992 Expansion of laser-plasma in oxygen at laser deposition of HTSC films—theoretical-model *World Congress on Superconductivity (Munich, Germany, 15–18 September, 1992) Appl. Supercond.* **1** 2011–17

[201] Amoruso S, Schou J and Lunney J G 2008 Influence of the atomic mass of the background gas on laser ablation plume propagation *Appl. Phys.* A **92** 907–11

[202] Bulgakova N M, Stoian R, Rosenfeld A, Hertel I V and Campbell E E B 2004 Electronic transport and consequences for material removal in ultrafast pulsed laser ablation of materials *Phys. Rev.* B **69** 054102

[203] Sattler K, Muhlbach J, Echt O, Pfau P and Recknagel E 1981 Evidence for coulomb explosion of doubly charged microclusters *Phys. Rev. Lett.* **47** 160–3

[204] Stoian R, Rosenfeld A, Hertel I V, Bulgakova N M and Campbell E E B 2004 Comment on 'Coulomb explosion in femtosecond laser ablation of Si(1 1 1)' *Appl. Phys. Lett.* **85** 694–5

[205] Bulgakova N M, Stoian R, Rosenfeld A, Hertel I V, Marine W and Campbell E E B 2005 A general continuum approach to describe fast electronic transport in pulsed laser irradiated materials: the problem of Coulomb explosion *Appl. Phys.* A **81** 345–56

[206] Reif J, Costache F, Eckert S and Henyk M 2004 Mechanisms of ultra-short laser pulse ablation from ionic crystals *Appl. Phys.* A **453–454** 1229–31

[207] Costache F and Reif J 2004 Femtosecond laser induced Coulomb explosion from calcium fluoride *EMRS 2003 Spring Conf. (Strasbourg, France, 10–11 June, 2003) Thin Solid Films* **453** 334–9

[208] Henyk M, Costache F and Reif J 2002 Femtosecond laser ablation from sodium chloride and barium fluoride *Spring Meeting of the European-Materials-Research-Society (Strasbourg, France, 5–8 June, 2001) Appl. Surf. Sci.* **186** 381–4

[209] Roeterdink W G, Juurlink L B F, Vaughan O P H, Diez J D, Bonn M and Kleyn A W 2003 Coulomb explosion in femtosecond laser ablation of Si(1 1 1) *Appl. Phys. Lett.* **82** 4190–2

[210] Dachraoui H, Husinsky W and Betz G 2006 Ultra-short laser ablation of metals and semiconductors: evidence of ultra-fast Coulomb explosion *Appl. Phys.* A **83** 333–6

[211] Bashir S, Shahid Rafique M and Husinsky W 2012 Identification of ultra-fast electronic and thermal processes

during femtosecond laser ablation of Si *Appl. Phys.* A **109** 421–9

[212] Szymonski M 1993 Electronic sputtering of alkali halides *Fundamental Processes in Sputtering of Atoms and Molecules (SPUT92)* Kongelige Danske Videnskabernes Selskab: Matematisk-Fysiske Meddelelser ed P Sigmund *Symp. on the Occasion of the 250th Anniversary of the Royal-Danish-Academy-of-Sciences-and-Letters - Fundamental Processes in Sputtering of Atoms and Molecules (SPUT92) (Copenhagen, Denmark, 30 August–4 September 1992)* pp 495–526

[213] Johnson R E and Schou J 1993 Sputtering of inorganic insulators *Fundamental Processes in Sputtering of Atoms and Molecules (SPUT92)* Kongelige Danske Videnskabernes Selskab: Matematisk-Fysiske Meddelelser ed P Sigmund *Symp. on the Occasion of the 250th Anniversary of the Royal-Danish-Academy-of-Sciences-and-Letters - Fundamental Processes in Sputtering of Atoms and Molecules (SPUT92) (Copenhagen, Denmark, 30 August–4 September, 1992)* pp 403–93

[214] Kimmel G A, Orlando T M, Cloutier P and Sanche L 1997 Low-energy (5–40 eV) electron-stimulated desorption of atomic hydrogen and metastable emission from amorphous ice *Symp. on Physics and Chemistry of Ice 1996 (Hanover, NH, 27–31 August, 1996) J. Phys. Chem.* B **101** 6301–3

[215] Lowndes D H 1998 Growth and doping of compound semiconductor films by pulsed laser ablation *Laser Ablation and Desorption* (*Experimental Methods in the Physical Sciences* vol 30) ed J C Miller and R F Haglund (San Diego, CA: Academic) pp 475–571

[216] Millon E, Perriere J, Defourneau R M, Defourneau D, Albert O and Etchepare J 2003 Femtosecond pulsed-laser deposition of BaTiO$_3$ *Appl. Phys.* A **77** 73–80

[217] Toftmann B, Doggett B, Budtz-Jørgensen C, Schou J and Lunney J G 2013 Comparison of plume dynamics in UV femtosecond and nanosecond laser ablation of silver *J. Appl. Phys.* submitted

[218] Teghil R, D'Alessio L, De Bonis A, Galasso A, Ibris N, Maria Salvi A, Santagata A and Villani P 2009 Nanoparticles and thin film formation in ultrashort pulsed laser deposition of vanadium oxide *J. Phys. Chem.* A **113** 14969–74

[219] Donnelly T, Lunney J G, Amoruso S, Bruzzese R, Wang X and Ni X 2010 Dynamics of the plumes produced by ultrafast laser ablation of metals *J. Appl. Phys.* **108** 043309

[220] Donnelly T, Lunney J G, Amoruso S, Bruzzese R, Wang X and Ni X 2010 Angular distributions of plume components in ultrafast laser ablation of metal targets *Appl. Phys.* A **100** 569–74

[221] Schou J, Amoruso S and Lunney J G 2007 Plume dynamics *Laser Ablation and its Applications* ed C R Phipps (New York: Springer) pp 67–95

[222] Claeyssens F, Ashfold M N R, Sofoulakis E, Ristoscu C G, Anglos D and Fotakis C 2002 Plume emissions accompanying 248 nm laser ablation of graphite in vacuum: effects of pulse duration *J. Appl. Phys.* **91** 6162–72

[223] Stock M and Molian P 2004 Femtosecond pulsed laser deposition of amorphous, ultrahard boride thin films *11th Canadian Semiconductor Technology Conf. (CSTC) (Ottawa, Canada, 18–22 August, 2003) J. Vac. Sci. Technol.* A **22** 670–5

[224] Ristoscu C, Ghica C, Papadopoulou E L, Socol G, Gray D, Mironov B, Mihailescu I N and Fotakis C 2011 Modification of AlN thin films morphology and structure by temporally shaping of fs laser pulses used for deposition *Thin Solid Films* **519** 6381–7

[225] Gyorgy E, Ristoscu C, Mihailescu I N, Klini A, Vainos N, Fotakis C, Ghica C, Schmerber G and Faerber J 2001 Role of laser pulse duration and gas pressure in deposition of AlN thin films *J. Appl. Phys.* **90** 456–61

[226] Zhang Z, VanRompay P A, Nees J A, Clarke R, Pan X and Pronko P P 2000 Nitride film deposition by femtosecond and nanosecond laser ablation in low-pressure nitrogen discharge gas *Symp. A on Photo-Excited Processes, Diagnostics and Applications of the 1999 E-MRS Spring Conference (Strasbourg, France, 1–4 June, 1999) Appl. Surf. Sci.* **154** 165–71

[227] Watanabe K, Taniguchi T and Kanda H 2004 Direct-bandgap properties and evidence for ultraviolet lasing of hexagonal boron nitride single crystal *Nature Mater.* **3** 404–9

[228] Sanz M, de Nalda R, Marco J F, Izquierdo J G, Banares L and Castillejo M 2010 Femtosecond pulsed laser deposition of nanostructured CdS films *J. Phys. Chem.* C **114** 4864–8

[229] Tong X L, Jiang D S, Liu Z M, Luo M Z, Li Y, Lu P X, Yang G and Long H 2008 Structural characterization of CdS thin film on quartz formed by femtosecond pulsed laser deposition at high temperature *Thin Solid Films* **516** 2003–8

[230] Tong X L, Jiang D S, Yan Q Y, Hu W B, Liu Z M and Luo M Z 2008 Deposition of CdS thin films onto Si(1 1 1) substrate by PLD with femtosecond pulse *5th Iberian Vacuum Meeting (Univ Minho, Guimaraes, Portugal, 18–21 September, 2005) Vacuum* **82** 1411–14

[231] Teghil R, Santagata A, De Bonis A, Galasso A and Villani P 2009 Chromium carbide thin films deposited by ultra-short pulse laser deposition *Appl. Surf. Sci.* **255** 7729–33

[232] Dinh L N, Hayes S E, Wynne A E, Wall M A, Saw C K, Stuart B C, Balooch M, Paravastu A K and Reimer J A 2002 Properties of GaAs nanoclusters deposited by a femtosecond laser *J. Mater. Sci.* **37** 3953–8

[233] Trelenberg T W, Dinh L N, Saw C K, Stuart B C and Balooch M 2004 Femtosecond pulsed laser ablation of GaAs *Appl. Surf. Sci.* **221** 364–9

[234] Tong X L, Jiang D S, Liu L and Dai H 2008 Comparison between GaN thin film grown by femtosecond and nanosecond pulsed laser depositions *J. Vac. Sci. Technol.* B **26** 1398–403

[235] Pronko P P, Zhang Z and VanRompay P A 2003 Critical density effects in femtosecond ablation plasmas and consequences for high intensity pulsed laser deposition *Conference on Physics and Chemistry of Advanced Laser Materials Processing (Strasbourg, France, 18–21 June, 2002) Appl. Surf. Sci.* **208–209** 492–501

[236] Teghil R, D'Alessio L, De Bonis A, Galasso A, Villani P, Zaccagnino M, Santagata A and Ferro D 2005 Ferntosecond pulsed laser ablation of group 4 carbides *Spring Meeting of the European-Materials-Research-Society (Strasbourg, France, 24–28 May, 2004) Appl. Surf. Sci.* **247** 51–6

[237] Taurian O E, Springborg M and Christensen N E 1985 Self-consistent electronic-structures of MgO and SrO *Solid State Commun.* **55** 351–5

[238] Darby M S B, May-Smith T C, Eason R W, Donnelly T, Lunney J G and Rogers K D 2008 A comparative study of gadolinium gallium garnet growth by femtosecond and nanosecond pulsed laser deposition *Appl. Surf. Sci.* **254** 3364–9

[239] Ghica C, Ristoscu C, Socol G, Brodoceanu D, Nistor L C, Mihailescu I N, Klini A and Fotakis C 2006 Growth and characterization of β-SiC films obtained by fs laser ablation *Symp. on Advances in Laser and Lamp Processing of Functional Materials (Strasbourg, France, 31 May–3 June, 2005) Appl. Surf. Sci.* **252** 4672–7

[240] Kim S, Spanier J E and Herman I P 2000 Optical transmission, photoluminescence, and Raman scattering of

porous SiC prepared from p-type 6H SiC *Japan. J. Appl. Phys. Part 1* **39** 5875–8

[241] Dominguez J E, Pan X Q, Fu L, Van Rompay P A, Zhang Z, Nees J A and Pronko P P 2002 Epitaxial SnO$_2$ thin films grown on ($\bar{1}$ 0 1 2) sapphire by femtosecond pulsed laser deposition *J. Appl. Phys.* **91** 1060–5

[242] Cox D F, Fryberger T B and Semancik S 1988 Oxygen vacancies and defect electronic states on the SnO$_2$(1 1 0)-1X1 Surface *Phys. Rev.* B **38** 2072–83

[243] Teghil R, De Bonis A, Galasso A, Villani P and Santagata A 2007 Ferntosecond pulsed laser ablation deposition of tantalum carbide *Symp. Laser Synthesis and Processing of Advanced Materials held at the E-MRS 2007 Spring Meeting (Strasbourg, France, 2007) Appl. Surf. Sci.* **254** 1220–3

[244] Teghil R, D'Alessio L, De Bonis A, Galasso A, Villani P and Santagata A 2006 Femtosecond pulsed laser ablation and deposition of titanium carbide *Thin Solid Films* **515** 1411–18

[245] Gamez F *et al* 2010 Nanoparticle TiO$_2$ films prepared by pulsed laser deposition: laser desorption and cationization of model adsorbates *J. Phys. Chem. C* **114** 17409–15

[246] Sanz M, Walczak M, de Nalda R, Oujja M, Marco J F, Rodriguez J, Izquierdo J G, Banares L and Castillejo M 2009 Femtosecond pulsed laser deposition of nanostructured TiO$_2$ films *Appl. Surf. Sci.* **255** 5206–10

[247] Teghil R, De Bonis A, Galasso A, Villani P and Santagata A, Ferro D and Barinov S M 2009 Nanostructured thin films obtained by ultra-short pulse laser deposition of vanadium carbide *Appl. Surf. Sci.* **255** 5220–3

[248] Krishnakumar S and Menon C S 1996 Optical and electrical properties of vanadium pentoxide thin films *Phys. Status Solidi* A **153** 439–44

[249] Rau J V, Latini A, Teghil R, De Bonis A, Fosca M, Caminiti R and Albertini V R 2011 Superhard tungsten tetraboride films prepared by pulsed laser deposition method *ACS Appl. Mater. Interfaces* **3** 3738–43

[250] De Bonis A, Teghil R, Santagata A, Galasso A and Rau J V 2012 Thin films deposited by femtosecond pulsed laser ablation of tungsten carbide *Appl. Surf. Sci.* **258** 9198–201

[251] Chau J L H, Yang M-C, Nakamura T, Sato S, Yang C-C and Cheng C-W 2010 Fabrication of ZnO thin films by femtosecond pulsed laser deposition *Opt. Laser Technol.* **42** 1337–9

[252] Yang Y, Long H, Yang G, Chen A, Zheng Q and Lu P 2009 Femtosecond laser deposited zinc oxide film and its optical properties *Vacuum* **83** 892–6

[253] Liu B, Hu Z, Che Y, Allenic A, Sun K and Pan X 2008 Growth of ZnO nanoparticles and nanorods with ultrafast pulsed laser deposition *Appl. Phys. A* **93** 813–18

[254] Yang Y, Long H, Yang G, Dai N, Zheng Q and Lu P 2008 Structural properties of ZnO thin films on Si substrate using femtosecond laser deposition *J. Cryst. Growth* **310** 551–5

[255] Klini A, Manousaki A, Anglos D and Fotakis C 2005 Growth of ZnO thin films by ultraviolet pulsed-laser ablation: study of plume dynamics *J. Appl. Phys.* **98** 123301

[256] Okoshi M, Higashikawa K and Hanabusa M 2001 Wavelength dependence of femtosecond pulsed laser deposition of zinc oxide films *Japan. J. Appl. Phys. Part 1* **40** 1287–8

[257] Rode A V, Gamaly E G and Luther-Davies 2007 Ultrafast laser ablation and film deposition *Pulsed Laser Deposition of Thin Films* ed R Eason (Hoboken, NJ: Wiley) pp 99–129

[258] Acharya K P, Mahalingm K and Ullrich B 2010 Structural, compositional, and optoelectronic properties of thin-film CdS on p-GaAs prepared by pulsed-laser deposition *17th Int. Mater. Research Congress (Cancun, Mexico, 17–21 August, 2008) Thin Solid Films* **518** 1784–7

[259] Mclaughlin M, Sakeek H F, Maguire P, Graham W G, Molloy J, Morrow T, Laverty S and Anderson J 1993 Properties of ZnS thin-films prepared by 248 nm pulsed-laser deposition *Appl. Phys. Lett.* **63** 1865–7

[260] Svendsen W, Ellegaard O and Schou J 1996 Laser ablation deposition measurements from silver and nickel *Appl. Phys.* A **63** 247–55

[261] Noel S, Hermann J and Itina T 2007 Investigation of nanoparticle generation during femtosecond laser ablation of metals *5th Int. Conf. on Photo-Excited Processes and Applications (Charlotteville, VA, September 2006) Appl. Surf. Sci.* **253** 6310–15